Development and Application of Multifunctional Optical Coherence Tomography

Zhongwei Zhi

A dissertation

submitted in partial fulfillment of the

requirements for the degree of

Doctor of Philosophy

University of Washington

2014

Reading Committee:
Ruikang Wang, Chair
Qiuming Yu
Chun Yuan

Program Authorized to Offer Degree:

Bioengineering

University of Washington

Abstract

Development and Application of Multifunctional Optical Coherence Tomography

Zhongwei Zhi

Chair of Supervisory Committee:

Professor Ruikang Wang

Department of Bioengineering and Ophthalmology

Microcirculation refers to the functions of capillaries and the neighboring lymphatic vessels. It plays a vital role in the pathophysiology of disorders in many clinical areas including cardiology, dermatology, neurology and ophthalmology, and so forth. It is crucial to develop imaging technologies that can provide both qualitative and quantitative information as to how microcirculation responds to certain injury and/or disease, and its treatment. Optical coherence tomography (OCT) is a non-invasive optical imaging technique for high-resolution cross-sectional imaging of specimens, with many applications in clinical medicine. Current state-of-the-art OCT systems operate in the Fourier domain, using either a broadband light source with a spectrometer, known as spectral domain OCT (SDOCT), or a rapidly tunable laser, known as swept source OCT (SSOCT). The current Fourier domain OCT systems have dramatically improvement in sensitivity, resolution and speed compared to time domain OCT. In addition to the improvement in the OCT system hardware, different methods for functional measurements of tissue beds have been developed and demonstrated. This includes but not limited to, i) Phase-resolved Doppler OCT for quantifying the blood flow, ii) OCT angiography for visualization of microvasculature, iii) Polarization sensitive OCT for measuring the intrinsic optical property/ birefringence of tissue, iv) spectroscopic OCT for measuring blood oxygenation, etc. Functional

OCT can provide important clinical information that is not available in the typical intensity based structural OCT images. Among these functional OCT modalities, Doppler OCT and OCT angiography attract great interests as they show high capability for *in vivo* study of microvascular pathology.

By analyzing the Doppler effect of a flowing particle on light frequency, Doppler OCT allows the quantification of the blood flow speed and blood flow rate. The most popular approach for Doppler OCT is achieved through analysis of the phase term in complex OCT signal which termed as Phase-resolved Doppler OCT. However, as limited by the phase noise and motion, Phase-resolved Doppler OCT can only be applied for relative large blood vessels, such as arterioles and venules. On the other hand, in order to visualize the microcirculation network, a number of strategies to enable better contrast of microvasculature components, which we termed OCT angiography, have been introduced during recent years. As a variation of Fourier domain OCT, optical microangiography (OMAG) is one of the earliest proposed OCT angiography techniques which is capable of generating 3D images of dynamic blood perfusion distribution within microcirculatory tissue beds. The OMAG algorithm works by separating the static and moving elements by high pass filtering on complex valued interferometric data using Hilbert transform. Based on the conventional OMAG algorithm, we further developed ultra-high sensitive OMAG (UHS-OMAG) by switching the high-pass filtering from fast scan direction (adjacent A-lines within one B-frame) to slow scan direction (adjacent B-frames), which has a dramatically improved performance for capillary network imaging and analysis.

Apart from the microvascular study with current available functional OCT for, visualization of the lymphatic system (lymph nodes and lymphatic vessels) plays a significant role in assessing patients with various malignancies and lymphedema. However, there is a lack of label-free and noninvasive method for lymphangiography. Hence, a cutting edge research to investigate the capability of OCT as a tool for non-invasive and label-free lymphangiography would be highly desired.

The objective of my thesis is to develop a multiple-functional SDOCT system to image the microcirculation and quantify the several important parameters of microcirculation within microcirculatory tissue beds, and further apply it for pre-clinical research applications. The multifunctional OCT system provides modalities including structural OCT, OCT angiography, Doppler OCT and Optical lymphangiography, for multi-parametric study of tissue microstructure, blood vessel morphology, blood flow and lymphatic vessel all together. The thesis mainly focuses on two parts: first, development of multi-functional OCT/ OMAG system and methods for volumetric imaging of microvasculature and quantitative measurement of blood flow, and its application for pathological research in ophthalmology on rodent eye models which aims to uncover the mechanism, provides early diagnosis and treatment evaluation of ocular diseases, such as glaucoma and diabetic retinopathy. Second, development of ultra-high resolution OCT system and algorithm for simultaneous label-free imaging of blood and lymphatic vessel, and its application in wound healing study on mouse ear flap model.

Objectives of my research are achieved through the following specific aims:

Aim 1: Theoretical analysis and algorithm development to improve the sensitivity of OMAG for microvasculature imaging; perform volumetric and quantitative imaging of vasculature with combined OMAG and Phase-resolved Doppler OCT for i*n vivo* study of vascular physiology.

Aim 2: Develop high speed high resolution OCT system and method for rodent eye imaging. Apply the combined OMAG and Phase-resolved Doppler OCT approach to investigate the impact of elevated intraocular pressure on retinal, choroidal and optic nerve head blood flow in rat eye model, which aids to the better understanding of the mechanism and development of glaucoma.

Aim 3: Apply the developed OCT system and ultra-high sensitive OMAG algorithm for noninvasive imaging of retinal morphology and microvasculature in obese mice, which may play an important role in early diagnosis of Diabetic retinopathy.

Aim 4: Developing an ultra-high resolution SDOCT system using broadband Supercontinuum light source to achieve ultra-high resolution microvasculature imaging of biological tissue.

Aim 5: Develop methods for simultaneous label free optical imaging of blood and lymphatic vessel and demonstrate its capability by monitoring the blood and lymph response to wound healing on mouse ear pinna model.

Acknowledgements

I wish to thank all those who participated in this work and provided help and support to me during my PhD studies.

I would like to express my deepest gratitude to my advisor, Dr. Ruikang Wang, for his excellent guidance, caring, and providing me with an excellent atmosphere for my research. Dr. Wang is a great advisor that helps me to be productive and innovative. I would also like to thank my committee members, Dr. Chuan Yuan, Dr. Paul Wiggins and Dr. Qiuming Yu for guiding my research and helping me to develop my knowledge of medical device and medical imaging.

I would like to show my special thanks to our collaborator Dr. John Morrison and William Cepurna from Casey eye institute, OHSU. Dr. Morrison's brilliant knowledge and great enthusiasm for Glaucoma research helps a lot to my work. I would also like to thank Dr. Charlie Alpers from department of pathology at University of Washington for his collaboration. Thanks to the Diabetes research center at UW to award me the Samuel and Althea Stroum Endowed Diabetes Fellowship.

Many thanks to Yali Jia, Lin An, Yaguang Zeng, Zhenhe Ma, Yi Wang for helping me to learn Optical coherence tomography from the very beginning. Great thanks to my colleagues Siavash Yosefi, Roberto Reif, Xin Yin, Jia Qin, Lei Shi, Jenny Li, and Hequn Wang. My research would not have been possible without their helps. I would like to thank my good friends Zheng Li Xi Cheng and Gongpu Lan, who were always willing to help and encourage me.

I would like to thank my family, my parents Xinhong Zhi and Qinge Zhang, my parents in law Changan Zhao and Lijun Yin, and my siblings Zhongwen Zhi and Zhongying Zhi. They were always there supporting me and loving me with no reservations.

Finally, I must thank my dear wife, Yina Zhao. She was always there cheering me up and standing by me through the good and bad times. I wouldn't make this without her love and support. Our lovely son Rudy Zhi is the best gift for us.

To my beloved wife Yina Zhao and my son Rudy Zhi

Table of contents

List of Figures

Chapter 1. Introduction

1.1 Background: microcirculation within tissue beds

The term microcirculation [1] refers to the functions of capillaries and the neighboring lymphatic vessels. Microcirculation delivers fresh blood to the smallest blood vessels, present in the vasculature embedded within tissue beds. The microcirculation plays a vital role in the pathophysiology of disorders in many clinical areas including cardiology, dermatology, neurology and ophthalmology, and so forth.

As shown in Fig. 1.1, the microcirculation is composed by terminal arterioles, capillaries and venules. The vessels on the arterial side of the microcirculation are called the arterioles, which are well innervated. Arterioles carry the blood to the capillaries, which are not innervated, have no smooth muscle, and are about 5-8 μm in diameter. Blood flows out of the capillaries are drained into the venules, and further into the veins. In addition to these blood vessels, the microcirculation also includes lymphatic capillaries and collecting ducts, which has an important role in inflammation.

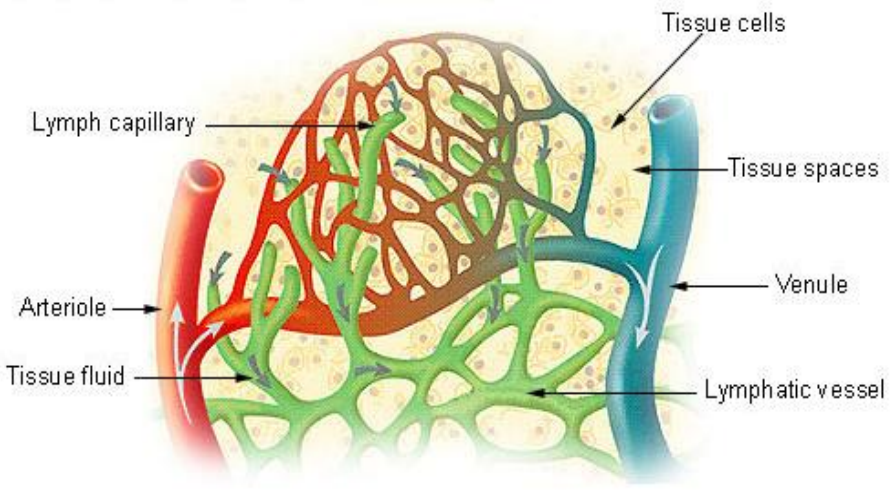

Fig. 1.1 Schematics of microcirculation, includes the proper function of blood and lymphatic vessels. The figure was adapted from Wikipedia.

The proper function of microcirculation is important because it regulates: i. Blood flow and tissue perfusion; ii. Delivery of oxygen and other nutrients and removal of CO_2 and other metabolic waste products; iii. Tissue fluid balance (abnormal lymphatic flow can cause swelling or edema), etc. In many different physiological and pathophysiological conditions it is crucial to image the microcirculation [2]. In clinical research, noninvasive imaging of microcirculation could be of great significance in accessing the effect of medical or surgical intervention in clinical trials, and in clinical practice it could be helpful to assist in diagnosis and monitoring of disease progression or the result of therapy in individual patients. Therefore, there is a special demand in the community, both biological and physical, to develop imaging technologies that can provide both qualitative and quantitative information as to how microcirculation responds to certain injury and/or disease, and its treatment.

Optical imaging methods [3] are now widely used in studies of both cellular and vascular physiology and pathology. Currently, *in vivo* optical imaging modalities can be broadly classified into two groups: macroscopic methods using diffuse light (optical intrinsic signal imaging [4], laser Doppler imaging [5], laser speckle imaging[6], and diffuse optical imaging[7], which achieve spatial resolutions of hundreds of microns to millimeters, and microscopic methods (two photon and confocal microscopy) which achieve micron-scale resolutions. Two-photon microscopy [8], in particular, is widely used in structural and functional imaging at the cellular and subcellular levels. While macroscopic imaging methods using diffuse light can achieve high penetration depths and large fields of view, they do not provide high spatial resolution. While two-photon microscopy achieves subcellular spatial resolution, the imaging speed, penetration depth, and field of view are limited.

Optical Coherence Tomography (OCT) [9] possesses a unique combination of high imaging speed, penetration depth, field of view, and resolution and therefore occupies an important niche between the macroscopic and microscopic optical imaging technologies discussed above. Hence,

it can be a great noninvasive imaging tool for the study of microcirculation and microcirculatory tissue beds.

1.2 Optical coherence tomography

Optical coherence tomography (OCT) is an imaging modality analogous to ultrasound, but measuring the intensity of back-reflected infrared light instead of sound. OCT is rapidly developing since it is a non-invasive, contrast-agent-free, cross-sectional and high-resolution imaging modality that can provide images of tissue morphology as well as functional information *in vivo* and in real time. Here, we will introduce the basic principle of OCT, current state of art Fourier domain OCT, essential parameters determines the system performance and the functional modalities of OCT.

1.2.1 Principle of OCT

OCT is an interferometric technique, relying on interference between a split and later re-combined broadband optical field. A typical time domain OCT schematic (based on a Michelson interferometer) is shown in Fig. 1.2. It consists of a light source, a beam splitter, a reference mirror, a sample arm and a detector.

Light emitted from the light source is divided by the beam splitter between the two arms of the interferometer. The split field travels in a reference path, reflecting from a reference mirror, and also in a sample path where it is reflected from multiple layers within a sample. Due to the broadband nature of the light, interference between the optical fields is only observed when the reference and sample arm optical path lengths are matched to within the coherence length of the light. Therefore, the depth (axial) resolution of an OCT system is determined by the temporal coherence of the light source. Sharp refractive index variations between layers in the sample medium manifest themselves as corresponding intensity peaks in the interference pattern. A time domain interference pattern can be obtained by translating the reference mirror to change the reference path length and match multiple optical paths due to layer reflections within the sample.

Thus, a one-dimensional image could be acquired along the depth with the intensity reflects the light reflection of different tissue layers. However, the speed of time domain OCT are limited due to the slow mechanical scanning along the depth. The A-line (one depth scan) scanning rate of an time domain OCT is ~ 2 kHz (maximum ~8 kHz). Notably, in OCT, a two- or three-dimensional image is obtained by making multiple depth scans. These scans are performed through laterally scanning the beam in either one or two orthogonal directions.

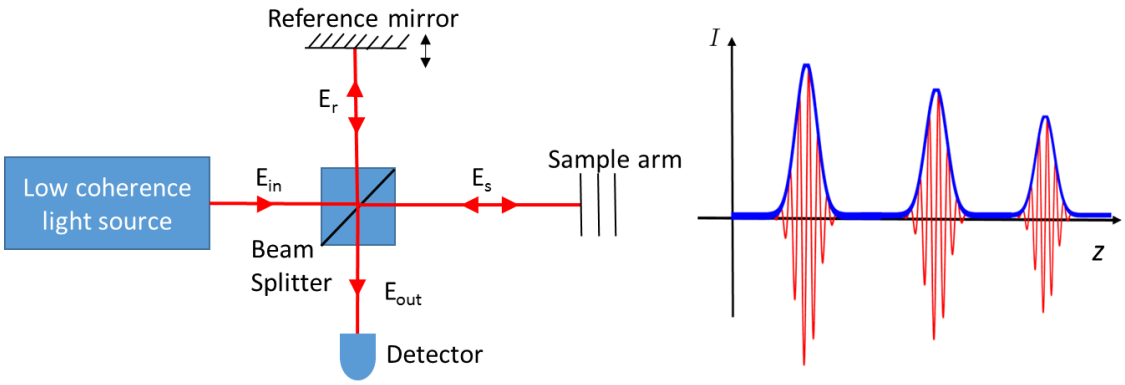

Fig. 1.2 (Left) Basic TDOCT system (based on a Michelson interferometer). E_{in}: incident light; E_r: reference light; E_s: sample light; E_{out}: detected light. (Right) The interference pattern shows up when the optical path length of the reference mirror is nearly equidistant to one of the reflecting structures in the sample.

1.2.2 Fourier domain OCT

Fourier domain OCT (FDOCT), which shares the same basic characteristics with time domain OCT, was capable of directly realize depth resolved structure of the biological tissue without scanning the reference arm. Instead of recording intensity at different locations of the reference mirror, the intensity is recorded as a function of wavelengths or frequencies of the light. The intensity modulations when measured as function of frequency are called spectral interference. The rate of variation of intensity over different frequencies is indicative of location of the different reflecting layers in the samples. It can be shown that a Fourier transform of spectral

interference data provides information of the sample along the depth which is equivalent to the one obtained by moving the reference mirror (Fig. 1.3). Fourier Domain OCT was further divided into two categories: Spectral Domain OCT (a broad band light source and a high speed spectrometer) and Swept Source OCT (a wavelength swept laser and photon detector).

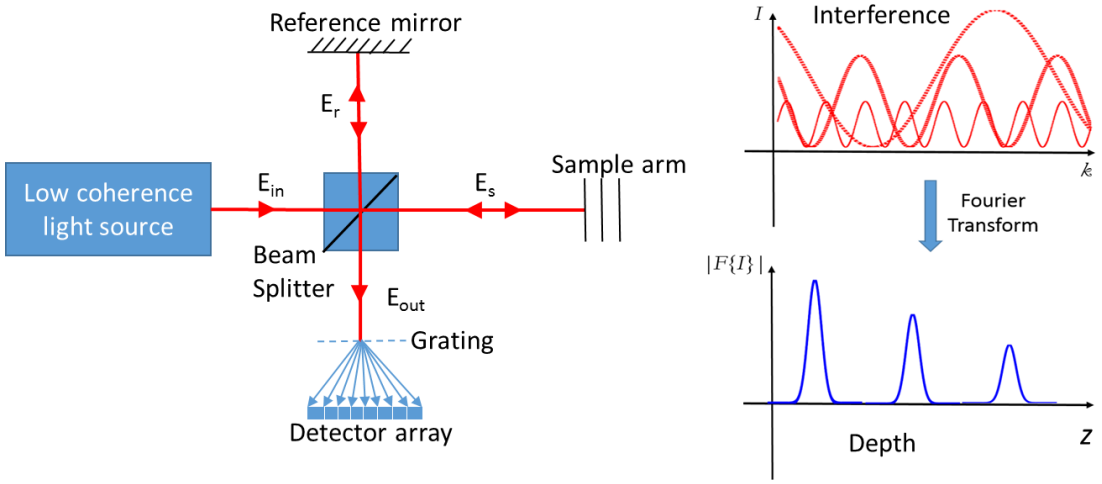

Fig. 1.3 (Left) Basic SDOCT system (based on a Michelson interferometer). E_{in}: incident light; E_r: reference light; E_s: sample light; E_{out}: detected light. (Right) The depth structure (along z-coordinate) of the sample is retrieved from the detected interference fringes by performing a Fourier transform (FT) from *k* to *z* domain.

In Spectral Domain OCT (SDOCT) systems (Fig. 1.3), the reference mirror is stationary, and the interference pattern is split by a grating into its frequency components and all of these components are simultaneously detected by linear detector. The detected interference fringes will be processed using Fast Fourier Transform and the frequency corresponds to the depth and the amplitude corresponds to the reflectivity of the sample. The sample arm beam can be scanned using a scanner to form a 2D cross-sectional image. Fig. 1.4 shows a typical high resolution OCT cross-sectional image of human finger cuticle and nail junction.

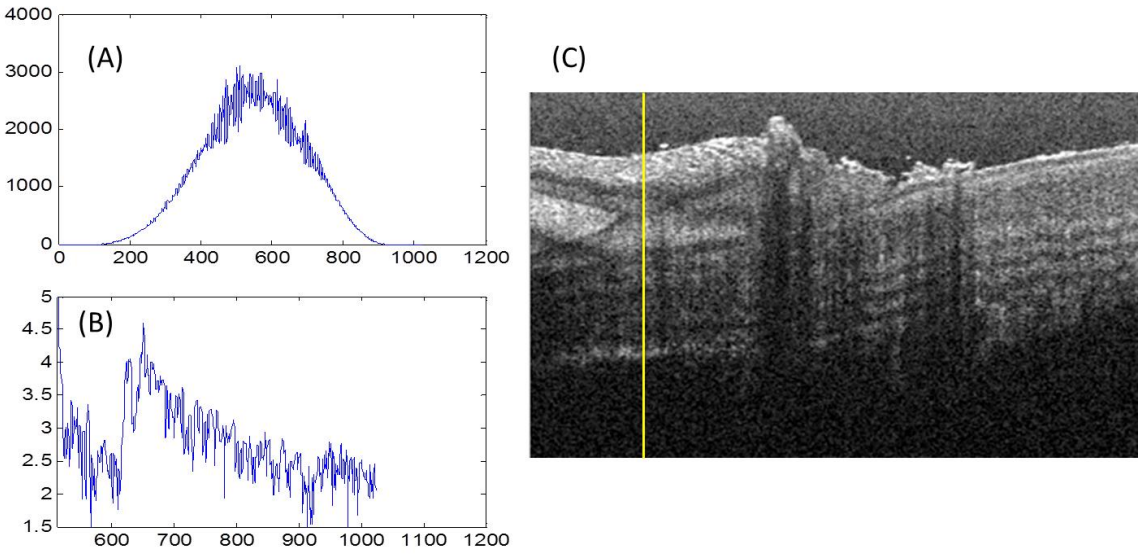

Fig. 1.4 (A) The original interference fringe of SDOCT at the yellow line position. (B) Corresponding FFT spectrum and the amplitude of the spectrum was used to form the OCT image. (C) Typical OCT cross-sectional image of human finger cuticle and nail junction.

Swept Source OCT (SSOCT) systems extract this spectral information by using a frequency scanning (tunable) light source and photodiode detector. It shares the same principle of forming images as SDCOT system. The depth structure (along z-coordinate) of the sample is retrieved from the detected interference fringes by performing a Fourier transform (FT) from *k* to *z* domain. FDOCT has the advantage of an improved signal-to-noise ratio and sensitivity allowing extremely fast-scanning laser systems to increase imaging speed while delivering comparable or improved image quality versus the time domain OCT systems [10, 11]. Since the first report in 2003 [12], FDOCT has gradually become dominant in OCT field, which has been successfully applied on lots of applications.

Based on the analysis above, in this thesis, we will use only FDOCT rather than TDOCT for our study. As compared to SSOCT, one of the biggest advantages of SDOCT is its phase stability. Phase stability is very important for blood flow imaging as we will discuss in the following thesis. Hence, the whole thesis will be based on development and application of SDOCT system.

1.2.3 Essential OCT parameters

The essential parameters that determine the imaging quality of FD-OCT systems are center wavelength & maximum imaging depth, axial resolution, transverse resolution, signal-to-noise ratio (SNR), and sensitivity roll-off in depth.

Firstly, we will discuss the maximum imaging depth of OCT. In scattering tissue and other turbid media, the depth scan is limited primarily by optical scattering, and hence maximum reported imaging depths are between 1 and 3mm for a variety of tissues. Within this range, the maximum imaging depth of OCT systems depends on center wavelength of light source utilized. The light source popularly used for current OCT systems are centered at 820nm, 1060nm or 1310nm. The first two are mostly used for human posterior eye imaging, because the absorption of water is relatively low which allows enough power reach to the retina. Whereas 1310 nm center wavelength are used for imaging other tissues, including skin, brain tissue, coronary artery, etc. 1310 nm can provide deeper penetration depth into tissue as compared to 820 nm light source. We can choose different center wavelength light sources based on specific applications. In this thesis, both 820 nm and 1310 OCT system have developed and utilized.

Secondly, the axial resolution of an OCT system is determined by the center wavelength and wavelength bandwidth of the light source. As we all know, the coherence length *lc* of a broadband light source is given by the following equation:

$$l_c = \frac{2c\ln 2}{\pi}\frac{1}{\Delta\nu} = \frac{2\ln 2}{\pi}\frac{\lambda_0^2}{\Delta\lambda} \approx 0.88\frac{\lambda_0^2}{\Delta\lambda} \tag{1}$$

where λ_0 is the center wavelength, $\Delta\lambda$ is wavelength bandwidth of the light source. Axial resolution of an OCT system is defined as half of the coherence length and given by [12]:

$$R_a = \frac{l_c}{2} \approx 0.44\frac{\lambda_0^2}{\Delta\lambda} \tag{2}$$

From this equation, we can easily found that the smaller center wavelength λ_0 and larger bandwidth $\Delta\lambda$ can provide higher axial resolution.

Thirdly, the transverse resolution of an OCT system is determined by the following equation [13]:

$$R_l = 2W_0 \approx 1.22\frac{\lambda_0}{2NA_{obj}} \tag{3}$$

where λ_0 is the center wavelength, NA_{obj} is the numerical aperture of the objective lens used in the sample arm.

One outstanding property of OCT is the axial resolution is decoupled from transverse resolution. As we know, most optical imaging system use Gaussian beam illumination and the depth of focus is inversely related to the transverse resolution. We can't obtain high transverse resolution with a long depth of focus. Defocus happens outside of the depth of focus and impacts the image quality significantly. Whereas, for OCT, the axial resolution and transverse resolution can be separately controlled, this can be a great advantage. In this thesis, one of the main goals is to improve the system resolution for better visualization of true capillary vessel.

Fourthly, the sensitivity of an OCT system, also called optical dynamic range, can be defined as the ratio of the signal power generated by a perfectly reflecting mirror *P* to the noise of the system [13]. This can be given by the equation:

$$\mathrm{SNR} = \frac{2\alpha^2 \mathrm{P}_S \mathrm{P}_R}{\langle {i_{sh}}^2 \rangle + \langle {i_{ex}}^2 \rangle + \langle {i_{re}}^2 \rangle} \tag{4}$$

with $\alpha = (q\eta/h\nu)$. In a Michelson interferometer with an ideal and symmetric beam splitter (50:50), we have $P_R = P_{Source}R_R/4$ and $P_S = P_{Source}R_S/4$, where P_{Source} is the output power of the light source, R_R the reflectivity of the reference mirror, and R_S the reflectivity of the sample.

Finally, the imaging range of SDOCT is limited by the signal roll-off, which is the attenuation of the OCT signal due to washout of the interference fringe visibility with increasing depth. The roll-off in depth of the SDOCT signal is determined by the spectral content (i.e. full-width-at-half-maximum (FWHM) of the transmission response of a single channel) of the spectrometer and the camera pixel size. The signal amplitude roll-off function is given by [14]:

$$A(z) = \frac{\sin(p*z)}{(p*z)} * \exp(\frac{-z^2}{p*w}) \quad (4)$$

where *p* is a constant, *z* is the depth, and the *w* is equal to 1/N (pixel number of spectrometer) and depends on the optical resolution of spectrometer elements. The first term representing a *sinc* function is a result finite pixel in the spectrometer. The second term is result of finite optical resolution of the spectrometer that results in leakage of a given wavelength into multiple pixels. Both the system sensitivity and signal roll-off are key parameters we need to concern when we build an OCT system. Methods for improving the system sensitivity and reduce the signal roll-off along the depth are discussed in the thesis.

1.2.4 OCT applications

Since its first introduce for human retina imaging by D. Huang et al [9], OCT has been developing fast and applied for many areas. In addition to the improvement in the OCT system hardware and performance, different methods for functional measurements of tissue beds have been developed and demonstrated as well. Here, we will briefly discuss the OCT applications and functional OCT methods which will bring out issues related to the topic in this thesis.

Firstly, OCT application in Ophthalmology is most successful until now. Due to easy optical access to the posterior segments of the eye, OCT has become a widely used imaging technique for Ophthalmology. Currently, structural OCT imaging has become a clinical standard in many areas of ophthalmic clinical diagnosis, such as retinal diseases, age related macular degeneration (AMD), glaucoma etc. One part of this thesis is dedicated to develop system and methods for solving key problems in Ophthalmology. We will discuss in more detail about how OCT could be applied for clinical situations and research in Ophthalmology in the following chapters.

Secondly, another important application of OCT is in cardiology. Cardiovascular disease is the leading cause of death worldwide and it claims hundreds of thousands of life in the U.S. each year [15]. Coronary artery disease (CAD) also known as atherosclerotic heart disease is the result of the accumulation of atheromatous plaques within the walls of the coronary arteries. As the

degree of coronary artery disease progresses, there may be near-complete obstruction of the lumen of the coronary artery, severely restricting the flow of oxygen-carrying blood to the myocardium, which result in acute heart infarction (heart attack) and threaten the human life. Intravascular OCT imaging system for assessment of vulnerable plaques in coronary artery has been FDA approved for application during percutaneous coronary intervention (PCI). LightLab's (now belongs St. Jude Medical) C7-XR Imaging System and C7 DragonflyI Imaging Catheter become first OCT products available to U.S. interventional cardiologists for intracoronary imaging. The most important advantage of intravascular OCT is its high resolution, which can provide more detailed morphological information of arterial wall than any previously available imaging technology including intravascular Ultrasound (IVUS). OCT has shown promise for intracoronary imaging and will definitely play a vital role in diagnosis and treatment of CAD and other cardiovascular diseases.

Thirdly, OCT was also been used in Dermatology for screening of many skin diseases. As skin covers the whole surface of our body, OCT can easily access into the skin tissue. OCT is a promising tool for investigating various types of skin wound as well as the wound healing. In this thesis, we will demonstrate the capability of the developed simultaneous label-free optical microangiography and lymphangiography for monitoring the vascular and lymphatic response to wound punch and healing in a mouse ear flap model.

Last but least, OCT has also been successfully applied in gastroenterology for screening Barrett's esophagus. By differentiating the different optical property of normal and cancerous tissue, OCT can be a useful tool for in vivo biopsy of cancer in Barrett's esophagus.

1.3 Functional OCT

Functional OCT can provide important clinical information that is unavailable in the typical intensity based structural OCT images. Integration of functional extensions with structural information can greatly enhance the capabilities of OCT for a range of applications in medicine. There have been several functional OCT methods including but not limited to: 1) Doppler OCT

(Phase-sensitive OCT measurements), 2) OCT angiography, 3) Polarization Sensitive OCT, 4) spectroscopic OCT etc. In this thesis, we will focus on the first two and develop of a multi-functional OCT system for volumetric and quantitative imaging of vasculature and lymphatics within the microcirculation.

One of the most promising functional extensions of OCT has been the field of functional imaging of blood flow which uses the internal blood flow as contrast. The development of Fourier domain optical coherence tomography (FDOCT) which provides markedly increased imaging speed and sensitivity [16] has enabled *in vivo* imaging of blood flow. The field of OCT for blood flow imaging has generated a lot of interest in the OCT research community during the last few years. Considerable attention in ophthalmic OCT has been paid to the functional imaging of retinal blood flow.

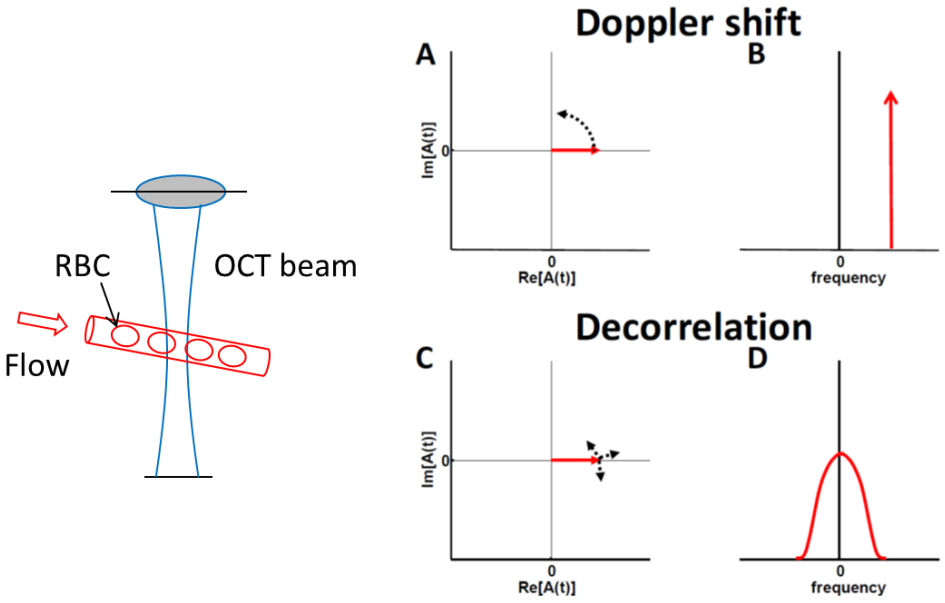

Fig. 1.5 (Left) Schematics of blood flow under OCT beam, RBC: red blood cell. (Right) OCT for blood flow detection relies on the fact that Blood flow is accompanied by both Doppler shifts (A-B) and decorrelation (C-D), leading to both shifting and broadening of the power spectrum.

Fig. 1.5 shows a qualitative visualization of dynamics in the time and frequency domains of blood flow caused Doppler shifts and decorrelation in OCT signal. Doppler shifting (the axial motion of red blood cell) causes a pure rotation of the OCT signal in the complex plane, and leads

to a frequency shift of the power spectrum (A-B). Decorrelation (both axial and transverse motion of red blood cell) causes random deviations of the OCT signal in the complex plane, and leads to a broadening of the power spectrum (C-D).

Currently, functional imaging of blood flow using FDOCT can be divided into two categories: Doppler OCT and OCT angiography. By analyzing the Doppler effect of a flowing particle on light frequency, Doppler OCT allows the quantification of the blood flow speed. The most frequently used Doppler OCT technique to measure blood flow speed is the phase-resolved Doppler OCT (PRDOCT) [17, 18]. On the other hand, in order to visualize the microcirculation network, a number of strategies to enable better contrast of microvasculature components, which we termed OCT angiography, have been introduced during recent years. We will discuss these two functional imaging methods briefly in following paragraphs.

1.3.1 Phase-resolved Doppler OCT

Vasculature can be visualized and quantified by OCT using the effect of motion caused by blood flow on the backscattered light. By analyzing the Doppler effect of a flowing particle on light frequency, Doppler OCT allows the quantification of the blood flow speed. Zhao et al. proposed the phase-resolved DOCT (PRDOCT) method [19], in which by evaluating the phase difference between adjacent axial OCT scans (A-scan), PRDOCT greatly improves the detection sensitivity for imaging the flow velocity by decoupling the spatial resolution and velocity sensitivity. The initial implementation of PRDOCT was based on Hilbert transform, in which the phase of the Doppler signal is determined through the analytic continuation of the measured interference signals by Hilbert transform. By this implementation, a minimum velocity sensitivity as low as 100 μm/s with a resolution of 100 μm/s could be achieved. Moreover, by comparing the sequential A-sans at the same locations, the speckle modulations in the fringe signal cancels each other and will not affect the phase difference calculation. Doppler-OCT has been used for more than a decade to provide contrast due to blood flow. However, Doppler OCT, despite being capable of quantifying blood flow, has several limitations such as limited dynamic range and

dependence of Doppler signal on the angle of probe beam and flow direction. In addition, the pulsatile nature of blood flow can also affect the Doppler signal. Fortunately, OCT extension for visualization of the detailed vasculature, which termed as OCT angiography, has emerged and generated a lot of interest in the OCT research and clinical community during the last few years.

1.3.2 OCT angiography and Optical microangiography (OMAG)

Fluorescein angiography and indocyanine green (ICG) angiography are currently the gold standards for vasculature visualization in the eye. However, the invasiveness of the approach combined with possible complications (allergy to dyes, side effects) make it an unsuitable technique for widespread screening applications in ophthalmic clinics. The field of OCT angiography which provides image of vascular network could enable doctors to obtain new and useful clinical information for diagnosis and management of many diseases in a noninvasive manner. One of the major applications of such techniques has been to generate *en face* vasculature images of the retina. *En face* images are typically generated from three dimensional data cubes by summing pixels along a given direction in the cube, either in their entirety or from sub-portions of the data volume.

Chen et al. demonstrated the use of the Doppler variance technique for the first time to obtain vasculature mapping [19]. Doppler variance, while incapable of quantifying the blood flow, is less sensitive to the Doppler angle and the pulsatile nature of the blood flow. Hence Doppler variance provides better detection for the location of the blood flow. Makita et al. used phase-resolved Doppler OCT to perform OCT vasculature mapping of the human retina [20]. However, these methods use only phase information which is intended to be affected by low image intensity. In addition, noisy signal causes inherently high variations in the phase measurements leading to 'false positive' detection of motion.

Our group developed a novel technique, optical microangiography (OMAG) [21], that applies a constant modulation frequency to the interferograms formed between reference and sample beams to separate the static and moving elements using mathematical properties of Hilbert and

Fourier transformations applied on complex valued interferometric data (Fig. 1.6). This resulted in separation of the vasculature image (due to motion of blood flow) and the tissue image. OMAG is capable of generating 3D images of dynamic blood perfusion distribution within microcirculatory tissue beds. OMAG was initially used for 3D imaging of the cerebral blood flow through the intact skin and skull of mice [22], as well as the microvasculature of the retina and choroid in humans [23]. Subsequently, OMAG was combined with PRDOCT to produce a method called Doppler OMAG (DOMAG), which has extended OMAG's capability to quantitatively measure blood flow velocity (axial component) [24].

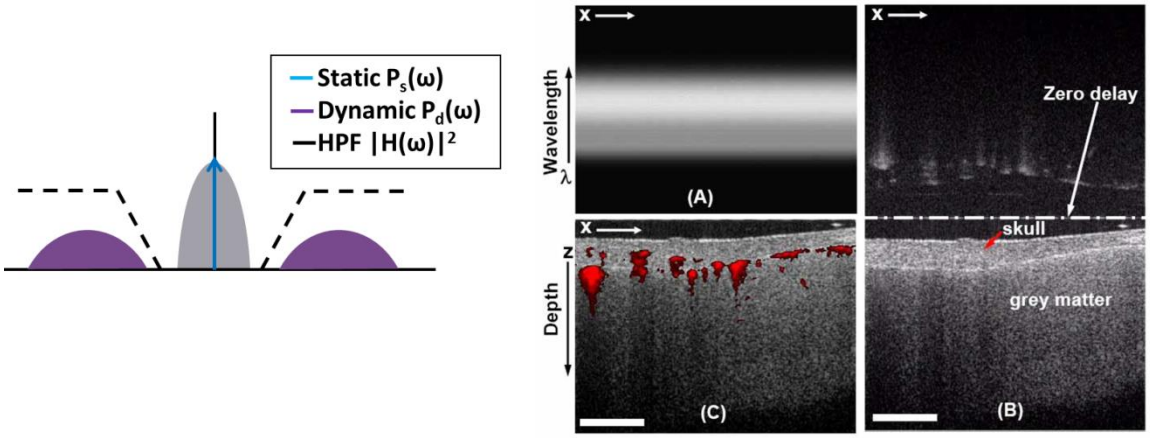

Fig. 1.6 (Left) working principle of OMAG and other high pass filtering based OCT angiography. (Right) Post-processing algorithm for OMAG image: (A) Raw spectrum along λ-x dimension of a typical B-frame; (B) separated static background tissue and dynamic blood flow image; (C) merge of the tissue and blood vessel image.

1.3.3 Lymphangiography

Visualization of the lymphatic system (lymph nodes and lymphatic vessels) plays a significant role in assessing patients with various malignancies and lymphedema [25, 26]. Most current methods for visualizing the lymphatic vessels require exogenous contrast agents [27], including but not limited to whole-mount immunofluorescence (LYVE_1), Evans blue dye imaging, fluorescence imaging, MRI, CT, Ultrasound and Photoacoustic imaging (Indocyanine Green dye as contrast agent) [28]. Unfortunately, the applicability of these methods is limited due to the

difficulty of contrast agent uptake and their potential side effects. There is a need for a noninvasive and label-free method that can image the lymphatic vessel network *in vivo*.

Due to the relative low scattering property of lymph fluid, it appears almost transparent optically. In this regard, an endogenous contrast would be taken advantage by OCT [9], which is an interferometric technology using the intrinsic light scattering as image contrast. In this thesis, we will investigate the capability of OCT as a non-invasive and label-free tool for lymphangiography.

Another issue we wish to address is that to better understand the physiological function of the immune system, it is preferred to study the interaction between lymphatic circulation system and blood microcirculation. This requires high resolution imaging of microstructure, lymphatic and blood vessel network within tissue bed all together. Thus, a multi-functional OCT system is desired for better study of *in vivo* vascular pathology and lymphatic system in both normal and disease conditions.

1.4 Scope of the thesis

The objective of this thesis is to develop a multi-functional OCT system and image processing method, for better visualization of the microcirculation and quantification of the several important parameters related to microcirculation and to further apply it for pre-clinical research applications. The multifunctional OCT system provides multi-functional modalities including structural OCT, OCT angiography, Doppler OCT and Optical lymphangiography, for multi-parametric study of tissue microstructure, blood vessel morphology, blood flow and lymphatic vessel all together. The thesis mainly focus on two parts: first, development of system and methods for volumetric imaging of microvasculature and quantitative measurement of blood flow, and its application for research in ophthalmology on rodent eye models; second, development of ultra-high resolution ultrahigh sensitive optical microangiography (OMAG) system for simultaneous label-free imaging of blood and lymphatic vessel, and its application in wound healing study on mouse ear model.

Chapter 2 describes theory about Doppler OCT and OCT angiography for imaging of vasculature and measurement of blood flow. The time interval used for the Doppler analysis and angiography determines the sensitivity. Different scanning protocols and processing applied can extract different information out of vasculature. A combined OMAG and Phase-resolved Doppler OCT, provides the capability for volumetric and quantitative imaging of vasculature and i*n vivo* study of vascular physiology.

Chapter 3 describes the application of the above described methods for investigating the impact of elevated intraocular pressure (IOP) on retinal, choroidal and optic nerve head anatomy and microcirculation in rat eye model. The purpose of this study is to improve our understanding about the mechanism and development of glaucoma.

Chapter 4 presents a more comprehensive study of the effect of acutely elevated IOP on retinal microstructure, retinal microvasculature and total retinal blood flow in the rat eye model by OCT/OMAG. Improved system resolution and performance enables better visualization of detailed capillary network response to the increased IOP. Quantification of the capillary network density and total retinal blood flow are presented.

Chapter 5 discusses the development of an ultra-high resolution OMAG system using broadband Supercontinuum light source and high NA objective lens to achieve ultra-high resolution microvasculature imaging of biological tissue.

Chapter 6 describes the importance and current status of lymphangiography. A label free imaging modality for lymphangiography is lacking and desired. Methods for simultaneous label free optical imaging of blood and lymphatic vessel was developed based on the ultra-high resolution OMAG system. Its capability was demonstrated by monitoring the blood and lymph response to wound healing on mouse ear pinna model.

Chapter 7 describes an application of optical microangiography/optical coherence tomography (OMAG/OCT) for evaluation of early diabetes-induced changes in retinal thickness and microvasculature in a type II diabetic mouse model. OMAG provides an unprecedented

capability for high-resolution depth-resolved imaging of mouse retinal microvasculature which may play vital role for detecting early microvessel abnormality such as microaneurysms.

Chapter 8 introduces the importance of capillary red blood cell (RBC) flux measurement and a novel approach for measurement of multi-capillary flux simultaneously will be proposed. The developed approach will be applied to measure the RBC flux of capillaries within retina of BTBR *ob/ob* mice, which may pave the way for early diagnosis of Diabetic retinopathy.

Chapter 9 is the summary and future work. In the future, for the first part, we will investigate the long term (8 hours) effect of IOP elevation on the retina, choroid and optic nerve head. The goal would include system performance to better evaluate the microstructure and microvasculature perfusion change within ONH, ONH deformation and biomechanical property change, as well as their effect on development of glaucoma. For the second par, we will further improve the system capability for simultaneous microangiography and lymphangiography and apply it for study tumor environment as well as the development and treatment of metastatic cancer.

Chapter 2. Combined Phase-resolved Doppler OCT and Optical Microangiography for *in vivo* imaging of vascular physiology

In this chapter, I first described how the time interval used for the Doppler analysis and angiography determines the sensitivity. A new scanning protocol and processing method was employed for OMAG which we term as Ultra-high sensitive OMAG (UHS-OMAG) to improve the sensitivity but keeps the total 3D image time minimal. The main purpose is to combine two different scanning protocols that enables simultaneous Doppler OCT and OMAG for the *in vivo* study of vascular physiology. Here, we applied it for *in vivo* imaging of the rat retina as an example, but similar techniques can be used to image and quantify vascular physiology in other organ systems.

2.1 Introduction

2.1.1 Ultra-high Sensitive Optical Microangiography: Sensitivity improvement

OMAG [21] has been demonstrated to be able to image both cerebral vasculature and human retinal and choroidal vasculature. However, the velocity sensitivity of OMAG is still not good enough to image true capillary blood flow. It is critical to improve the sensitivity for slow flow detection. In order to do this, we need to start from how OMAG works.

The working principle of OMAG is to separate the dynamic optical scattering signals from moving particles to those from the static tissue using high pass filtering. According to $V_{Axial} = \Delta\varphi(z,t)\lambda_0/4\pi n\Delta t$, where λ_0 is the central wavelength of the light source and n is the refractive index of the sample, the detectable flow velocity is determined by the time spacing between adjacent interferograms used for velocity calculation. The time spacing could be controlled through modify the exposure time of the camera sensors, while the phase noise of system is determined by the overlapping factor between adjacent A-lines. If flow velocity in a capillary is $v \leq 100\mu m/s$, then it would require $\Delta t \geq \sim 4.7ms$ for the system to have a chance to sample

the blood cells flowing in the capillary, corresponding to a scanning speed of ~213 A scans per second. Therefore, the total imaging time for one 3D capillary flow image of a tissue volume would be prohibitively long, which is not suitable for in vivo imaging.

To solve this problem, ultra-high resolution OMAG (UHS-OMAG) [29] has been further developed that dramatically improves the detection sensitivity of blood flow to a level that enables us to image capillary vessels within the scanned tissue volume. This was achieved by applying the OMAG technology along the slow scan axis, i.e. the time separation between two measurements was now determined by B-frame rate rather than A-scan rate. This allowed increased time difference between two OCT measurements at the same location and hence increased the sensitivity to slower flow. By doing so, the camera can be used at the maximum A-line scan rate which minimize the total 3D image time. Since our OMAG algorithm shifts from B-scan direction to C-scan direction, the time spacing between adjacent interferograms would change from Δt_A (between adjacent A scans) to Δt_B (between adjacent B scans). As the A-scan rate we used here was 47 kHz, and A-line number in each B-scan was 256, the imaging speed achieved was 150 fps, leading to Δt_B = 6.7 ms. Hence, the maximum unambiguous detectable velocity in UHS-OMAG would be ~72 μm/s. That means flow velocity smaller than 72 μm/s could be detected as the time spacing is much longer. On the other hand, the minimal flow velocity that can be detected by the system is determined by the system phase noise floor. With the measured SNR = 105 dB, the minimal detectable flow velocity is ~ 4 μm/s as demonstrated in our previous study [29]. With this ultra-high sensitivity to slow flow, UHS-OMAG has been successfully applied to image microvasculature at the capillary level within human skin [29] and retina and choroid [30], and is now being extended to small animal studies, including imaging of the microvasculature within the meninges and brain cortex [31] and sentinel lymph node [32] in mice.

Apart from UHS-OAMG, there are several OCT angiography methods that utilize inter-frame change analysis of the OCT intensity or phase-resolved OCT data were proposed.

Fingler et al. performed Doppler or phase variance based detection by comparing the phase data at the same location from multiple B-scans or frames [33]. However, inter-frame phase variance analysis method relies only on the phase information in the OCT data to detect motion. One of the limitations of phase only methods is that phase signals have increased error in measurements at low backscattered signal intensity. The OCT data obtained from the light backscattered from the moving scattering particles has variations in intensity as well as the phase. Mariampillai et al. confirmed this by performing vasculature imaging based on inter-frame speckle variance analysis [34]. The amplitude of the light backscattered from the tissue also provides useful information about their optical properties.

Until now, many different kinds of OCT angiography methods have been proposed which generates contrast for blood flow, They can be separated into three different categories, which works on either the phase [20, 35-40] or intensity [41-43] or complex information [21, 44-46] of FDOCT signals. As compared to other imaging method either using just the phase information or intensity information alone, UHS-OMAG which utilizes the complex OCT information can enhance the accuracy and sensitivity for detecting localized motion contrast caused by blood flow.

2.1.2 Combined Doppler OCT and UHS-OMAG for volumetric visualization of microvasculature and quantitative measurement of blood flow

In most cases, it's required to achieve both volumetric visualization of the microvasculature and quantitative measurement of blood flow. UHS-OMAG has been demonstrated to be a great tool for microvasculature imaging and visualization. However, there is a problem for applying UHS-OMAG to quantify the blood flow velocity and flow rate. As we discussed above, the maximum unambiguous detectable velocity (without phase wrapping) in UHS-OMAG through phase analysis between adjacent B-frames would be ~ 72 μm/s (based on the above system parameters). That means flow velocity higher than 72 μm/s couldn't be accurately obtained. A higher

maximum unambiguous detectable velocity (in other word, a shorter time spacing between adjacent interferograms used for velocity calculation) is required to quantify the blood flow velocity in the big blood vessels, especially large arteries and veins. Hence, we still need to use the conventional phase-resolved Doppler OCT technique which calculate the blood flow velocity using the phase change between adjacent A-lines with time spacing $\Delta t_{A.}$ And now, the maximum velocity that can be detected by the system is determined by the system A-scan imaging rate, or more precisely the integration time of the camera used in the study. Here, the imaging speed was of 47,000 A-scans per second. Thus, the blood flow with a maximal velocity of ~30 mm/s would be detectable.

In this chapter, I will develop a combined Doppler OCT and UHS-OMAG for volumetric visualization of microvasculature and quantitative measurement of blood flow simultaneously.

2.2 System and methods

2.2.1 Imaging System description

The SDOCT system setup used to image the retinal microvasculature and provide the quantitative retinal blood flow in rats is shown in Fig. 2.1. A broadband infrared Superluminescent Diode (SLD, Denselight Ltd, Singapore) with a 1310 nm central wavelength and a full width at half maximum (FWHM) bandwidth of 60 nm was used as the illuminating light source. The ex-fiber output power was rated at ~ 8 mW. The light from the SLD was split into two paths with a 10:90 fiber based Michelson interferometer. The ninety percent power path goes to the sample arm while the ten percent power path goes to the reference mirror. The sample arm was scanned by a Galvo mirror in both x and y directions. The objective lens had a 50 mm focal length and the ocular lens had a 30 mm focal length. The probe beam size was adjusted to enable the entire beam to pass through the rat pupil and reach the retina. The lights reflected back from both reference and sample arms meet and interfere with each other at the fiber-coupler, and the resulting interferograms emerging at the output of interferometer was sent, via the optical circulator, to a custom-built high-speed spectrometer. The spectrometer consisted of a

transmission grating (1175 lines/mm), a camera lens with a focal length of 100 mm, and 1024 element line scan infrared InGaAs detector (Goodrich Ltd, USA). The total depth range was measured to be ~2.8 mm in air (2.1 mm in biological tissue by assuming that the refractive index of the sample is ~1.35). The axial resolution of the system was ~13 μm in air (~9 μm in tissue), sufficient to resolve the different morphological layers in the rat retina. With a 3 mm beam size illuminated on the objective lens, the lateral resolution was estimated to be 16 μm at the posterior segment of the eye. The maximal imaging speed of the system was 47,000 A scans per second, with which the measured signal to noise ratio (SNR) was ~100 dB at the focus spot of the sampling beam, which was ~500 μm below the zero delay line.

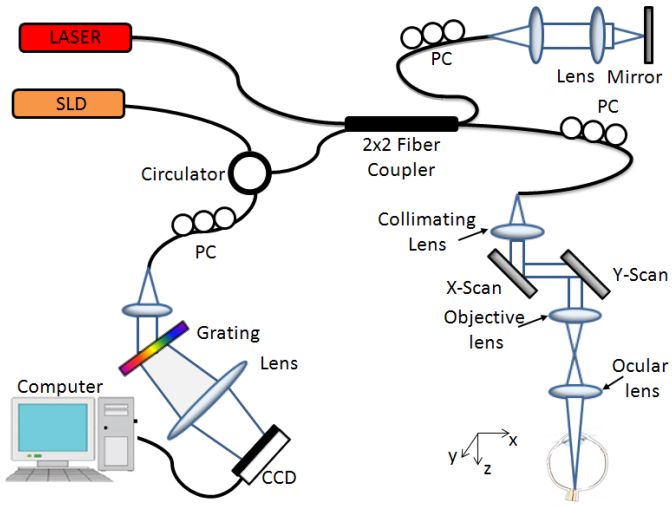

Fig. 2.1 (a) Schematic of the UHS-OMAG system: SLD – super luminescent diode, OC – optical circulator, FC– 10:90 fiber coupler, PC – polarization controller, RM – reference mirror, Laser- pilot laser for beam guiding, DG – diffraction grating, CCD – line-scan camera, COMP – computer. (b) Scanning voltage pattern for Galvo mirror during UHS-OMAG data acquisition.

The 3D scan was achieved by enabling the x-y scanner to provide volumetric morphological and vasculature images through UHS-OMAG, while repeated B-scan (i.e., M-B scan) was achieved by enabling x-scanner only to provide the quantitative blood flow measures on the selected blood vessels on the retina through D-OMAG.

2.2.2 Scanning protocol and image acquisition

Unlike conventional OMAG [21], in order to achieve ultrahigh sensitive imaging of slow microcirculation, UHS-OMAG employed a new scanning protocol and data processing algorithm for image reconstruction. Fig. 2.2 (b) shows the scanning voltage pattern used to drive the Galvo scanner. Firstly, the x-scanner was driven by a 150 Hz saw tooth waveform V_x (red), meaning the imaging rate is 150 frames/sec (fps). In each B scan (i.e. x-direction scan) we acquired 256 A-lines with a spacing of ~10 μm between adjacent lines that covered a size of ~2.5 mm on the retina. Secondly, the y-scanner was driven by a step function V_y (green), and the entire C scan consists of 200 steps, with spacing of ~12.5 μm between steps. In each position (step), we acquired 5 repeated B scans, which was preferred by the UHS-OMAG algorithm. Accordingly, it required only 6.7 sec to acquire one 3D OMAG dataset with the A-line scanning speed of 47 KHz, covering an area of ~2.5x2.5 mm^2 on the retina.

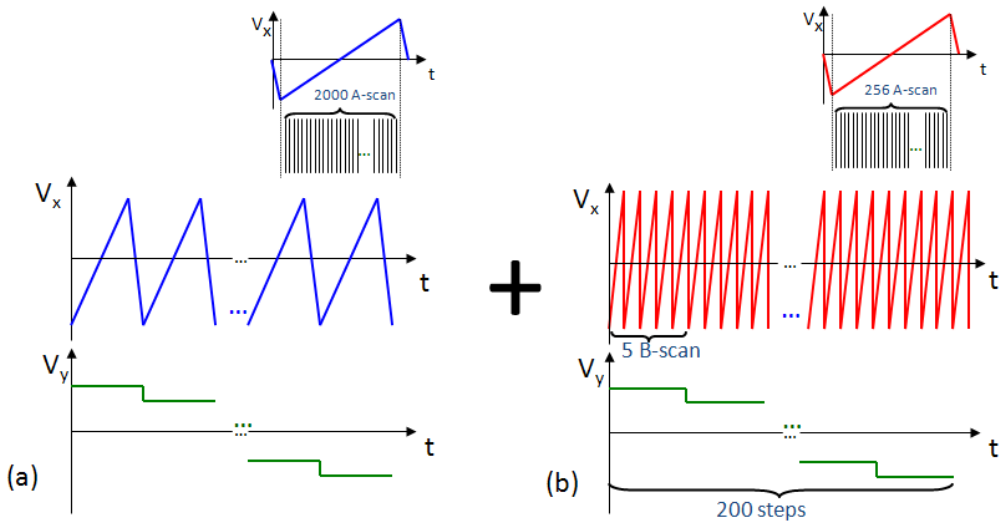

Fig. 2.2 Hybrid scanning protocol (voltage pattern driving Galvo-mirror) we used for OMAG 3D data acquisition. (a) is the scanning protocol for conventional OMAG, and (b) is for UHS-OMAG. The fast scanning Galvo mirror was driven by a saw tooth signal (V_x) while the slow scanning mirror driven by a step function (V_y).

2.2.3 3D volumetric perfusion imaging using UHS-OMAG

In our previous work, UHS-OMAG was successfully applied to obtain 3D volumetric perfusion images of the scanned tissue volume, including human skin tissue [29], and human retina and choroid [30], and this allowed detailed, capillary level resolution visualization of the perfused microvasculature. Here, in order to image not only fast flow vessels but also slow flow capillaries within the rat retina, we adopted this UHS-OMAG scanning protocol and its data processing algorithm to achieve high quality 3D volumetric perfusion imaging. In addition, the high quality 3D image of the vasculature provides us the ability to determine the Doppler angle that is required to provide the quantitative measures of the blood flow in individual vessels. Here, UHS-OMAG was used to acquire low density B-scan frames (i.e. x-direction scan) with 256 A-lines at a spacing of ~ 6 μm (which is of the order of the least sampling distance of 8 μm for the system's lateral resolution of 16 μm) between adjacent A-lines. This covered a total x-scan range of ~1.5 mm on the retina. Notably, the line scan camera employed in the spectrometer runs at an A-line scan rate of 47 KHz, providing an imaging speed of 150 frames per second (fps) with 256 A-lines in each frame. The whole 3D data volume containing 200 cross-sections with a spacing of ~ 6 μm covered a y-scan range of 1.2 mm. To facilitate the UHS-OMAG data processing, two frames were acquired at each cross-section; 400 frames in total were acquired in one whole 3D data volume, which took ~2.5 seconds.

In the data processing, the essential principle of UHS-OMAG is the same as the traditional OMAG [21], except that UHS-OMAG applied high pass filtering along the C-scan direction, rather than the B-scan direction. As mentioned in [24], regardless of DC component and sample arm self-cross-correlation, the interferograms of one B-scan captured by the CCD camera can be expressed by the following equation:

$$I(k_j,t) = 2S(k_j)E_R\left[\int_{-\infty}^{\infty} a(z,t)\cos(2k_j nz)dz + a(z_1)\cos(2k_j n(z_1 - vt))\right] \quad (1)$$

where *j = 1, 2, ... 1024* is the pixel number index of the CCD camera, and k_j is the wavenumber captured by the j^{th} pixel; t is the time point when an A-line was captured. E_R is the light reflected from the reference arm; S (k) is the spectral density of the SLD light source used; a (z, t) is the amplitude of the back scattered light at depth z; n is the average refractive index of tissue, assumed to be constant; v is the velocity of moving blood cell, which is located at depth z_1 moving towards depth z. For the conventional OMAG method, the high pass filtering was applied along the fast scanning B-scan direction, to isolate the scattering signal from moving blood cells from the static tissue. Here, we switched this process to the slow scanning direction i.e. C-scan direction. According to previous analysis [47, 48], the sensitivity to the flow velocity is determined by the time spacing between adjacent interferograms used for velocity calculation. Since our OMAG algorithm shifts from B-scan direction to C-scan direction, the time spacing between adjacent interferograms would change from Δt_A (between adjacent A scans) to Δt_B (between adjacent B scans). In this case, the time spacing is increased by 256 fold, leading to a dramatic improvement in the sensitivity to the slow blood flows.

Since we acquired two B-scans in each cross-section along the C-scan direction, a differential operation was applied to the subsequent B-scan at each cross-section. This can be described by the following equation:

$$I_i(t,k) = I(t+\Delta t_B, k) - I(t,k), i = 1,2,3...200 \quad (2)$$

where $I_i(t,k)$ denotes the flow signal at i^{th} cross-section (totally 200 cross-sections) along the C-scan direction, Δt_B is the time interval between adjacent B-scans. As the differential operation is equivalent to the high pass filtering, it suppresses the optical scattering signals from the static elements. Then, by applying fast Fourier transforms (FFT) upon every wavenumber *k* of $I_i(t,k)$, we can obtain the depth resolved OMAG flow image for each cross-section with ultra-high sensitivity to the blood flow. With all the cross-sectional images, 3D volumetric perfusion map,

i.e., 3D microangiogram was rendered using Amira 3D visualization software (Visage Imaging, Inc.).

2.2.4 Axial velocity measurement with Doppler OMAG

While UHS-OMAG can provide microangiograms for visualizing perfusion at capillary level resolution, the measurement of the blood flow velocity would be difficult because the time interval used between adjacent frames is in a range of milliseconds, which is too long for measuring fast flows. PRDOCT has been widely studied for the measurement of blood flow velocity. D-OMAG [24] was developed to measure the axial blood flow velocity for relatively fast flows. Since the OMAG algorithm enables us to separate the scattering signals by moving elements from those caused by the static elements, D-OMAG can apply the phase analysis algorithm purely on the scattering signals from the moving blood cells. The resulting phase map is free of texture pattern noise and the performance of blood flow velocity measurement can be dramatically improved [18].

The axial flow velocity can be derived from phase differences between adjacent A-scans introduced by the motion of blood cells. The relationship between them is:

$$V_Z = \frac{\Delta\varphi \cdot \lambda_0}{4\pi n \Delta t_A} \tag{3}$$

where $\Delta\varphi$ is the phase difference between adjacent A-scans; λ_0 is the central wavelength of the light source; n is the refractive index of tissue (~1.35); Δt_A is the time interval between adjacent A-scans as mentioned above. Phase wrapping happens if $|\Delta\varphi| \geq \pi$, hence, the maximal axial velocity component which can be unambiguously measured with a given time interval Δt_A would be:

$$V_{Z\max} = \pm \frac{\lambda_0}{4n\Delta t_A} \tag{4}$$

The reason why we choose to calculate the phase difference between adjacent A-scans rather than adjacent B-scans is because in this study we wished to focus on the quantitative analysis of retinal arteries and veins rather than capillary vessels. In order to avoid phase wrapping in the big arteries and veins, shorter time spacing is required. The A-scan rate we used to do D-OMAG was 47 KHz, then Δt_A = ~20μs, which gives an axial velocity range of [-11.75 11.75] mm/s. This range is sufficient to measure the axial velocity component of retinal arteries and veins in the rat.

2.2.5 Absolute flow velocity and blood flow rate calculation

Measurements of absolute flow velocity and retinal blood flow rate are an important endpoint in studies in ophthalmology, since they allow the evaluation of blood flow dynamics in vessels. Towards the aim of monitoring the dynamic changes of RBF under certain disease conditions, we will next describe the methods used to calculate these two parameters.

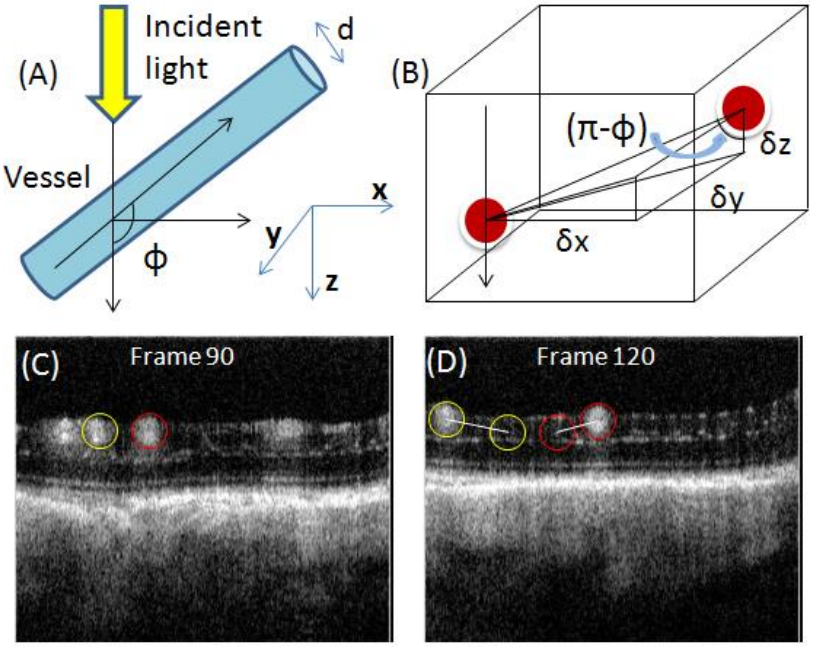

Fig. 2.3 Calculation of Doppler angle of blood vessel from the 3D data volume. (A) Illustration of the defined vessel Doppler angle. (B) Schematic representation of the vessel Doppler angle calculation. (C, D) Two cross-sections of UHS-OMAG blood flow image along the C-scan direction. The three components used for Doppler angle calculation could be obtained for the two vessels circled with two different colors.

Firstly, in order to calculate the absolute flow velocity, besides the axial velocity that we can obtain using D-OMAG as discussed above, the Doppler angle also needs to be known. Doppler angle φ is defined as the angle between the flow-velocity vector and the wave vector of incident light, as shown in Fig. 2.3(A). Many descriptions have been published about how to calculate Doppler angle. [49-51] However, they require complex data acquisition and processing procedures, and the accuracy of the calculated Doppler angle is far from ideal. In our method, we calculated the vessel Doppler angle using the three dimensional data set captured using UHS-OMAG, where the orientation of each vessel is provided in the whole 3D volume. Fig. 2.3 (B) is a schematic of this method. Assuming that the orientation of the artery or vein in the retina doesn't change within a small range, which we found to be true (within 100 μm in this work), the Doppler angle can be calculated according to the following equation:

$$\phi = \pi - \arccos\left(\frac{\delta z}{\sqrt{\delta x^2 + \delta y^2 + \delta z^2}}\right) \tag{5}$$

Where δx, δy, δz are the three components indicating the distance that the vessel meander in the three coordinates of the 3D volume. They can be obtained from the 3D data volume captured using UHS-OMAG. Fig. 2.3 (C) and (D) show two cross-sections of a UHS-OMAG blood flow image along the C-scan direction from one 3D scan where the Doppler angle of the two circled vessels could be calculated. We calculated δx, δz by defining how many pixels the vessel traveled in both x and z direction and multiplying them with the pixel size, while δy could be calculated by multiplying the frame number difference with the spacing between adjacent frames in C-scan direction.

After the Doppler angle is obtained, the calculation of the absolute flow velocity is straightforward:

$$V = \left|\frac{V_Z}{\cos\phi}\right| \tag{6}$$

Here, the absolute velocity V does not take into account the flow direction, since this can be determined from the Doppler angle.

Secondly, in order to calculate the blood flow rate, the vessel diameter D needs to be known apart from the absolute velocity. For each vessel, its diameter was determined from the UHS-OMAG image in the region between the upper and lower boundary of the vessel [52]. In our image the length ratio in the axial dimension is 3.7μm/pixel, which provides a measurement accuracy of 3.7μm for the vessel diameter. With the diameter, we were able to calculate the vessel cross-sectional area size, $S=\pi*(D/2)^2$. The blood flow rate was then calculated by multiplying the absolute average velocity $\bar{V}$ by the cross-sectional area S of the blood vessel.

$$Flow\,Rate=\bar{V}\bullet S \tag{7}$$

2.3 Results and Discussion

2.3.1 3D volumetric imaging of microvasculature

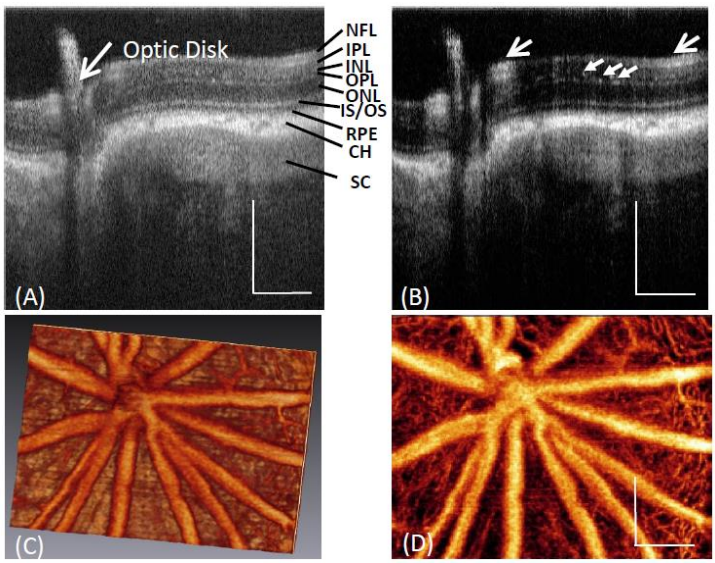

Fig. 2.4 Typical *in vivo* 3-D vasculature perfusion image of the rat retina using UHS-OMAG. (A) One typical cross-sectional structural image of a rat eye around optic disk, where the different layers of posterior segment of the rat eye are demarcated; and the corresponding (B) UHS-OMAG flow image. (C) 3D vasculature perfusion image and (D) the maximal projection map of vasculatures in the rat retina. White bar= 250 μm.

One typical *in vivo* 3D microvasculature perfusion image of posterior wall of a rat eye, including the optic disk, using UHS-OMAG is shown in Fig. 2.4. Fig. 2.4 (A) presents a typical OCT cross-sectional structural image, where the important histological layers can be identified. These include the nerve fiber layer (NFL), inner plexiform layer (IPL), inner nuclear layer (INL), outer plexiform layer (OPL), outer nuclear layer (ONL), junction between the inner and outer segment of the photoreceptors (IS/OS), retinal pigment epithelium layer (RPE), choroid (CH) and sclera (SC). Fig.2.4 (B) is the corresponding blood flow image showing big vessels (retinal artery and vein) represented by large open arrows and capillary vessels as pointed by the small arrows. Fig. 2.4 (C) is the rendered 3D vasculature map of retinal blood vessels and Fig. 2.4 (D) is the corresponding maximal projection view which shows a detailed vessel network, an appearance typical in the rat eye as described in a standard textbook.

2.3.2 Absolute blood flow velocity and flow rate measurement within the rat retina

Fig. 2.5 shows representative results for absolute velocity measurement of retinal blood vessels. Fig. 2.5 (A) is the microangiogram of microvasculature of normal rat retina *in vivo*, where the middle line marked in the image indicates the position where the D-OMAG data were captured for absolute velocity calculation. By applying the D-OMAG algorithm on data captured at the cross section, we obtained the phase difference map as shown in the upper row of Fig. 2.5 (B), while the picture in the lower row is the phase map for the 200 repeated B-scans rendered in 3D, where red and green indicates the two different flow directions and a deeper color represents larger phase difference, meaning faster flow. Three vessels were identified for absolute velocity calculation, among which vessels 1 and 3 are arteries and vessel 2 is a vein. This can be confirmed as the absolute blood flow velocity of vessel 1 and 3 is higher than vessel 2 as shown in Table 1. Fig. 2.5(D) plots the axial velocity profile of vessel 2 along the depth direction indicated by the vertical line across the center of the vessel in Fig. 2.5(B), along with the parabolic polynomial curve fitted to the measured profile. The axial velocity of each vessel at

each time point was calculated by averaging over the whole cross section of the vessel, i.e. the average flow velocity. The measured axial velocities in the three vessels over the time duration of 20 seconds (200 time points with a frame rate of 10 fps) are plotted in Fig 2.5 (E).

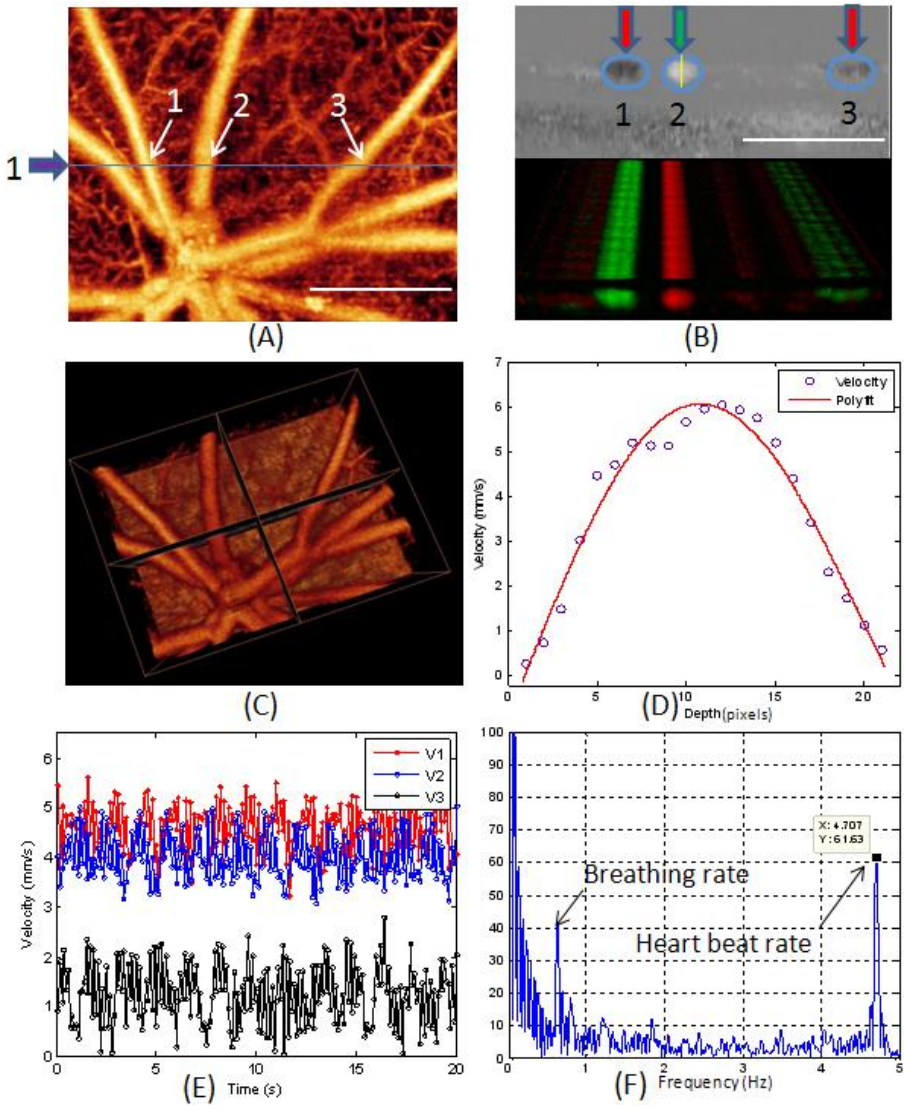

Fig. 2.5 Measurement of absolute velocity within retinal blood vessels in rats. (A) Microvasculature angiogram of a normal rat retina *in vivo* where the blue line and arrows indicate where the D-OMAG data were captured. (B) DOMAG phase difference map in one cross section (upper row) and the 3D rendered phase difference extended in 20 seconds at the same cross section. C) 3D vasculature image showing the vessel orientation that was used for calculating the Doppler angle and vessel diameter for the vessels analyzed. (D) The axial velocity profile of vessel 2 along depth direction. (E) The axial velocities in the three vessels over 20 sec periods and (F) the FFT of the values for V2 in Fig. 2.5E. White bar= 500 μm.

For each vessel, there is variation in the velocity due to flow pulsatility [53] which is caused by the heartbeat and breathing of the animal. Fig. 2.5 (F) is the plot of the Fourier transformation of the values of V2 in Fig 2.5 (E). We can see that there is a peak at 4.7 Hz which is identified to be the heart beat rate (for a rat the heart beat rate is around 280 beats per minute). Also there is another peak at 0.56 Hz which we interpret to be due to breathing. The mean value of the velocities over 20 seconds was calculated as the final axial velocity for each vessel. This increases the accuracy of quantitative blood flow measurement by minimizing the errors caused by the flow variation due to the heartbeat and breathing of the animal.

Fig. 2.5 (C) is the 3D vasculature image showing the vessel orientation where the Doppler angles of the three vessels at the cross section were calculated. The quantitative results for the central axial velocities, Doppler angle, vessel diameter, central absolute velocities and the blood flow rate in the three vessels labeled as 1(artery), 2 (vein) and 3(artery) in Fig. 2(B) are shown in Table 2.1.

Table 2.1 Quantitative results of the blood flow for the retinal artery and vein.

vessel #	Axial velocity (mm/s)	Doppler angle	Vessel diameter (μm)	Absolute velocity (mm/s)	Flow rate (μl/min)
#1	4.6	79^o	55.5	24.0	1.74
#2	4	120^o	70.3	11.7	1.36
#3	1.44	86^o	51.8	20.49	1.30

2.4 Summary and Future work

In this chapter, we first introduce the two category of functional OCT imaging technique which uses internal blood flow as contrast. PR-DOCT for axial blood flow velocity measurement and OCT angiography for visualization of detailed blood vasculature within tissue beds. In order to better characterize the vascular information, we combined the two techniques with a hybrid

scanning protocol and image processing method. We then applied the system and method for *in vivo* image of rat retina and achieved to provide 3D angiography of microvasculature within retina as well as measurement of absolute blood flow velocity and flow rate in retinal arteries and veins.

In the future work, we will also apply the system and method for the evaluation of impact of elevated intraocular pressure on retinal, choroidal and optic nerve head anatomy and microcirculation (chapter 3).

Chapter 3. Impact of elevated intraocular pressure on retinal, choroidal and optic nerve head blood flow investigated by Optical microangiography

3.1 Introduction

Perfusion of the retina, choroid and optic nerve head (ONH) is critical to maintaining normal vision, and reduction in perfusion may contribute to the development and progression of various ocular diseases, including glaucoma [54-56]. The development of non-invasive methods for assessing blood flow in these structures is therefore important for both patient care and research. Many different methods have been used to visualize and measure directly or calculate indirectly *in vivo* ocular blood flow (OBF). Laser Doppler velocimetry (LDV) [57-59] is used to measure RBF velocity by using a laser beam directed at a specific blood vessel, and the Doppler shift caused by moving red blood cells allows blood speed to be measured. However, this method only provides information on flow in a single vessel, but no information about perfusion in the rest of the eye. Unlike velocimetry, laser Doppler flowmetry (LDF) [60-62] can measure relative velocities, numbers of red blood cells and flux at a fixed spot, particularly in capillary beds with the laser directed to areas between larger vessels, and it has often been used for blood flow measurement in the optic nerve [63-66]. One main drawback of LDF is that measurements are limited to a small selected area and the exact volume of the tissue being measured is unknown, which restricts the reproducibility of measurements with this technique [54].

Optical coherence tomography (OCT) [9] is a non-contact, non-invasive imaging modality that has been widely used for human eye imaging [67, 68] and, when combined with the Doppler principle, can be used to measure retinal blood flow.[53, 69, 70] As a variation of Spectral-domain optical coherence tomography (SDOCT), Optical microangiography (OMAG) [21] is capable of generating 3D dynamic perfusion images of tissue microcirculation. When combined

with phase-resolved analysis methods developed for Doppler OCT [71], it produces Doppler OMAG (D-OMAG) [24] that can be used for quantitative and directional blood flow imaging. Recently, it has been refined into ultra-high sensitive OMAG (UHS-OMAG) [29, 30] which has the capability of imaging capillary vessels with speed as slow as 4 μm/s. The combined use of D-OMAG and UHS-OMAG to provide simultaneous 3D angiography and quantitative measurement of blood flow in rat retinal blood vessels has recently been described [72].

Glaucoma is currently estimated to affect nearly 3% of the world's adult population, with a significant economic and individual impact [73]. Despite its prominent contribution to worldwide blindness, mechanisms of optic nerve damage in this condition are incompletely understood, although recent refinements in existing models of primate glaucoma [74] and development of several experimental and spontaneous glaucoma models in rodents [75, 76] are improving our knowledge of the retinal and optic nerve head responses to elevated intraocular pressure (IOP) [77, 78]. Because elevating IOP is also known to affect retinal and ONH perfusion [72, 79], visualizing and measuring these blood flow effects become increasingly important, if we are to fully understand the range of mechanisms that may be contributing to nerve damage in glaucoma. The purpose of this study is to demonstrate the ability of OCT/OMAG to image the tissue and vascular anatomy of the rat retina, ONH and surrounding choroid and investigate the effects of acutely elevated IOP on this anatomy. In addition, we will present quantitative measurements of the effect of elevated IOP on these important vascular beds, as determined by this technique.

3.2 Material and Methods

3.2.1 Animal Model

All animals were treated in accordance with the ARVO Statement for the Use of Animals in Ophthalmic and Vision Research. Adult Brown Norway rats (N=6), anesthetized with inhalational isoflurane (1.5%) mixed with 80% air and 20% oxygen, were positioned for OCT/OMAG imaging in custom-made head holders. IOP was elevated by cannulation of the anterior chamber with a 5 millimeter long 31 gauge needle connected to a reservoir filled with

balanced salt solution and to a calibrated pressure transducer. The height of the reservoir was used to elevate IOP, as determined by the transducer, in 10 mm Hg increments, from 10 mm Hg (treated as baseline) to 80 mmHg followed by a pressure of 100 mmHg which produced complete obstruction of ocular blood flow. After that, IOP was reduced back to 10 mmHg to examine reperfusion. In separate experiments, double-cannulated closed artificial chambers and anterior chambers of anesthetized animals were connected with one cannula (via a 23 gauge needle) to a pressure transducer and the other (via a 31 gauge needle) to a suspended reservoir and second transducer, as described above. Over a range of reservoir heights and pressures, both transducers demonstrated excellent agreement (data not shown). During the whole process, animal position was unchanged and there was no apparent eye movement. After the in vivo imaging session, each animal was euthanized.

3.2.2 Optical coherence tomography/Optical microangiography system

The OMAG system we applied here has been described in detail in chapter 2. Here we will briefly provide parameters that specifically determine the system performance for imaging the rat eye. The system was operated at a wavelength of 1300 nm, in contrast to conventional OCT systems that normally use 800 nm wavelength light source for imaging. Since the water absorption over the short length of the rodent eye is not significant enough to reduce the system sensitivity, we demonstrate that 1300 nm, in addition to an 800 nm light source, can be used for the rodent retinal imaging, opening up new choice of light source. The axial resolution is 12 μm and the lateral resolution is ~ 16 μm in air. The maximal imaging speed of the system was 92,000 A scans per second, which is nearly doubled compared to the one we applied previously [72]. At this A scan rate, the measured signal to noise ratio (SNR) was ~100 dB at the focus spot of the sampling beam, which was ~500 μm below the zero delay line. The total depth range was measured to be ~2.8 mm in air (which is equivalent to 2.1 mm in biological tissue, assuming a

sample refractive index of ~1.35) and the power incidence on the sample was measured to be ~1mW.

3.2.3 Image acquisition and processing

For all image acquisition, the pupil was dilated with 1% tropicamide and 2.5% phenylephrine eyedrops, and the position of the rat eye was kept stationary using a custom-made animal holder during the entire process of IOP elevation. At each IOP level, 3D data volumes covering the ONH area with a size of ~ 1x1 mm^2 were first captured using the UHS-OMAG scanning protocol [80], in which the raster scanning of the beam spot was performed to capture 256 A-lines within each B-frame (2D cross-sectional image) and 1000 B-frames for each C-scan (3D image). Using a frame rate of 280 frames per second (fps), we were able to obtain a single 3D data volume in only 3 seconds, which helps minimize motion artifact. We then applied repeated B-scans (using 3000 A-lines per B-frame and a frame rate of 10 fps) at one cross-section (1 mm) for D-OMAG analysis [24, 81] to determine the axial blood flow velocity in selected retinal arteries/veins. This switch between UHS-OMAG and D-OMAG imaging protocols was automatically controlled by the controlling software written in Labview. At each IOP level, after the height of the reservoir was increased, we waited about 1 minute before OCT scans were taken. This will ensure that the IOP could be stable when the OCT scans are taken.

3D blood flow images were reconstructed from the 3D data volumes by applying high pass filtering along the slow scan direction to separate the moving blood flow from static tissues. Since we shifted the high pass filtering process from the fast scan direction to the slow scan direction [82], the time interval available for Doppler analysis was increased from 0.01 ms (between adjacent A-lines) to 3.57 ms (between adjacent B-frames), which dramatically improved the sensitivity of the system to slow flow movements, enabling us to image capillary flow within the retina and ONH.

3.2.4 RBF, choroidal and ONH blood flow calculation

The method we used for RBF calculation has been described in detail [72]. We selected specific retinal arteries/veins for blood flow calculation. The axial velocity of each vessel was determined from a D-OMAG cross-sectional phase image by calculating the phase difference between adjacent A-lines. The axial velocity V_Z can be given as

$$V_Z = \frac{\Delta\varphi \cdot \lambda_0}{4\pi n \Delta t_A} \tag{1}$$

where λ_0 is the central wavelength, n is the refractive index, $\Delta\varphi$ is the phase difference between adjacent A-lines and Δt_A is the time interval between adjacent A-lines. Doppler angle and blood vessel diameters were determined from the 3D vasculature maps. Absolute blood flow velocity was then calculated from the obtained axial velocity component after being corrected by the Doppler angle of the vessel. We then calculated blood flow rate for each vessel by multiplying the absolute velocity with the area of the vessel cross-section. In order to better assess the effect of IOP on RBF, the flow rates at each level of IOP were normalized and expressed as a percentage of the baseline reading (10 mmHg). In this manner, to evaluate the effect of acute changes in IOP on RBF, we calculated blood flow changes of 15 arteries/veins from a total of 6 animals.

Five eyes provided images adequate to allow us to visualize the peripapillary choroid. Using pixel density as a measure of perfusion, we quantitated changes in peripapillary choroidal perfusion with increasing IOP by measuring the area of choroidal filling at different IOP levels and calculated this as a percentage of area of choroidal filling at baseline (10 mmHg).

For ONH blood flow quantification, since most blood vessels within ONH are capillaries, we were unable to calculate flow in individual blood vessels, as done for RBF. Because OMAG is sensitive to moving particles only, and can separate the blood flow signal from surrounding static tissue, we were able to delineate the flow map using the blood flow signal only. Hence, we

elected to quantify ONH perfusion by calculating blood flow volume as a percentage of ONH volume as follows. The ONH shape, to an approximate depth of 150 μm posterior to the choroidal opening, was first segmented from the anterior view 3-D vasculature map using Amira 3D software (Visage Imaging, Inc.). We then set a threshold to obtain a binary 3D flow map where 1 represents area with flow and 0 represents area with no flow. ONH perfusion was then quantified as the percentage of the voxel numbers showing flow signal divided by the total voxel numbers of the segmented ONH volume. More description of this process is presented in the results section, together with images.

Note that the analysis of the microstructures and blood perfusion from each animal were performed on the same 3D OMAG scan. However, for the retinal blood flow measurement, we need to take extra scans for Doppler analysis to measure the RBF flow velocity. The switch between the 3D scan and Doppler flow measurement scan was automatically controlled by our controlling software, with a time interval less than 1 second.

3.3 Results

3.3.1 ONH, retina and choroidal anatomy viewed by OCT/OMAG

OCT/OMAG is capable of producing 3D images of the structure and vasculature of posterior rat eye. The cross-sectional OCT structural image (Fig.3.1 A) shows a typical anatomy of the rat eye with labeled layers and optic nerve head (ONH) area. The different layers we identified from the image are the nerve fiber layer (NFL), inner plexiform layer (IPL), inner nuclear layer (INL), outer plexiform layer (OPL), outer nuclear layer (ONL), inner/outer segment (IS/OS), retinal pigment epithelium (RPE), choroid (CH) and sclera (SC). Here, the 1300 nm wavelength light source provides an increased penetration depth, as demonstrated by visualization of the sclera and extra ocular muscles. Combining this structural image with the reconstructed 3D image (Fig.3.1 B) we are able to identify some additional important features of the anatomy, such as the central retinal artery (CRA) and posterior ciliary artery (PCA), arrows in Fig.3.1 A. Viewed posteriorly (Fig.3.1 C), a typical UHS-OMAG image focused approximately 150 μm posterior to the opening

of the choroicapillaris demonstrates that the rat CRA enters the globe inferior to the ONH, which has a horizontally oval or kidney bean shape. Here, the CRA appears lucent in the UHS-OMAG image because blood is moving axial to the OMAG unit, making the flow too fast to be detected by the system, and leading to signal washout. The maximal-intensity projection maps can be viewed anteriorly to see the retinal and choroidal microvasculature (Fig.3.1 D). A reduced view of the retinal vessels (Fig.3.1 E) illustrates their relationship to the choroidal opening at the ONH. The choroid and choriocapillaris consist of a dense capillary bed and appears homogeneous, except for the choroidal opening (Fig 3.1. F). A detailed retinal capillary vessel network can be seen clearly from the retinal microvasculature map alone (Fig 3.1. G).

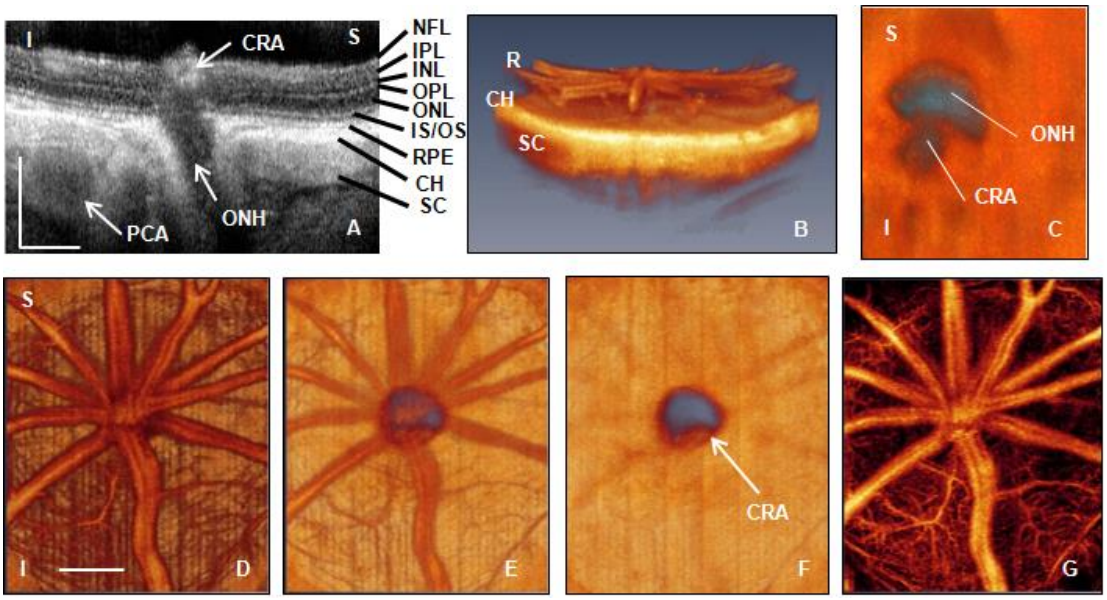

Fig. 3.1 (A) Cross-sectional OCT structural image shows the layers and ONH anatomy of rat eye. See text for abbreviation definitions. (B) 3-dimensional rendering of OMAG images, showing the microvasculature of the retina (R), choroid (CH) and sclera (SC). (C) Posterior view of UHS-OMAG image approximately 150 μm posterior to the opening of the choroicapillaris, showing that the rat central retinal artery (CRA) enters the globe inferior to the ONH. (D–G) Maximal projection maps of the 3-D microvasculature viewed anteriorly as: (D) a combined projection of the retinal and choroidal microvasculature; (E) a reduced view of the retinal vessels to illustrate their relationship to the choroidal opening at the ONH; (F) the choroid and choroicapillaris after removal of retinal vessels, with arrow pointing to the CRA in the inferior aspect of the opening; and (G) retinal microvasculature alone. White bar = 250 μm.

3.3.2 Effect of elevated IOP on ONH contour

By continuously capturing data at the same longitudinal section, we were able to evaluate the ONH contour change from the OCT structure images at different IOPs (Fig.3.2). Here, we termed contour change as a change in the observed surface curvature, compressed retinal and choroidal layers and a distortion of the CRA. When the IOP was lower than 50 mmHg, no apparent contour change was observed. However, IOPs above 60 mmHg progressively compressed the adjacent retina (R) and choroid (CH) and distorted the CRA posteriorly, along with apparent compaction of the ONH. All of these effects resolved completely when IOP was returned to baseline. Horizontally oriented views (Fig.3.3) at progressively higher IOPs clearly showed posterior bowing of the retina and choroid around the ONH and posterior displacement of the central retinal vessels (*) into the ONH. Dashed yellow lines were drawn in each panel to serve as a reference (top line: original RPE layer surface; bottom line: ~ 300 μm down to the top line) to measure the distortion of the CRA into the ONH. At 80 mmHg we observed an approximately 80 μm displacement, as denoted by the white arrow point from the original RPE layer surface to the new location (around ONH only).

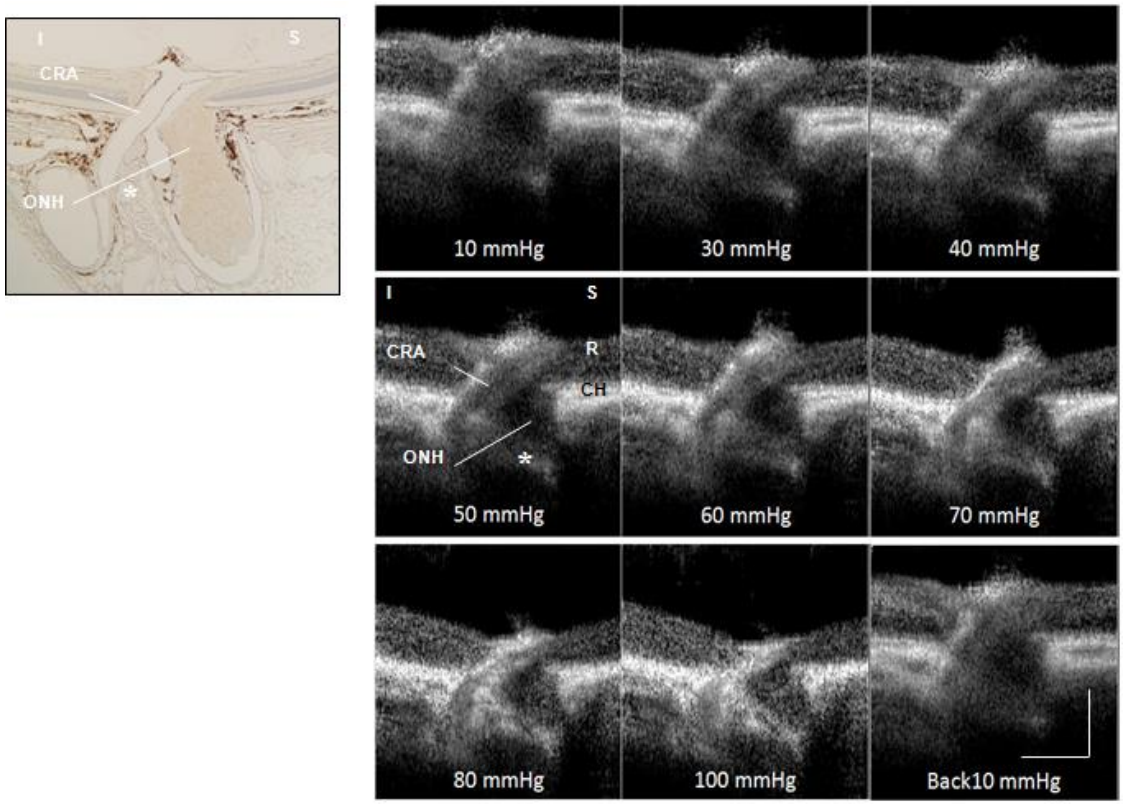

Fig. 3.2 Compared to a histologic section (Left), vertical longitudinal OCT structure image views of the ONH (right) demonstrate that the central retinal artery (CRA) is located inferior to the optic nerve head (ONH), and separated from it by a band of sclera (*). (Right) Sequential images show posterior displacement of the retina (R) and choroid (C) and compression of the CRA with ONH contour change at increasingly higher IOPs. I = inferior; S = superior. White bar = 200 μm.

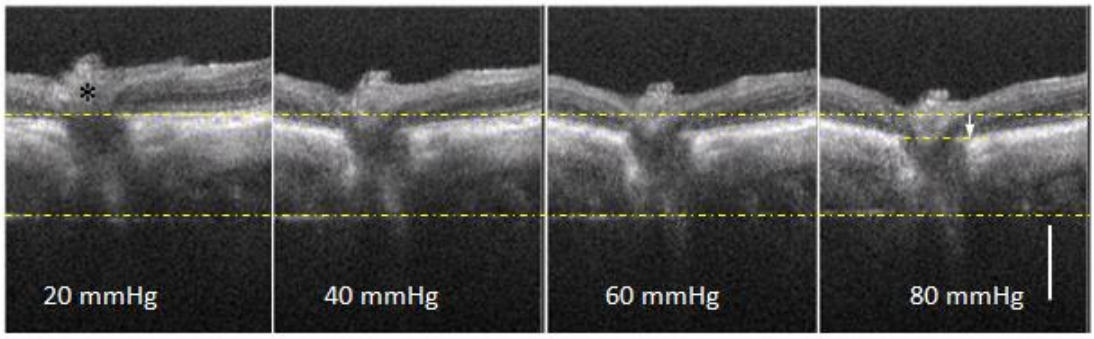

Fig. 3.3 Horizontal views at higher IOPs show posterior bowing of the retina and choroid around the ONH and the posterior displacement of the central retinal vessels (*) into the ONH with the dashed lines as reference. White bar = 200 μm.

3.3.3 Effect of elevated IOP on retinal and choroidal perfusion

UHS-OMAG microangiogram maps (Fig.3.4 A) of the rat RBF showed a progressive decrease in the density of functional capillaries and a decreased diameter of the larger vessels as the IOP was increased from 10 mmHg to 80 mmHg, with near complete obstruction at 100 mmHg. Notably, beginning at 60 mmHg, vertical striping was observed in the UHS-OMAG microangiogram maps, which may be due to increased pulsatility at higher IOPs from reduced ocular perfusion pressure. Apart from visualizing the reduction of RBF, we quantitated the effect of elevated IOP on RBF (Fig.3.4 B). Average blood flow rate changes from 6 eyes (15 vessels) demonstrated an approximately linear decrease in RBF relative to baseline, starting from 30 mmHg to nearly 0 at 100 mmHg. RBF maps and flow values reverted to baseline after IOP was returned to 10 mmHg. The corresponding vessel diameter changes are given in Fig.3.4 C, to help identify the contribution of velocity and vessel diameter to the reduced blood flow rate. This shows that the reduction in vessel diameter was smaller than that of blood flow rate, suggesting that the blood flow rate reduction resulted from decreased flow velocity as well as reduction in vessel diameter. The relatively larger error bars in diameter change are caused by the inherent size difference between veins and arteries and a likely greater effect of increased IOP on the former as opposed to the latter.

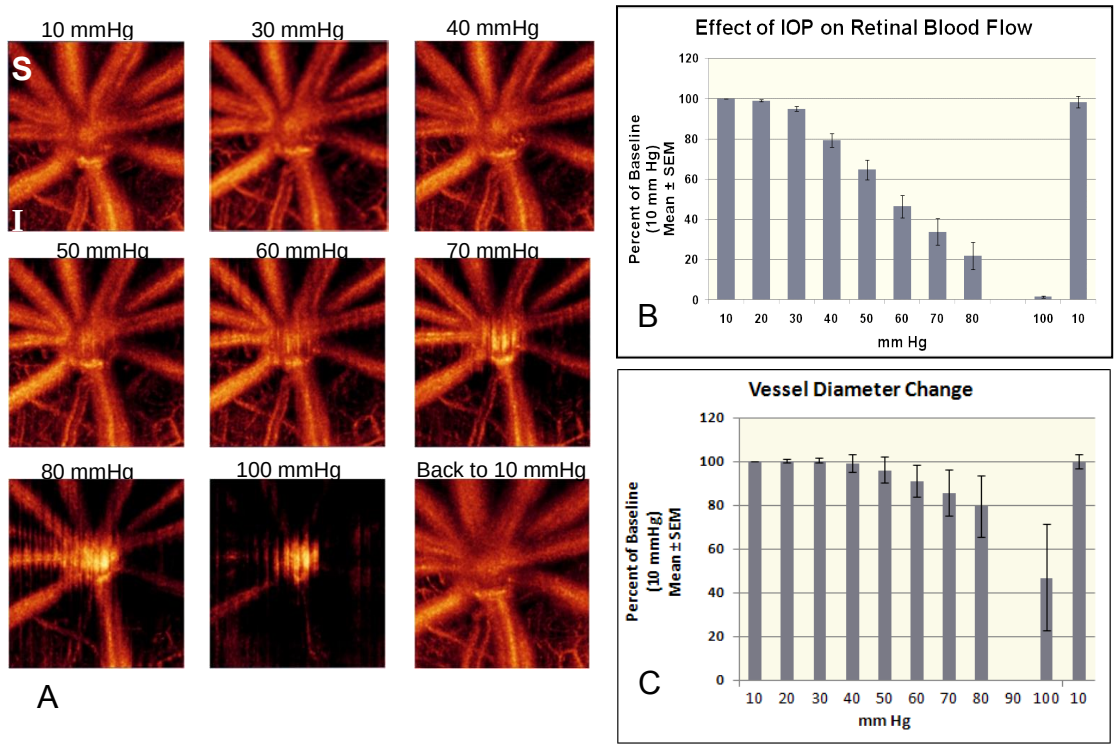

Fig. 3.4 (A) UHS-OMAG microangiogram maps of the rat RBF at different IOPs. Image size: 0.5x0.5 mm^2. (B) Quantitative RBF data (Mean ± SEM) from 6 eyes (15 vessels) show the relative change of RBF under increased IOPs. (C) The corresponding vessel diameter change. The values in B and C are normalized to the percentage of baseline value (10mmHg).

The appearance of choroidal capillary beds (Fig.3.5) at increasing IOP was viewed after removal of the retinal vessels in the post-processing of the 3D OMAG dataset. This revealed, at low IOPs, a dense and intact choroidal capillary bed and choroicapillaris with an opening for the ONH. As the IOP was increased, these beds began to show the effects by 60 mmHg, as demonstrated by apparent filling voids (*). Above this IOP, choroidal capillaries were increasingly dramatically compressed, allowing larger choroidal vessels to be visible. At 100 mmHg, even large choroidal vessels appeared closed. Within the ONH, some capillaries (arrows) were visible up to 70 mmHg, but not above this. As with the RBF, all changes reverted to baseline once IOP was returned to 10 mmHg.

To quantitate the reduced choroidal perfusion or filling with increasing IOP, we measured the area of choroidal filling at each IOP level and calculated this as a percentage of the choroidal

filling seen at baseline (10 mmHg) over the whole image size according to the pixel characteristics for 6 eyes (Fig.3.6). This showed that, from 10 to 50 mmHg, filling was equal to baseline, which we interpret as no reduction of choroidal perfusion. At 60 mmHg, filling was reduced by 6.5% indicating early effects on choroidal perfusion. Above 60 mmHg, this effect increased in a nearly exponential fashion, and at 100 mmHg perfusion was reduced to only 20% of baseline. Again, peripapillary choroidal perfusion returned to normal once IOP was lowered to baseline.

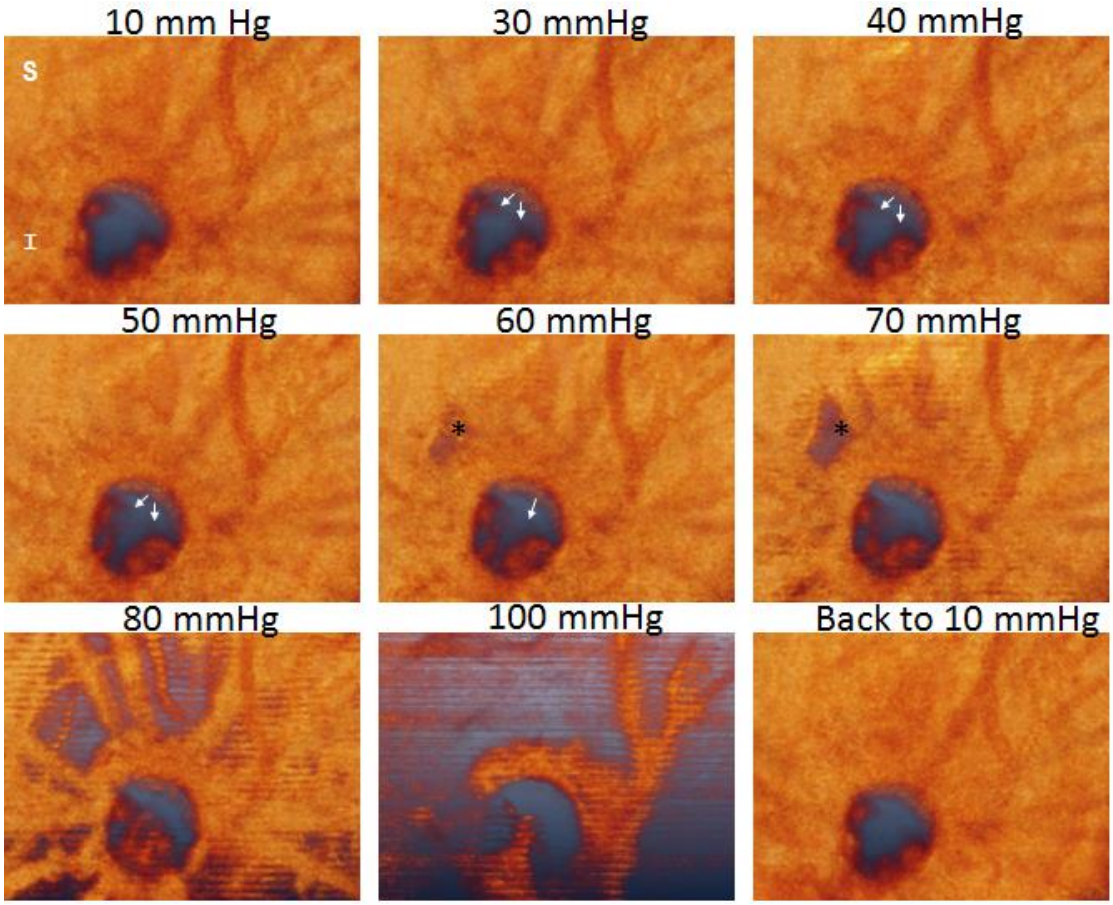

Fig. 3.5 UHS-OMAG microangiogram of choroidal and ONH capillary beds at increasing IOP from 10 mmHg to 100 mmHg and back to 10 mmHg, viewed after removal of the retinal vessels. Arrows indicate ONH capillaries, visible up to 70 mmHg; Asterisk indicate filling void in the choroid.

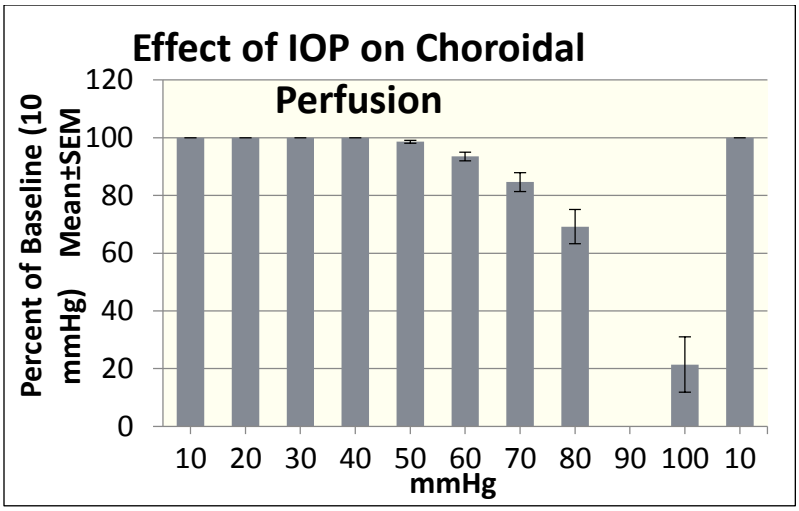

Fig. 3.6 Quantitative measurement of the IOP effect on the choroidal flow illustrated by the percent of perfused choroidal area compared to baseline value at 10 mmHg (Mean ± SEM, n =6).

3.3.4 Effect of elevated IOP on ONH blood perfusion

Fig.3.7 shows the quantitative evaluation of ONH blood perfusion response to increased IOP. Fig.3.7 (top row) showed both cross-sectional structure image (A, C) and corresponding flow image (B, D) across the ONH region. Dense capillary flow signal could be visualized in the Fig.3.7 (D), however, overlying retinal vessels may lay a shadow in the beneath ONH area which cause the low structure signal intensity (dashed circle in Fig.3.7 A) and capillary flow undetectable (Fig.3.7 B). Fig.3.7 (middle) shows the steps in quantitation of ONH blood perfusion. These include segmentation of the retinal vasculature from anterior view 3-D vasculature maps (E to F), and then identifying the blood flow signal pixel map (G) and the ONH volume used for the percentage of flow calculation (H). After we obtained the binary blood flow pixel maps, the whole segmented binary map, which represents ONH volume, was integrated, the value of which was considered to be the percentage of blood flow volume compared to the whole ONH volume. The volume for this data analysis has an approximate depth of 150 μm posterior to the choroidal opening as shown in Fig.3.7 (C). In order to show the effect of acutely increased IOP on the ONH blood flow, we calculated blood flow in this manner at each IOP level.

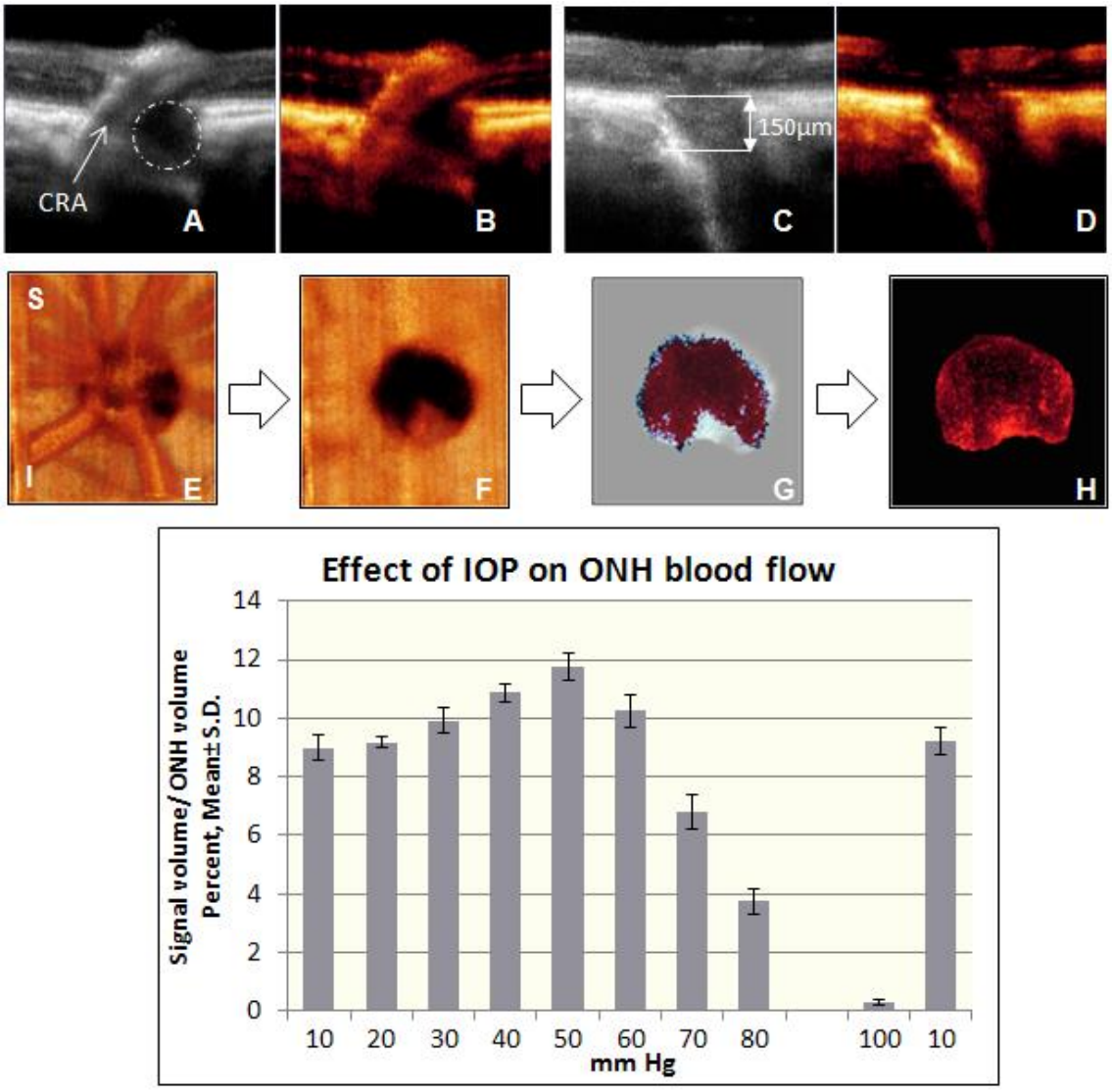

Fig. 3.7 (Top) (A) Cross-section OCT structure image across the CRA, and the dashed circle shows the shadowed region. (B) Corresponding flow image of (A). (C) Cross-section OCT structure shows the dimension (between the two lines) for ONH flow analysis. (D) Corresponding flow image of (C). ((Middle) Steps in quantitation of ONH blood flow, including removal of retinal vasculature from anterior view 3-D vasculature maps (E to F), generating the blood flow signal pixel map (G) and the ONH volume (H). Image size: 0.5x0.5 mm^2. (Bottom) Graph of ONH blood flow (Mean ± SEM, N=6 animals) change with increasing IOPs. Up to 50 mmHg, blood flow appears to increase, possibly as a result of improved signal detection due to a gradual decrease in the shadowing effect as blood flow in overlying retinal vessels is reduced. Above 50 mmHg, reduction in ONH blood flow overcomes this effect and becomes clearly evident, reducing to near 0 at 100 mmHg and returning to baseline when IOP is lowered to 10 mmHg.

A graph of these ONH blood perfusion calculations at increasing IOPs is shown in Fig.3.7 (bottom). This shows an apparent increase in blood perfusion at lower IOPs, in contrast to RBF (Fig.3.4), which decreased. We feel that this is most likely due to the reduced detection of ONH capillary signal by "shadowing and tailing" from overlying retinal vessels at the low IOPs. As blood flow in the retinal vessels is decreased with higher IOPs, this effect is reduced and the signal improves, until it is diminished by actual reduction in ONH blood perfusion. Above 60 mmHg, this produces a clear reduction that progresses to nearly 0 at 100 mmHg. Again, ONH perfusion reverted to baseline when IOP returned to 10 mmHg.

3.4 Discussion

Elevation of IOP is well known to affect retinal perfusion [83], and many investigators maintain that altered blood flow to the ONH may play a role in the development of optic nerve damage in some glaucoma patients, particularly those lacking clear evidence of elevated IOP [84]. In addition, nearly all animal models developed to study the mechanisms of glaucomatous optic nerve damage involve elevation of IOP [76]. However, unless perfusion of the back of the eye can be determined in these models, it is difficult to be certain what role reduced perfusion or ischemia might play in the effects of elevated IOP on the relevant tissues. For these reasons, developing non-invasive methods of imaging and measuring blood flow in the retina, choroid and ONH is important for both clinical management and experimental research in glaucoma.

OCT/OMAG has now been successfully used to image in vivo microvascular beds, to the capillary level, in several different tissues, including human skin and retinal and choroidal vessels, and in several experimental situations, such as the response of brain and rat skeletal muscle vascular beds to physiologic stimuli [85, 86]. Most recently, we have described its adaptation for imaging and measuring blood flow in the retinal vasculature of the rat eye. In this report, we expand on these observations of the peripapillary retina and extend them to the ONH and adjacent choroid. With this, we are provided insights into the unique anatomy of the microvasculature of these structures in the rat eye and demonstrate that this method may be a useful tool to supply

quantitative assessment of the response of blood flow to acute elevations in IOP in these different regions.

A significant feature of this system is the use of 1300 nm wavelength light, which allows deeper penetration of ocular tissues than instruments using 800 nm light. The advantage of this degree of penetration is evident from the detailed tissue images of the ONH that even include posterior ciliary vessels, many features of which can be directly correlated with those of a histologic tissue section, as shown in Fig.3.2. Of particular importance, 3D maximal projection maps of the peripapillary retina, choroid and ONH (Fig.3.1) even include the ONH capillary bed to a depth of 150 μm, a region that is thought to be the site of initial axonal injury in our chronic rat glaucoma model [78, 87]. Another advantage of the increased penetration of this system is that it allows us to visualize conformational tissue responses to elevated IOP within the ONH (Fig.3.2 and Fig.3.3). Fortune and colleagues, using spectral domain OCT with the Spectralis HRA-OCT (Heidelberg Engineering GmbH, Heidelberg, Germany) have recently reported detailed measurements of rat retinal and ONH response to acute IOP elevations of 50 and 70 mmHg [88]. They noted the elliptical choroidal opening that bordered the ONH, and found significant posterior movement of the ONH surface and decreased retinal thickness within this ellipse during elevated IOP. Fig.3.2 of the current study qualitatively shows posterior movement of the ONH surface at higher IOP, but also demonstrates posterior movement and compression of the central retinal artery, as well as apparent density of the optic nerve itself within the ONH. Quantification of these internal ONH changes is beyond the scope of the current report, but these images suggest the possibility of using this technique to monitor and better understand the physical consequences of cellular responses to elevated IOP, particularly at the site of initial injury, that we have observed in our chronic model of elevated IOP [19, 78]. The microvasculature images provide striking *in vivo* corroboration of prior findings of basic anatomic features of the ONH in the rat that, until now, were only apparent using static *ex vivo*, histologic methods [89-91]. These

features include a consistent presence of the central retinal artery inferior to the horizontally-oriented kidney bean-shaped neural optic nerve at the level of the sclera.

In addition to these anatomic relationships, OMAG/OCT also provides a dynamic view of the ocular vasculature, as shown by our ability to measure microvascular responses to acutely elevated IOP in all three tissue beds. While relatively few studies have been published on the rat microvascular response to elevated IOP, our results (Fig.3.4) are in general agreement with those of He and colleagues [62] who, using the laser Doppler flowmetry, noted that an IOP of 50 mmHg was associated with a reduction in ocular blood flow to approximately 50% of baseline, as compared to our finding that a similar IOP level produced a less severe reduction in flow, to just over 60% of baseline. At higher IOP, we observed vertical striping of the vessels in the UHS-OMAG microangiogram maps, which we interpreted as increased pulsatility of the vasculature as perfusion pressure nears diastolic pressure. Because ocular perfusion is dependent on systemic blood pressure, we measured the effect of 2% isoflurane via the femoral artery in a separate group of similar-aged rats, revealing a mean systemic blood pressure ($\pm$ SEM) of 106 $\pm$ 4 mmHg (N = 5). This is comparable to published experience with isoflurane as well as other anesthetics [62, 92-95] and is consistent with the increased pulsatility observed by OMAG/OCT. Similarly, Fortune and colleagues noted significant attenuation of the retinal vessels when IOP was raised to 70 mmHg [88].

Interestingly, Bui and colleagues [62, 96] observed an almost immediate reduction in blood flow with elevated IOP, while, with OMAG/OCT, we found that, while RBF did show an initial decrease below 30 mmHg, this accelerated to a linear reduction above 30 mmHg. This may suggest evidence of autoregulatory mechanisms that may be overcome once perfusion pressure is reduced to a critical level. This phenomenon, which appears to be operative up to an IOP of 30 to 40 mmHg, has been extensively studied in the retina and ONH in humans [57, 97, 98] and in non-human primates [83] as well as other research animals [99, 100]. Images of the choroidal microvasculature are dominated by the capillary beds of the choroid and choriocapillaris that are

too small and dense to discriminate, which results in a generalized, uniform signal. Because of this, blood flow velocity in individual vessels cannot be determined, as done for the retinal vasculature. However, we were able to quantitate percent choroidal filling by measuring areas of non-perfusion at increasingly higher IOPs. Using this, we noted that choroidal "perfusion" remained stable over a surprisingly wide range of IOPs, and only began to deteriorate noticeably at 60 mmHg, with a rapid drop above this level (Fig.3.6). While choroidal perfusion has classically been considered to be influenced solely by ocular perfusion pressure [101], other work in animals and humans suggests that choroidal autoregulation may occur [102, 103]. While it is tempting to interpret our current data as further evidence of choroidal autoregulation, this is only a measure of choroidal filling, and not strictly a measure of choroidal flow, as the flow rate within the capillary beds still being perfused is unknown. Further refinements, perhaps using measures of pixel density within these beds may improve our ability to use OMAG/OCT for a more accurate assessment of choroidal perfusion.

Perhaps of greatest significance to use of the rat eye to assess mechanisms of glaucomatous injury is the potential of OMAG/OCT to measure ONH blood flow. While this did reveal a reversible reduction in perfusion at higher IOPs, we encountered a tailing and shadowing effect caused by overlying major retinal vessels. As mentioned above, this will affect the observed blood flow signal within the ONH, especially when the large retinal vessels are fully perfused at lower IOP levels. This likely result in a false increase in measured blood flow within the ONH as the IOP increases from 10 mmHg to 50 mmHg, and retinal flow is reduced. In order to solve this problem, one possible approach could be to use measured RBF change to compensate for the impact of this tailing effect on measured ONH blood flow. The Study of the relationship between measured ONH flow and the overlying RBF is currently ongoing.

3.5 Conclusions and future work

In conclusion, we have used an OCT/OMAG system to image the posterior eye of the rat. Using a wavelength of 1300 nm for increased penetration, we were able to image the structural and

vascular anatomy of nearly the entire thickness of the ONH, and the adjacent choroid and retina, and demonstrate the effects of acutely elevated IOP on these structures. Quantitative measurements of the effect of elevated IOP on the RBF, and choroidal and ONH perfusion as determined by this technique are presented as well. Starting from 30 mm Hg, the RBF diminished linearly with increasing IOP and was nearly extinguished at 100 mm Hg. Choroidal perfusion did not appear to be affected until 60 mmHg, above which further reductions developed exponentially. Both of these effects fully recovered after IOP was returned to baseline. A reduction in ONH capillary blood flow at higher IOP's was also observed, but tailing and shadowing from perfusion of overlying retinal vessels at lower IOP's limited precise measurements of change compared to baseline ONH flow. This technique may prove useful in evaluating the contribution of altered retinal, choroidal and ONH perfusion to optic nerve and retinal damage in rodent glaucoma models that employ elevated IOP.

In the future, we will improve the system resolution and performance to better visualize the capillary network change during the IOP elevation by switching back to 800nm central wavelength light source (chapter 7). We will also continue to investigate the effects of long term elevated IOP (4hours) on the structures and blood perfusion within retina, choroid and ONH.

Chapter 4. Evaluation of the effect of elevated IOP on retinal capillary bed and total retinal blood flow in rats using optical coherence tomography

The objective of this chapter is to evaluate the effect of acutely elevated intraocular pressure (IOP) on the retinal capillary bed and total retinal blood flow (RBF) in anesthetized rats using Optical microangiography (OMAG)/Optical coherence tomography.

4.1 Introduction

Glaucoma is one of the leading causes of blindness. Although many glaucoma risk factors have been identified, elevated intraocular pressure (IOP) is the best defined and controlling IOP is the mainstay of glaucoma therapy. Currently, many studies have been conducted to evaluate the effect of the increased IOP on the retinal structure and function. The capability to visualize detailed capillary network and quantify the total retinal blood flow would be a big advance for better evaluation of the effect of elevated IOP on the retina and ONH function.

In chapter 2 and 3, we have evaluated the effect of elevated IOP on structure and blood flow of retina, choroid and optic nerve head (ONH) in rats. In order to increase the penetration of light into ONH and get a maximized intensity, we utilized a SLD light source centered at 1300 nm. However, this impairs the system resolution, which limits the system capability for resolving detailed capillary network of retina. In order to improve the system resolution, we need to switch the central wavelength of light source back from 1300 nm to 800 nm. This improved resolution will enable better visualization of the retinal capillary bed response to the elevated IOP.

One big issue with the previous work is that the lack of information about systematic blood pressure during the process of IOP elevation. In this chapter, we will improve the system setup which enables us to monitor the systematic blood pressure during the whole process of IOP

elevation. With the systematic blood pressure information, we will be able to look at the effect of perfusion pressure, instead of IOP only on the functionality of retina.

Another issue with the previous work is that the increased IOP effect on retinal blood flow is only evaluated on a couple of retinal arteries and veins, but not the total retinal blood flow. In order to calculate the blood flow rate, we need calculate the Doppler angle of each vessel, which can cause errors to the blood flow calculation. In this chapter, we will utilize an *en face* Doppler OCT approach to measure the total retinal blood flow (RBF) in rats. The flow can be calculated by integrating the axial blood flow velocity over the vessel area measured in an *en face* plane without knowing the blood vessel angle. The effect of acutely elevated IOP on total RBF can be evaluated noninvasively with this approach.

4.2 Materials and Experimental methods

4.2.1 System setup and methodology

Fig. 1 shows the schematics of the system setup utilizing high-speed spectral domain OCT system for *in vivo* imaging of a rat eye under elevated IOP. We employed a home-built spectral-domain OCT system. Briefly, the system was operated at a central wavelength of 840 nm with a spectral bandwidth of 42 nm, providing an axial resolution approximately 7.2 μm in air. The homebuilt spectrometer encloses a high speed CMOS line scan camera (Basler Sprint spL4096-140 km), having 10 μm square pixels in two rows and 4096 pixels wide. In order to increase the camera speed, only 896 pixels were illuminated and the camera was read at an exposure time of 4.2 μs which provided an ultra-fast line scan rate of 240 kHz. In the sample arm, we applied an objective lens (75 mm focal length) and ocular lens (Ocular Instrument, Maxlight Standard 90D) combo that enables a large field of view and a lateral resolution (~10 μm, simulated results with Zemax) of the rat retina.

The rats were anesthetized with inhalational isoflurane (2.0 %) mixed with 80% air and 20% oxygen, and positioned in custom-made holding stage with multi-dimension adjustability. Under

isoflurane anesthesia, the tail artery was cannulated and connected to a pressure transducer to monitor systemic blood pressure during the whole experiment. During the whole experiment, body temperature was kept at 37 ℃ by a homeothermic blanket control unit.

IOP was elevated unilaterally by cannulation of the anterior chamber with a 5 millimeter long 31 gauge needle connected to a reservoir filled with balanced salt solution and to a calibrated pressure transducer. Topical anesthetic (0.5% proparacaine hydrochloride, Alcon Laboratories Inc.) was instilled prior to cannulation. The height of the reservoir was used to elevate IOP, as determined by the transducer, in 10 mm Hg increments, from 10 mm Hg (treated as baseline) to 80 mmHg followed by a pressure of 100 mmHg which produced complete obstruction of ocular blood flow. After that, IOP was reduced back to 10 mmHg to examine reperfusion. As a secondary confirmation, IOP was monitored indirectly during cannulation with a rodent tonometer (Tonolab, iCare, Finland). The laboratory animal protocol was approved by the Animal Care and Use Committee of University of Washington.

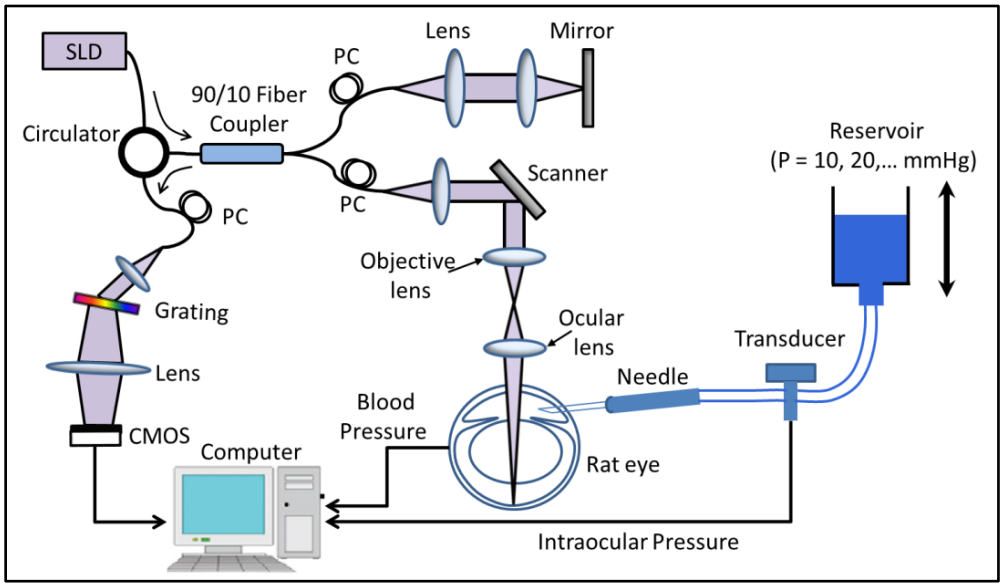

Fig. 4.1 Schematic of the setup utilizing high-speed spectral domain OCT system for in vivo imaging of a rat eye under controlled intraocular pressure. SLD: superluminescent diode; PC: polarization controller; CMOS: line scan camera.

4.2.2 Data acquisition and post-processing

The right eye was carefully placed under the sample arm for OCT imaging. Before OCT imaging, the pupil was dilated with the eyedrops (10% phenylephrine hydrochloride ophthalmic solution, USP, AK-Dilate™) to allow OCT beam access to the posterior segment and saline solution was added to the cornea to keep the eye hydrated.

At each IOP level, a 3D data volumes covering the optic nerve head (ONH) area with a size of ~ 2x2 mm^2 was first captured using the UHS-OMAG step scanning protocol, in which the raster scanning of the beam spot was performed to capture 512 A-lines within each B-frame (2D cross-sectional image) and 2000 B-frames for each C-scan (3D image). These 2000 B-frames were captured at 400 cross-sections with 5 repeated B-frames captured at each cross-section position. Using a frame rate of 360 frames per second (fps), the whole 3D data volume could be captured within 5.5 seconds. We then captured another 3D dataset covering a region of ~ 1x1 mm^2 around ONH using conventional OMAG scanning protocol with dense A-scan (2000 A-lines per B-frame) for phase-resolved Doppler OCT analysis to determine the axial blood flow velocity. The camera acquisition rate was reduced to 140,000 A-scans per second and a slow scan duty cycle 80% which resulted in a frame rate of 56 fps. The system has a real time preview system to make sure the ONH was placed in the center of the 3D image.

After all the data were captured, the 3D UHS-OMAG data were post-processed using the UHS-OMAG algorithm, i.e. high pass filtering along the C-scan direction to extract the blood flow signal out of the background tissue. At each cross-section, the phase-compensated complex signal of adjacent B-frames were subtracted consequently and then averaged (four times) to obtain the cross-sectional blood flow image. This was applied to all of the 400 cross-sections to generate concurrent 3D structural and blood flow movies.

4.2.3 Image segmentation and capillary density

The rodent retina consists of three layers of vascular networks [104]: retinal artery and vein along with the radial peripapillary capillaries within nerve fiber layer (NFL) and ganglion cell layer

(GCL), capillary networks within inner plexiform layer (IPL), and capillary networks within outer plexiform layer (OPL). To better show the retinal vessel distribution and quantify the microvascular response to elevated IOP, we need to segment out and render the microvascular maps in different layers. A semi-automated retinal layer segmentation algorithm developed by our research group was used to segment individual retinal layers from the OCT cross-sectional structural images using a two double line model. The segmentation was first applied on structural images and then directly transferred to blood flow images.

To better quantify the capillary response to the elevated IOP, the capillary density of the outer plexiform layer (OPL) was calculated as the pixel number occupied by capillaries over the total pixel number on the binarized image. The capillary density changing curve versus IOP and perfusion pressure was then obtained, as normalized to baseline (10 mmHg).

4.2.4. Measurement of total retinal blood flow rate

Total retinal blood flow measurement was performed using an *en face* Doppler method demonstrated by Srinivasan et al [47]. Unlike conventional Doppler OCT methods, knowledge of the blood vessel Doppler angle is not required. This method was later applied for measuring total flow in the human retina [105] and further developed to evaluate the pulsatile total blood flow in the human and rat retinas [106].

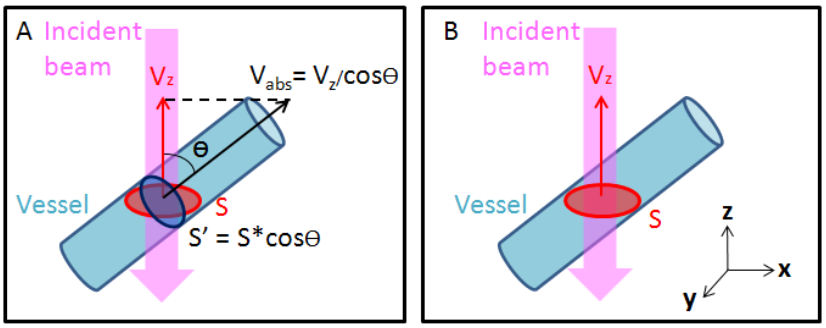

Fig. 4.2 Schematic of *en face* Doppler approach for flow measurement. (A) In conventional Doppler OCT methods, the blood vessel angle Θ is required to compute absolute velocity values V_{abs}. Total blood flow is calculated by multiplying with V_{abs} the cross-sectional area of the vessel S'. (B) In *En face* Doppler method, total blood flow is computed by simply integrating the axial velocity components V_z over the *en face* cross-section S that intercepts the vessel.

In conventional Doppler OCT methods (Fig. 4.2A), the axial velocity component of the blood vessel was first measured using phase resolved analysis. Absolute blood flow velocity was calculated form the axial component corrected by the blood vessel Doppler angle Θ. The area of the vessel in the *en face* (xy) plane is inversely proportional to *cos (Θ)*, whereas the axial velocity V_z is proportional to *cos (Θ)*. Therefore, these two effects cancel when the integration is performed in the *en face* plane, which means blood flow in a vessel can also be calculated by simply integrating the axial velocity components in an OCT *en face* plane that intercepts the vessel (Fig. 4.2B).

Measurement of axial flow velocity within a three-dimensional volume is required before the total retinal blood flow could be calculated. A three-dimensional data set was acquired consisting of 200 images with 1024 axial scans per image over an 800 μm square area in approximately 2 seconds. The axial flow velocity can be derived from phase differences between adjacent A-scans introduced by the motion of blood cells using PRDOCT. The relationship between them is:

$$V_Z = \frac{\Delta\varphi \cdot \lambda_0}{4\pi n \Delta t_A} \tag{1}$$

where $\Delta\varphi$ is the phase difference between adjacent A-scans; λ_0 is the central wavelength of the light source; n is the refractive index of tissue (~1.35); Δt_A is the time interval between adjacent A-scans as mentioned above.

Phase wrapping happens if $|\Delta\varphi| \geq \pi$, hence, the maximal axial velocity component which can be unambiguously measured with a given time interval Δt_A would be:

$$V_{Z\max} = \pm\frac{\lambda_0}{4n\Delta t_A} \tag{2}$$

With an acquisition rate of 140,000 A-scans per second which means Δt_A equals 7.1μs, the maximum axial velocity range that could be measured without phase wrapping was ±20.6 mm/s in tissue. Phase wrapping happened in the blood flow velocity measurement for some of the big

retinal arteries, which means phase unwrapping is required in order to obtain the true total retinal blood flow rate. The phase unwrapping method we used here has been discussed in detail in [51].

After above processing, a three-dimensional map of the axial velocity component $V_z(x,y,z)$ was obtained, from which an *en face* plane bisecting all the retinal arteries and veins could be chosen. We can compute the absolute flow values by integrating the axial flow components over the vessel cross-section in the *en face* plane using the following equation:

$$F = \iint_{xy-plane} V_Z(x,y)dxdy \tag{3}$$

where $V_z(x,y)$ is the axial flow velocity measured for different pixels and $d_x d_y$ represents the actual size of one pixel in the *en face* plane.

4. 3 Results and Discussion

4.3.1 OMAG/OCT provides unprecedented details of retina in rat

The OCT system we developed here provides high resolution cross-sectional imaging of retina in rat as shown in Fig. 4.3A. From the image, we were able to recognize all the retinal layers as well as the choroid layer. 3D rendering of the imaged retina (Fig. 4.3B) and OCT fundus image (Fig. 4.3C) were obtained using Amira 3D software (Visage Imaging, Inc.). From the OCT fundus image (similar to fundus image captured by 2D cameras), we can only some limited information of the, including the optic nerve head, and some large retinal vessels. To better show the details of retina within different depths, we segmented out different retinal layers. The first layer we want to show is the nerve fiber layer (Fig. 4.3 D), within which lots of optic nerve fiber bundles could be visualized clearly. UHS-OMAG can provide unprecedented details of retinal microvasculature of retina and choroid in rodents. Microvascular maps in three different retinal layers as well as choroidal layer were obtained as shown in Fig. 4.3 (E-H), from which different vascular patterns could be observed. NFL/GCL consist the retinal artery and vein along with the radial peripapillary capillaries, IPL consist intermediate capillary networks and OPL consist capillary networks and post-capillary venules. The retinal arteries and veins within the NFL and GCL (Fig.

4.3 E) are arranged alternately and radiate in spoke-like fashion towards the retinal periphery. Dense capillary networks were well distributed and observed in IPL (Fig. 4.3 F) and OPL Fig. 4.3 H), which are supposed to supply the nutrients for the ganglion cells and nuclear cells. The choroidal vasculature (Fig. 4.3 G) was obtained as well. It was consisted mainly by large vessels although small blood vessels were also observed around the ONH area.

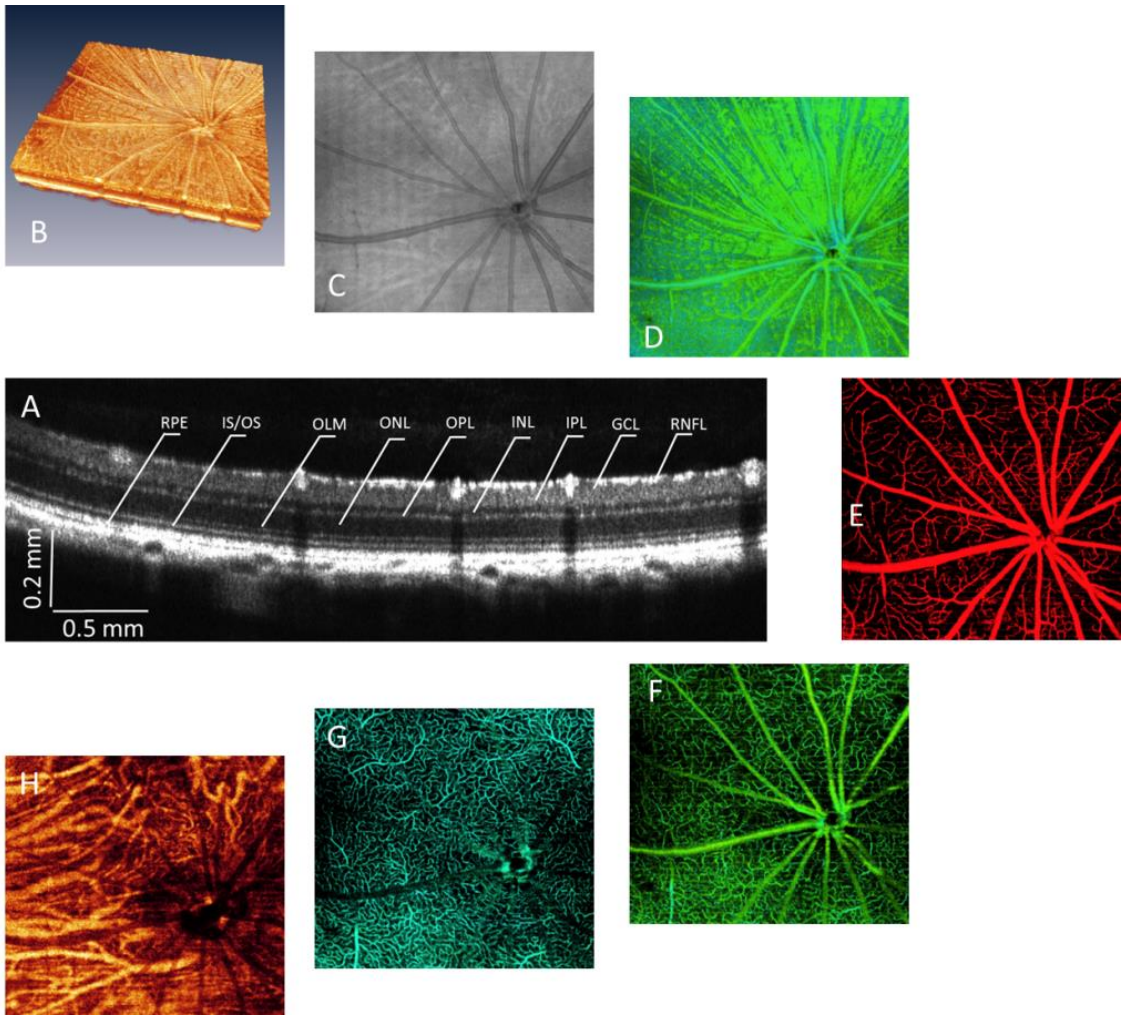

Fig. 4.3 OMAG/OCT provides unprecedented details of retina in rat. (A) Cross-sectional OCT structure image, all the retinal layers could be resolved. (B) 3D volume rendering of the retina structure. (C) OCT fundus image. (D) Projection view of nerve fiber layer (NFL), from which lots of nerve fiber bundles can be visualized. (E) Microvessel/capillary within NFL/GCL, capillary network within IPL (F) and OPL (G). (H) Choroidal vasculature.

4.3.2 OCT reveals the effect of elevated IOP on retinal microstructure

The system blood pressure was monitored and turns to be stable during the IOP elevation process (Fig. 4.4 A). The average systematic blood pressure with the current experiment setup is ~80 ± 6 mmHg, which is relatively lower than normal condition. We will discuss in more detail about this in the following parts.

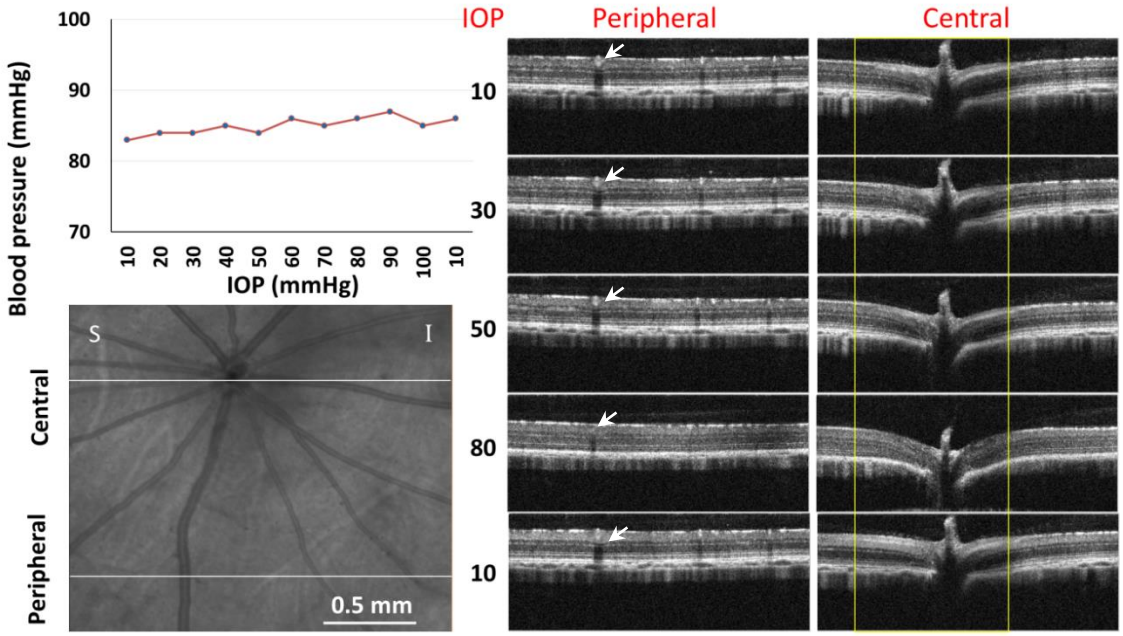

Fig. 4.4 OCT reveals the effect of elevated IOP on retinal microstructure. (Left) Blood pressure was measured to be stable during the IOP elevation (up). OCT fundus image indicating measurement lines (bottom). (Right) The retinal structure response reveals deformation of ONH with elevated IOP (yellow square region).

OMAG/OCT provides the capability of both structural imaging and blood flow imaging. The effect of acutely elevated IOP on retinal microstructure could be documented from OCT structural images. Fig. 4.4 B shows an *en face* view of the scanned retinal volume, from which two cross-sections which represents central and peripheral retina were monitored (Fig. 4.4 C). The retinal layers were compressed due to the increased IOP, especially for the blood vessel as pointed by the arrow. The OCT microstructural images at the central retina reveal obvious deformation of ONH with elevated IOP and this recovers back to normal state when IOP return

back to baseline. B. Fortune et. al. [88] also observed the rapid, reversible posterior deformation of the rodent optic nerve head and peripapillary structures during acute intraocular pressure elevation which is consistent with our founding.

4.3.3 UHS-OMAG visualizes the detailed effect of elevated IOP on retinal capillary bed and Choroid

UHS-OMAG provides the capability to visualize detailed microvasculature within different retinal layers and choroidal layer. In order to better show the effect of elevated IOP on retinal capillary bed, we segmented out the microvasculature within the three different layers as described above. The effect of elevated IOP on superficial micro-vessels and the radial peripapillary capillaries within NFL/GCL (Fig. 4.5), capillary networks within IPL (Fig. 4.6), and capillary networks within OPL (Fig. 4.7) could be visualized clearly. We can't visualize obvious changes from the images until up to 50 mmHg (in this case, BP is ~ 80 mmHg), and then the flow and capillary vanish abruptly. Especially for inner plexiform (Fig. 4.6) and outer plexiform layer (Fig. 4.7), no capillary vessel could be visualized at IOP equals 70 and 80 mmHg. For the superficial layer, the large arteries and veins can stay up to 70 mmHg IOP, but with obvious compressed vessel diameter.

Besides the retinal layers, we could also visualize the response of choroidal vasculature to elevated IOP (Fig. 4.8). There is a slightly different for the choroidal vasculature change. The vascular intensity increases for IOP from 10mmHg to 50 mmHg and then start to decrease from 60 mmHg. The reason for the increasing signal would be due to decreasing absorption from the above retinal layers when IOP is lower than 50 mmHg. The flow in choroid also disappeared when the IOP is 80 mmHg which means that absolute occultation of ocular flow happens when the perfusion pressure (systematic blood pressure – intraocular pressure) is ~ zero. All these effects were recovered when the IOP return back to the baseline at 10 mmHg.

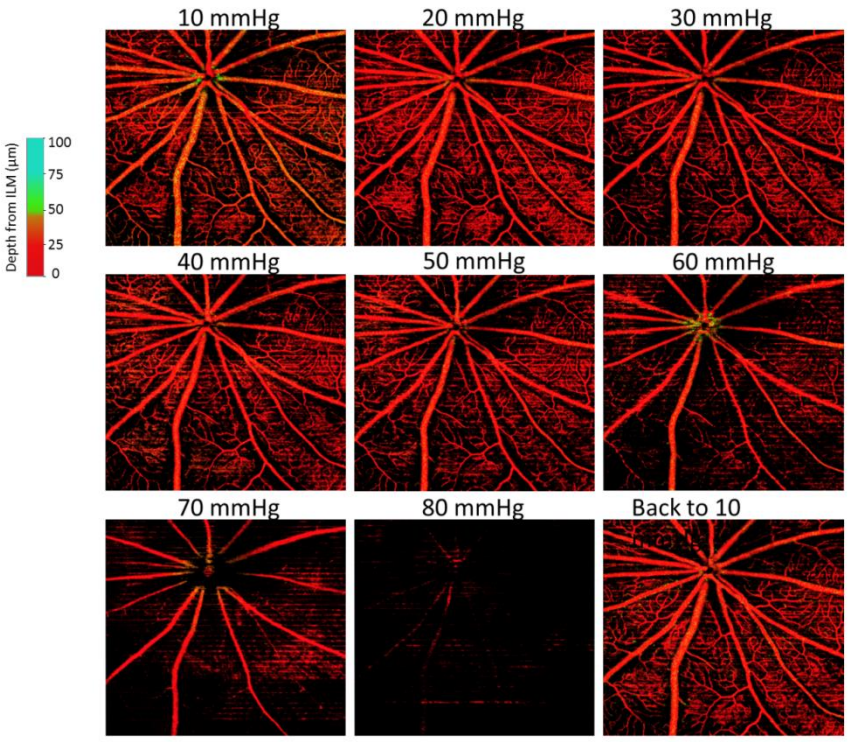

Fig. 4.5 Response of micro-vessel/capillary within NFL/GCL to elevated IOP.

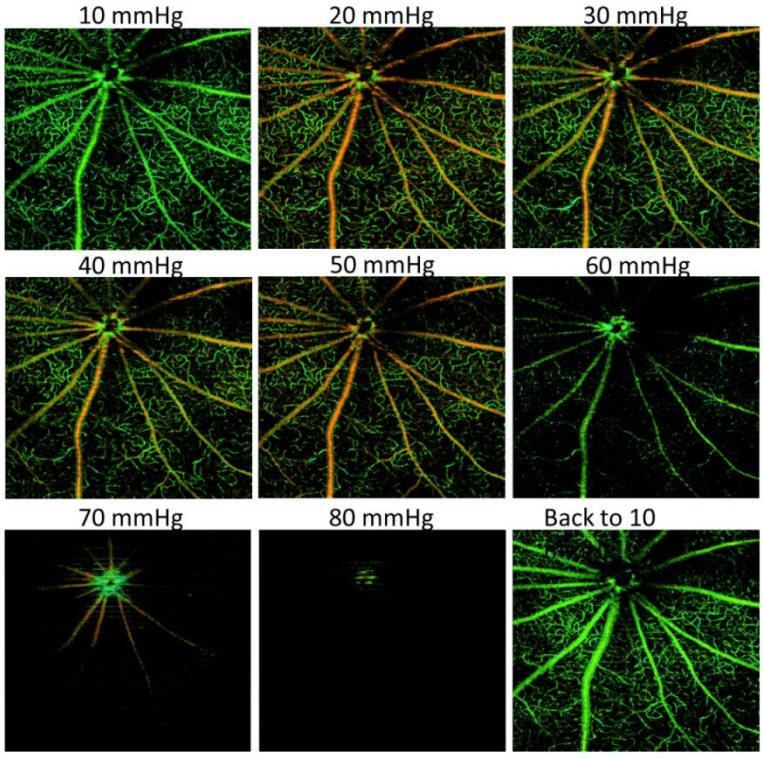

Fig. 4.6 The response of capillary within IPL to elevated IOP.

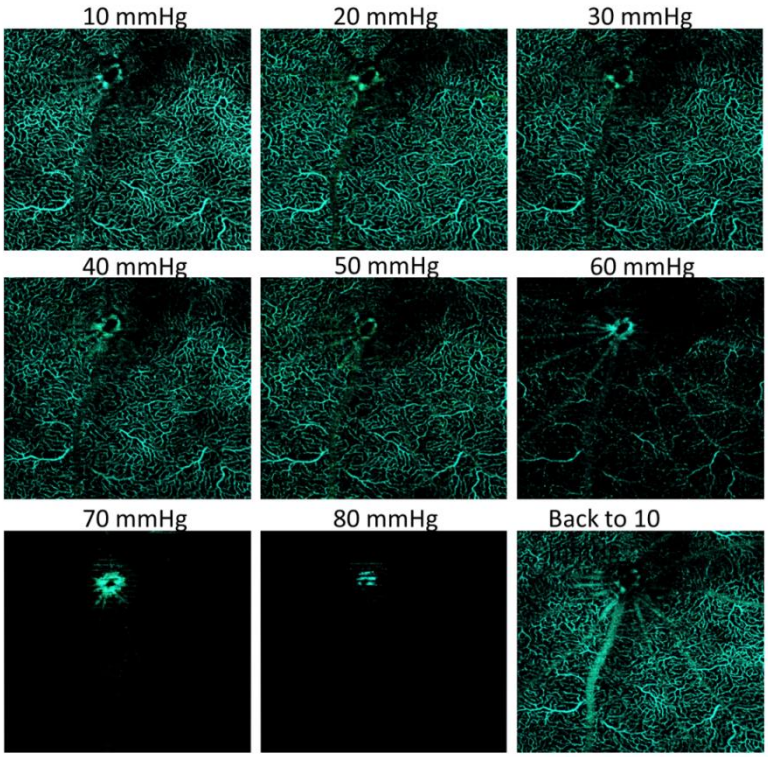

Fig. 4.7 Response of capillaries within OPL to elevated IOP.

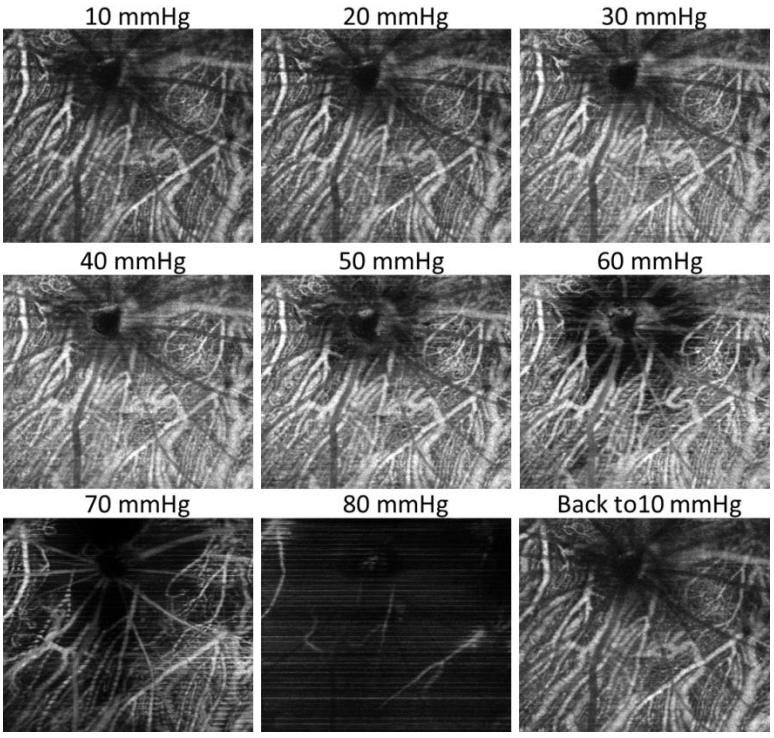

Fig. 4.8 Response of vasculature within choroid layer to elevated IOP.

4.3.4 Elevated IOP effect on retinal capillary density (OPL) quantified by UHS-OMAG

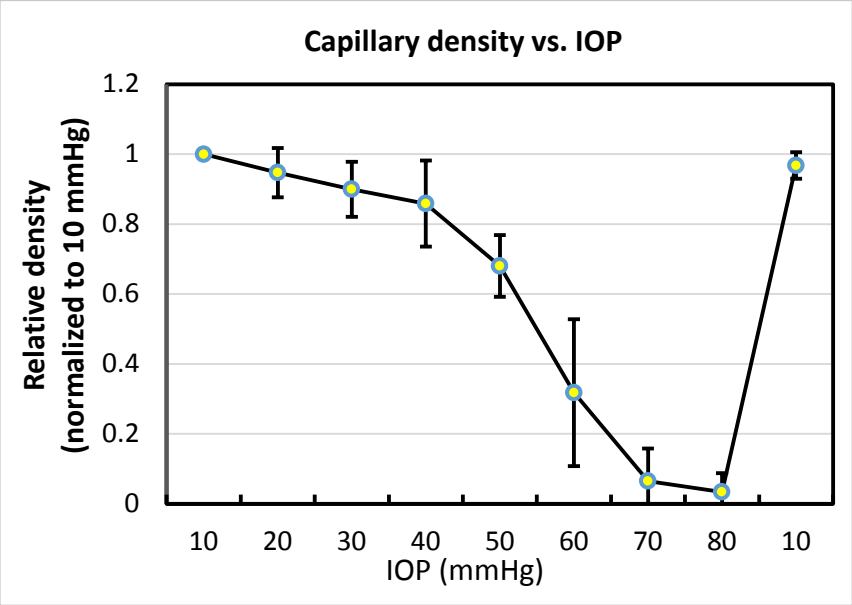

Fig. 4.9 The OPL capillary density change as the IOP increases, but was not significantly affected until IOP exceeds 40 mmHg.

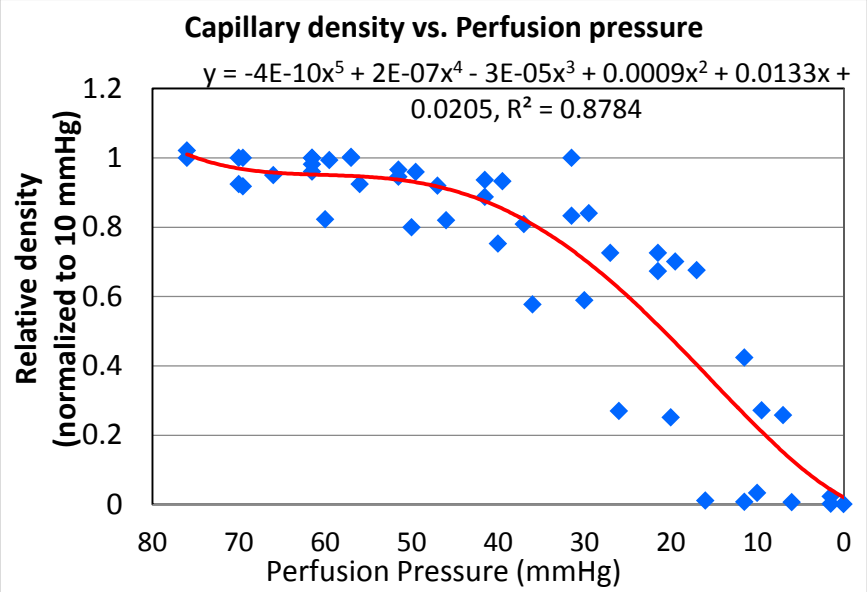

Fig. 4.10 Taking systematic blood pressure into consideration, the capillary density change was plotted versus perfusion pressure decrease, indicating that capillary density does not significantly decrease until perfusion pressure falls below 40 mmHg.

In order to better evaluate the effects of elevated IOP on retinal capillary bed filling, the capillary density of the outer plexiform layer (OPL) was quantified based on the UHS-OMAG images. The dynamic changing curve of OPL capillary density vs. IOP was shown in Fig. 4.9. We can find that the OPL capillary density was not significantly affected until IOP exceeds 40 mmHg, while after IOP exceeds 40 mmHg, sharp decrease happens, which confirms what we have visualized from the images.

Since systematic blood pressure variation exists for different animals, we need to take the systematic blood pressure into consideration. The scatter plot of OPL capillary density versus perfusion pressure (systematic blood pressure – intraocular pressure) was shown in Fig. 4.10. A fifth order polynomial fitting was applied to fit the data which gives the curve that related the OPL capillary density with perfusion pressure mathematically ($R^2 = 0.878$). Also, there is less than 15% decrease in the OPL capillary density when the perfusion pressure was higher than 40 mmHg. This may indicate autoregulation exists for the capillary bed. Alternatively, this can be because the UHS-OMAG based capillary density measurement cannot adequately reveal the change of capillary flow since that it has very high sensitive to slow flow. UHS-OMAG flow image is actually an "on and off" imaging tool which means any motion within the capillary will results in signal in flow image while only when the red blood cell stops flowing, it will not show up.

4.3.5 Elevated IOP effect on total retinal blood flow quantified by *en face* Doppler OCT

The total retinal blood flow response to the elevated IOP was quantified by the *en face* Doppler OCT (Fig. 4.11). An *en face* image (Fig. 4.11B) at a particular depth that intersects all the retinal arteries and veins was obtained from the 3D Doppler OCT data. The total arterial flow and venous flow could be calculated by integrating the axial velocity over the vessel area, respectively. The total retinal blood flow was measured as the average of arterial and venous flow. In contrast to the capillary vessel response, the total retinal blood flow decreased almost nearly as to the increased IOP (Fig. 4.11C).

Similarly, we plotted the total retinal blood flow vs. perfusion pressure scatterly, and then fit it to a linear line (R^2 = 0.907). Total RBF decrease linearly with reduced perfusion pressure (when perfusion pressure < =70 mmHg). But one thing we need to point out is that, all the results above are from relatively low mean systematic blood pressure (~ 80 ± 6 mmHg) and more results with BP ~ 98 ± 5 mmHg are still under analysis. The relative low BP can be a potential issue why the total blood flow didn't show autoregulation.

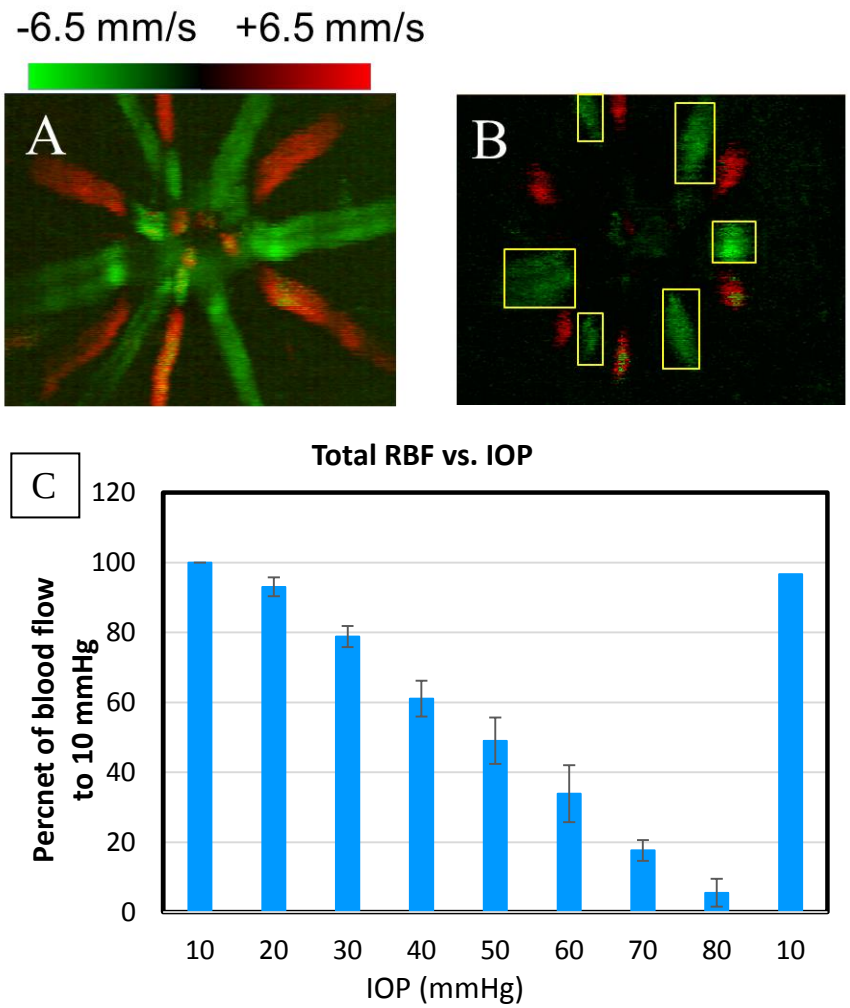

Fig.4.11 (A) Maximum projection and (B) *En face* view of bi-directional axial flow velocity. Yellow squares indicate integration of venous flow, and similar integration could be done on the arterial flow. Total RBF is calculated as the average of arterial and venous flow. (C) The total RBF decrease almost linearly to increased IOP.

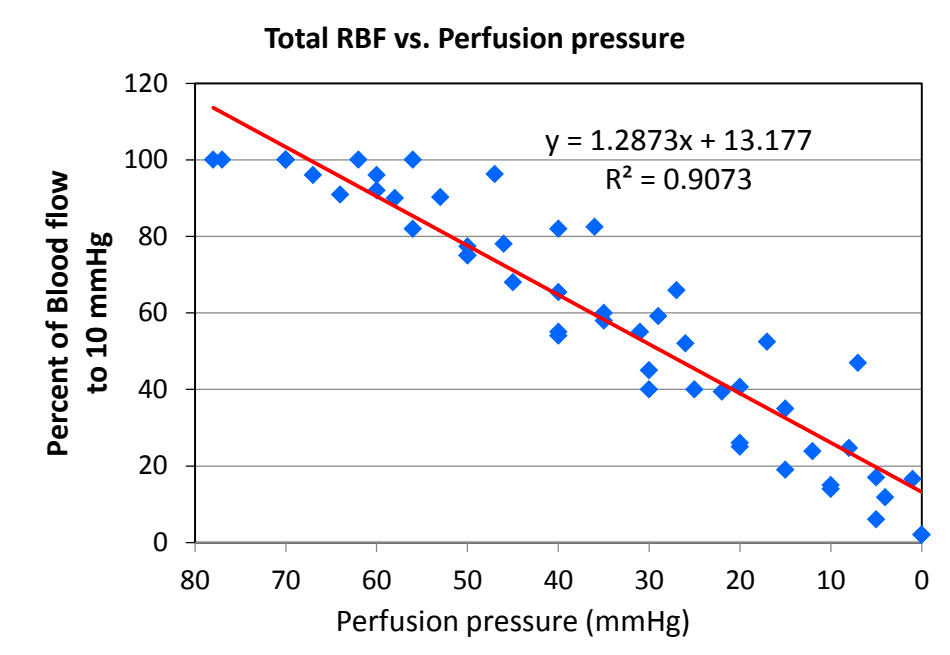

Fig.4.12 Total RBF decrease linearly with reduced perfusion pressure (when perfusion pressure < =70 mmHg).

4. 4 Conclusion and future work

UHS-OMAG can provide images of the retinal capillary microvasculature within different retinal layers and allows noninvasive monitoring of their response to elevated IOP. The capillary density is not significantly affected as long as IOP is lower than 50 mmHg (BP: 80±6 mmHg) or perfusion pressure higher than 40 mmHg. Beyond this range, capillary density decreases abruptly. In contrast, total RBF decreases linearly with increased IOP and decreased perfusion pressure. There is a difference between the capillary bed and total RBF response to increased IOP, or reduced perfusion pressure. This may be due to autoregulation of the capillary bed response to increasing IOP. Alternatively, capillary density change as revealed by UHS-OMAG may not adequately reflect the responses of capillary blood flow to changing IOP. These relationships will be further assessed in additional animals with higher levels of systemic blood pressure.

Chapter 5. Supercontinuum light source enabled ultra-high resolution OCT and OMAG

The objective of this chapter is to utilize the broadband Supercontinuum light source to achieve an ultra-high resolution OMAG for imaging true capillary vessels within tissue beds. As we discussed in chapter 1, the axial and lateral resolution of OCT is decoupled. The broadband light source can provide higher axial resolution and higher NA objective enables higher lateral resolution.

5.1 Introduction

Optical coherence tomography (OCT) is a noninvasive and noncontact interferometric technology that enables depth-resolved imaging of biological tissues at micrometer scale resolution. In general, the axial resolution is determined by the bandwidth of the light source used, which is given by $\delta z = 2(\ln 2)\, \lambda^2 / (\pi \Delta\lambda)$ where λ is the central wavelength and $\Delta\lambda$ is the spectral bandwidth. The wider the bandwidth, the more resolving power the OCT system is to differentiate the fine microstructures within tissue. The compact and cost effective superluminescent diodes (SLD), emitting in the spectral region centered around 800 nm or 1300 nm, are commonly used to implement the OCT systems. Unfortunately, the spectral bandwidth of the available SLDs is usually limited, which determines the achievable axial resolution at 7-10 μm for 800 nm and 10-20 μm for 1300 nm band light sources. In order to enhance the axial resolution, light source with broader spectral bandwidth has to be applied. Researchers attempted to integrate a number of SLDs with non-overlapping central wavelengths into one single broadband source for resolution improvement [107], but the improvement is suboptimal in terms of emitting wavelength of the multiplexed SLD that is typically centered at >900 nm, i.e, overlapping the water absorption at 980nm. A number of reports [108, 109] have demonstrated

the use of state-of-the-art femtosecond lasers can achieve a 2-3 μm axial resolution, but with the disadvantage of being expensive and bulky, limiting its uses to a few of research laboratories.

Being spectrally very broad and visually very bright, Supercontinuum (SC) light source has been attracted recently as an excellent alternative for OCT imaging to achieve sub-cellular axial resolution [110]. The feasibility of Fianium SC source for time-domain and spectral-domain OCT (SDOCT) has been demonstrated by Kurz group [111, 112]. Recently, Koch group [113] has successfully used a commercial available Koheras SC source to realize a dual-band SDOCT system for flexible imaging of tissue microstructures at either 800 nm or 1300 nm wavelength band. However, all these previous works are focused on using the SC light source to improve the system power to resolve the fine microstructures within tissue. No report has been so far demonstrated the feasibility of utilizing a SC light source to image tissue microcirculations.

As a variation of Fourier domain OCT, optical microangiography (OMAG) is a new imaging modality capable of generating 3D images of dynamic blood perfusion distribution within microcirculatory tissue beds. An unprecedented sensitivity to the blood flow down to 4 μm/s was reported with the recent development of an ultrahigh sensitive OMAG (UHS-OMAG). To achieve ultrahigh resolution and ultrahigh sensitive imaging of tissue microcirculations, here, we report the engineering of a SC source into an optic-fiber based UHS-OMAG system that provides a useable light source centered at 800 nm with a bandwidth of 120 nm. By applying the UHS-OMAG algorithm to extract the flow signal out of the static tissue background, we successfully achieved ultrahigh resolution imaging of not only the tissue microstructures, but more importantly the functional microvasculature. To the best of our knowledge, this is the first study that reports the utilization of the SC light source to achieve ultrahigh resolution imaging of microcirculations.

5.2 Material and methods

The schematic of the system is shown in Fig. 5.1a, which is an optic-fiber based SDOCT setup. The system layout is similar to the one published in [80], but with the design consideration and

the use of components that can handle the high intensity and broad bandwidth of SC light source. The light source applied was a SuperK Versa Supercontinuum Source (Koheras A/S, Denmark) pumped by a Nd:YAG laser, which provides an output spectrum from 460 nm to 2400 nm and an total output power of 1.5 W. The output light from the SC source was passed through an optical filter that was specially designed to filter and re-shape the incoming SC light into the light that centers at 800 nm with a bandwidth of 120 nm. The filtered light was then collimated and coupled into an optic-fiber (single mode) based SDOCT system via an optical circulator. All the optic-fiber components used were specified at 800 nm with a spectral bandwidth of at least 120 nm. The output power from the single-mode fiber in the sample arm was measured at ~12 mW. The spectral interferograms formed by the lights between the reference and sample arms were routed via the optical circulator into a home-built high-speed spectrometer. The spectrometer consisted of a collimating lens, a volume transmission grating and a CMOS line-scan camera. The camera had 4096 pixels and a maximum line scan rate of 70 kHz. The designed spectral resolution of the system was 0.044 nm that provides a ranging distance of 4 mm, implying that each pixel in the final OCT image practically represents ~1.9 μm. With these designs, the system sensitivity had a measured maximal roll-off of 20dB at the depth of 4 mm (Fig.5.1b).

However, since the penetration depth of NIR light is usually limited to within 2 mm in turbid medium, the meaningful system performance should only be considered for the ranging distance of 0-2mm. This is shown in Fig. 5.1c, where the averaged signal to noise ratio is rated at 87 dB, and importantly, the roll-off of system sensitivity is only ~7dB at the depth of 2 mm, which would no doubt improve the overall system performance of imaging the microcirculations within tissue beds *in vivo*. Meanwhile, we also evaluated the free space axial resolution along this depth range by using the full width at half maximum (FWHM) of the FFT amplitude signal as shown in Fig.5.1d. The achieved axial resolution is ~3.2 μm, slightly worse than the theoretical coherence gate 2.3 μm, probably due to the residual optical dispersion presented in the system.

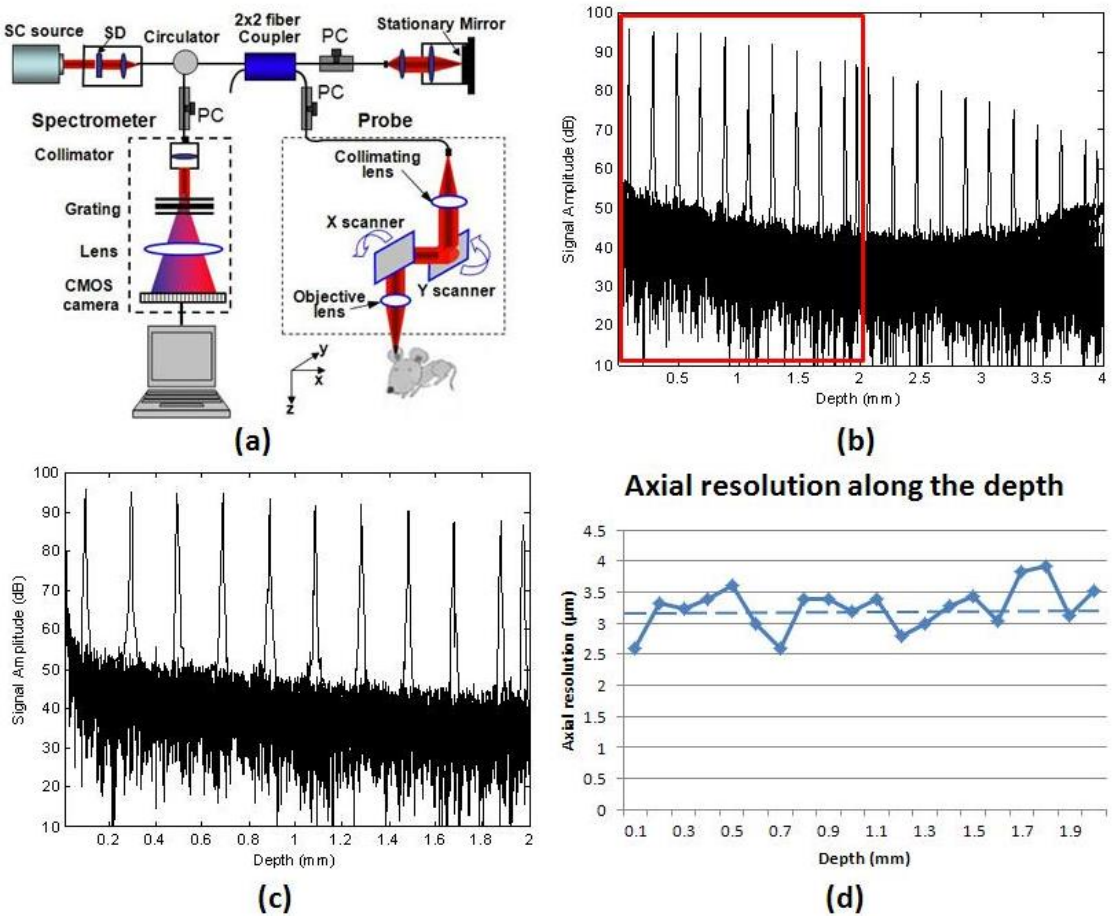

Fig. 5.1 Schematics of the system and characterization of its performance. (a) System setup, SD: spectral density filter. (b) Sensitivity falling off curve along the whole designed imaging depth and (c) the falling off curve within the meaningful depth range of 2mm (i.e, zoomed from the region square-marked in (b). (d) The evaluated free space axial resolution. Horizontal dash line is the mean value.

It is known that the capillary vessels have an average diameter between 6 – 8 μm. To resolve them well, the system design also needs to consider the lateral resolution besides the high axial resolution. Here, we adopted a microscopy objective lens with an effective focal length of 18 mm to deliver the probing light onto the sample. The beam spot size before the objective lens was measured at ~3.0 mm, giving a theoretical lateral resolution of ~ 5.8 μm. For UHS-OMAG imaging of microcirculations, a specially designed scanning protocol was used. In the fast-scan direction, 256 A-lines were captured to compose one B-scan cross sectional image (~80% duty cycle). By setting a ~4.6μm spatial interval between adjacent A-lines, each B-scan image covered

~1.2 mm range. In the slow-scan direction, 1000 B-frames were captured to cover ~1.2 mm range. The system imaging speed was set at 70,000 A-lines per second (the maximum camera speed). Due to the effective duty cycle of the fast scan and the data-transfer between the camera and the computer, the practical achievable frame rate of the system was 220 frames per second (fps). With this frame rate, it took only 4.5 seconds to finish one 3D scan that is short enough to minimize motion artifacts for *in vivo* imaging.

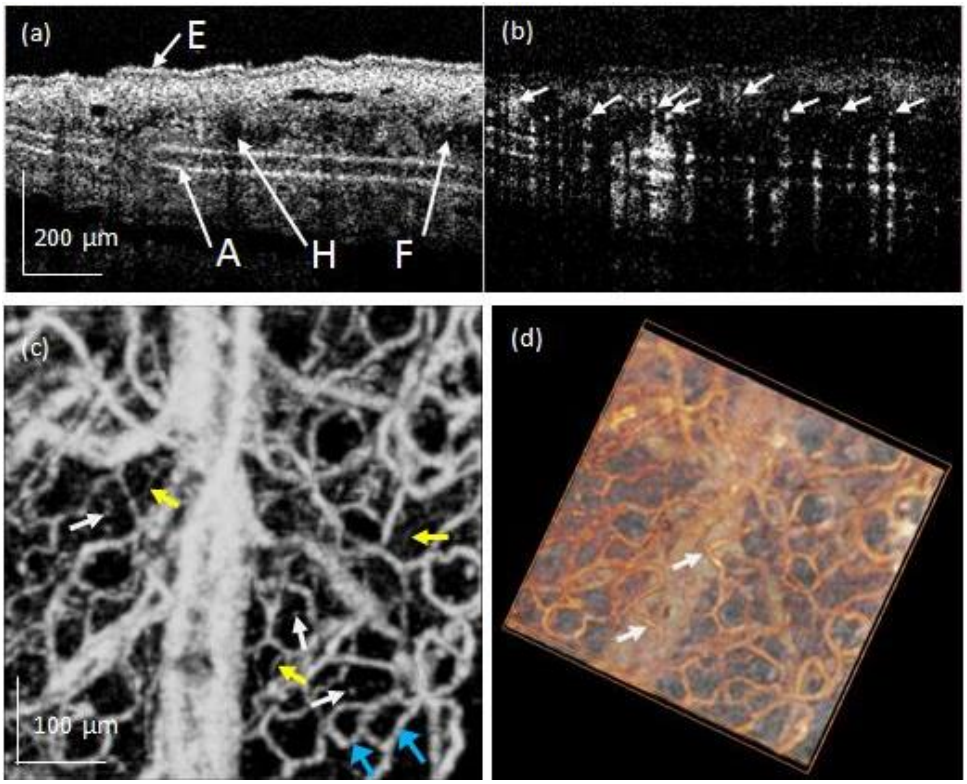

Fig. 5.2 (a) Cross-sectional structural image of mouse pinna *in vivo*, A: auricular cartilage, E: epidermis, H: hair follicle, F: fatty subcutaneous tissue; and (b) the corresponding blood flow image. (c) 2D projection view of a 3D OMAG image of blood vessels within a ~ 500 x 500 μm^2 area and (d) a 3D view rendered by merging structure with blood vessels.

5.3 Results

To demonstrate the capability of the designed UHS-OMAG system powered by the SC light source, we conducted experiments to image the capillary vessel networks lying within the mouse

pinna (ear) *in vivo* as well as the capillary loop within human finger cuticle. The scanning protocol described above was applied to capture a 3D data cube that covered $\sim 1.2 \times 1.2$ mm^2, onto which we applied UHS-OMAG algorithm to obtain both the structural and blood flow images.

Fig.5.2a shows a representative B-scan image of microstructure, where we can clearly identify the typical, layered microstructural features of the mouse pinna, e.g., epidermis, dermis and auricular cartilage. In addition, the ultrahigh resolution of the system also enabled us to distinguish some of the other particular features, such as the hair follicle and fatty subcutaneous tissue. Fig.5.2b gives the corresponding B-scan blood flow image where the abundant capillary blood vessels (pointed by arrows) are seen. To provide a clearer demonstration of the system capability to resolve single capillary vessels within tissue beds, Fig.5.2c gives the 2D projection view of a 3D OMAG image of microcirculation obtained from a field of view of 0.5x0.5 mm^2. Owing to its ultrahigh spatial resolution, the system was able to clearly identify the looped structures of the capillary network (blue arrows), a common feature in the skin microcirculation. The capillaries pointed by the yellow arrows have the measured diameter of ~6 μm, close to the lateral resolution of the system. Even the individual red blood cells (white arrows) moving in the capillaries can be identified in the OMAG flow image. Fig.5.2d illustrates a 3D view rendered by merging microstructural image with the blood vessel image, where the capillary vessels (white arrows) on the top of big vessel could be seen more clearly.

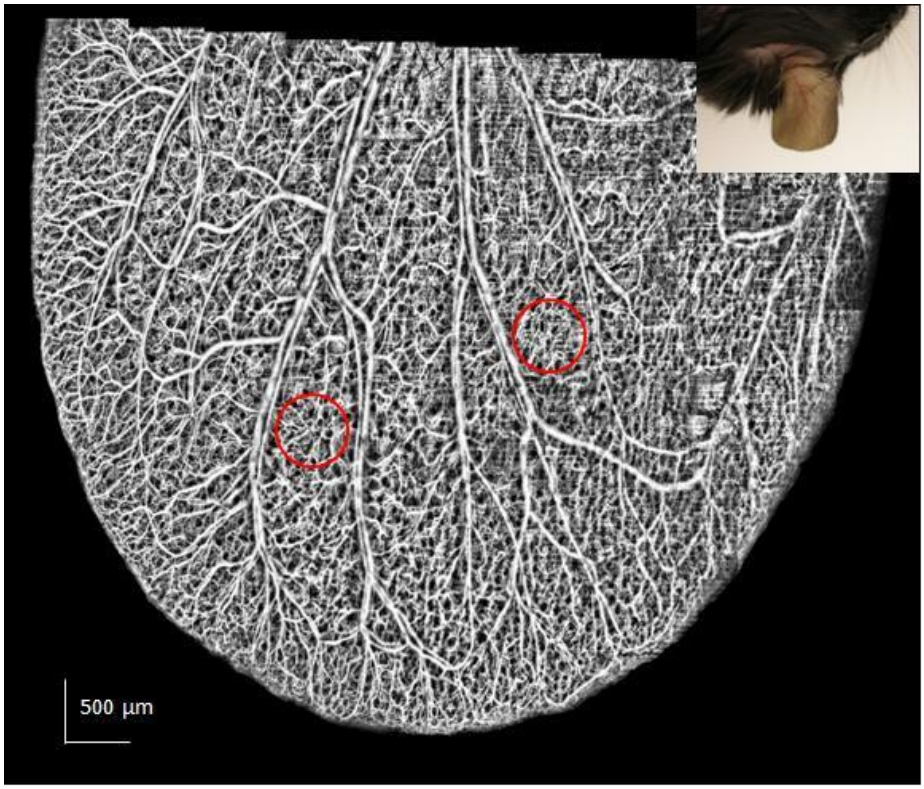

Fig. 5.3 Whole-ear vascular network of a living mouse imaged by SC light source coupled UHS-OMAG system. Inserted is the picture of the mouse ear.

The UHS-OMAG system has a broad detectable velocity range, from ~4µm/s to ~15mm/s, which enables us to image not only the big arteries and veins, but also the detailed capillary bed within tissue. By scanning multiple small regions and stitching them together afterwards, Fig.5.3 shows the detailed and impressive vascular perfusion map of the whole ear, where the inserted is a photograph of the mouse ear imaged. Since the densely patterned capillary beds and plexus (red circles) can be imaged and resolved clearly, this image demonstrates the power of the OMAG imaging of microcirculations within tissue beds *in vivo*.

Besides the mouse ear pinna, we applied the ultra-high resolution SDOCT on human skin imaging as well. Fig.5.4 shows the OCT cross-sectional structure of human finger cuticle and nail. Different layers of the skin and the junctions were clearly identified as shown in the Figure. More interestingly, we observed obvious birefringence of the muscle beneath the nail in the image.

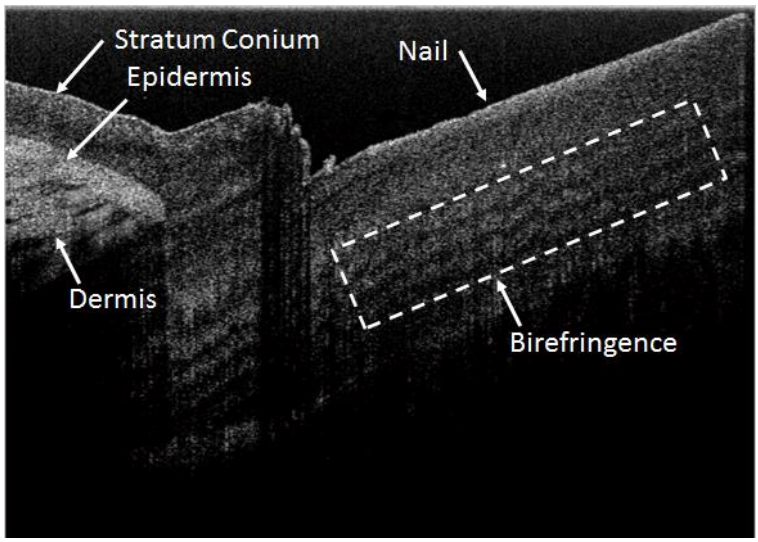

Fig. 5.4 Ultra-high resolution OCT cross-sectional structure of human finger cuticle and nail. We can observe the anatomical features of the skin and obvious birefringence caused by the muscle beneath the nail.

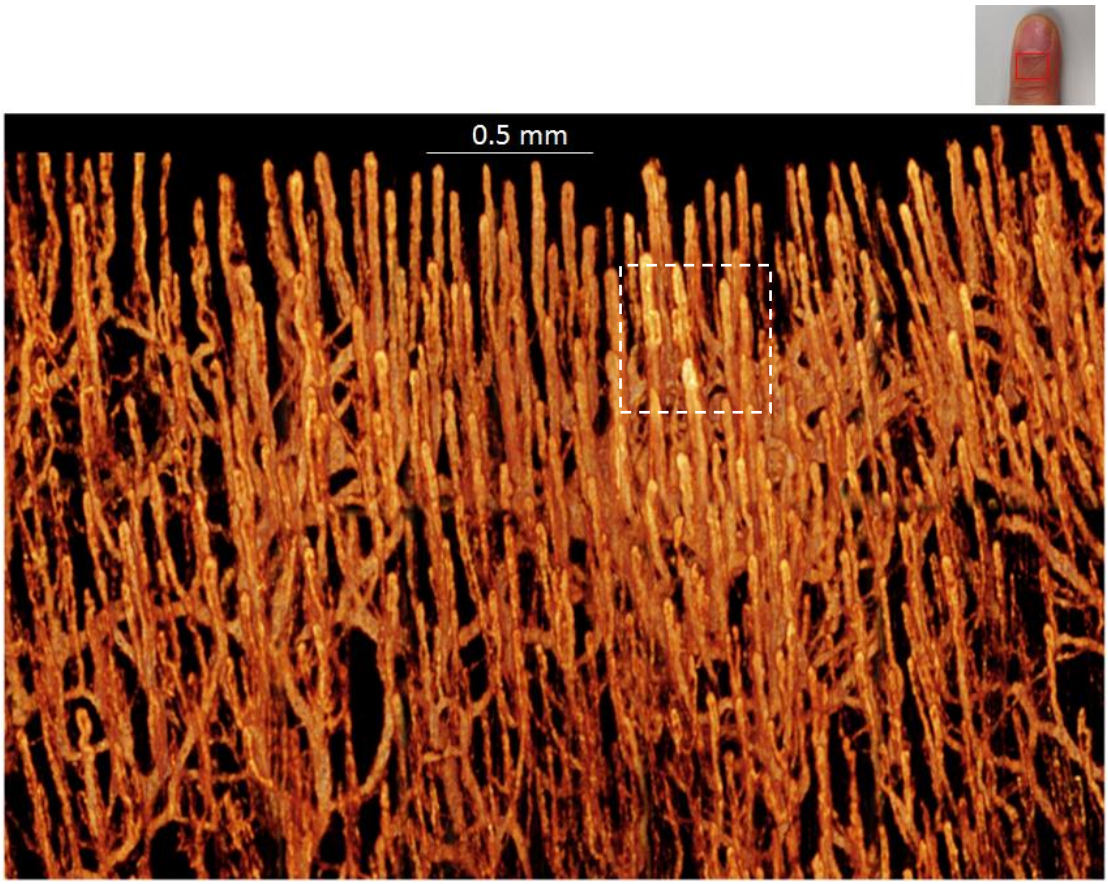

Fig. 5.5 Maximum intensity projection view of microvasculature of human finger cuticle. Fine capillary loop structure was observed clearly. Inserted is the photo of human finger, where the red square denotes the corresponding imaged area.

For the skin blood flow imaging, we developed a new image processing approach based on Eigendecomposition (ED). This ED based UHS-OMAG algorithm [114] can minimize the motion artifact without phase or motion compensation which can dramatically increasing the post-processing speed (at least 5 times faster than phase compensation based UHS-OMAG). After applying the UHS-OMAG algorithm, we could obtain the blood flow image as well. By stitching multiple small regions together, a large field of view (4.8 mm x 3.6mm) image showing the capillary loop in the finger cuticle are shown in Fig.5.5. The high resolution of the system enabled us to see the loop structure (white dashed box) clearly, i.e. one vessel going up, turn around and going down. To the best of our knowledge, this is the first demonstrated OCT angiography with capability of imaging such kind of loop structure.

5.4 Conclusion

In summary, we have constructed an UHS-OMAG system with ultra-high resolution and ultra-high sensitivity for imaging microcirculation within tissue beds by utilizing a broadband SC light source and high NA objective lens. The system provides an axial resolution of ~3 μm and a lateral resolution of ~ 6 μm in air. Within the depth range of 2mm, the system delivered an averaged SNR of 87 dB and a sensitivity falling-off of 7dB. With the use of the CMOS camera capable of 70 kHz A-scan rate, it has been shown that the system took less than 5 seconds to capture a 3D image for a field of view of 1.2x1.2 mm^2. The performance of the system for microvasculature imaging was demonstrated by showing high quality and impressive blood vessel network obtained from a mouse ear flap *in vivo* and human finger cuticle. Promising future applications of this high-resolution UHS-OMAG system for investigating microvascular involvements in various disease models, either for humans or small animals, could be expected.

Chapter 6. Label-free 3D imaging of microstructure, blood and lymphatic vessels within tissue beds in vivo

As we discussed in chapter 1, the microcirculation includes not only the capillary blood vessel network, but also the lymphatic blood vessels. The objective of this chapter is to develop system and methods for simultaneous label-free imaging of blood and lymphatic vessels using OCT. We have already demonstrated the capability of our ultra-high resolution UHSOMAG for imaging capillary blood vessel network in chapter 4, and here the challenge is label-free lymphangiography. In this chapter, we will first introduce the importance of lymphatic system and current lymphangiography technique, and then describe how ultra-high resolution OCT could be used for label-free lymphangiography, and finally we will apply our developed simultaneous label-free optical microangiography and lymphangiography to monitor the vascular and lymphatic response to wound punch and healing processing in mouse ear flap model.

6.1 Introduction

6.1.1 Background: Lymphatic vessel and lymphangiography

Lymphatic system is responsible for immune function and waste drainage [115]. Fig. 6.1 (right) shows the human immune system, which including the lymphatic organs, lymph nodes and lymphatic vessels. Lymphatic vessels are thin walled, valved structures that can collect and carry extra interstitial fluid (called lymph) from the body to ultimately drain back into the blood stream, which maintains the fluid balance. When we look into microcirculatory tissue beds (Fig. 6.1 left), the lymphatic vessels at the capillary bed are explored in detail. The forces that drive the fluid flow into the lymphatic capillary include the pressure gradient and the lymphokinetic motion. The valve structure in lymphatic vessels is also important to avoid the backflow of lymph.

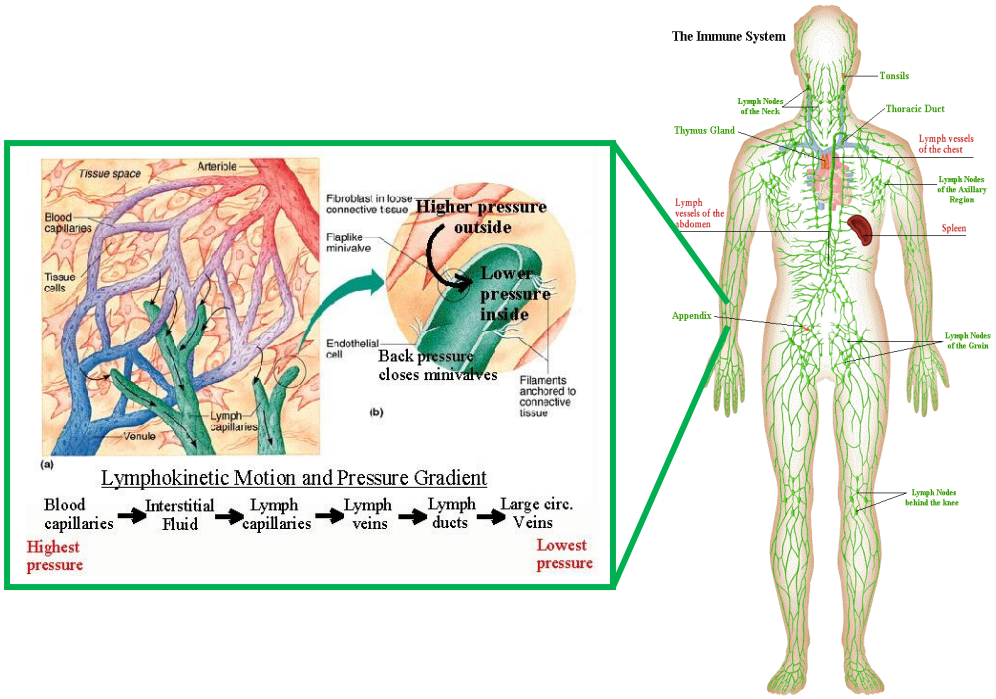

Fig. 6.1 (Left) The lymphatic system at the capillary bed. When fluids leak out of the capillary beds, the lymphatic capillary takes it up and returns it to circulation (Original image copyright Benjamin Cummings Publishing Company). (Right) The immune system of human body includes both the lymphatic organs and lymphatic vessels. The green network shows the lymphatic vessel network across the whole body. [Image adapted from website: http://www.rugusavay.com/how-does-our-body-fight-against-diseases].

Nowadays, people pay more and more attentions to study on lymphatic system. Firstly, clinical and pathological observations suggest that, transport of tumor cells via lymphatics is the most common pathway of initial dissemination for many carcinomas [25, 116, 117]. The lymphatic system, because of its physical proximity to many tissues of the body, is responsible for carrying cancerous cells between the various parts of the body. During metastasis, the intervening lymph nodes can trap the cancer cells and avoid the dissemination. If they are not successful in destroying the cancer cells the nodes may become sites of secondary tumors. Hence, the study of lymphatic drainage is important in diagnosis, prognosis, and treatment of cancer [118]. Secondly, lymphatic vessels can sprout at sites of inflammation [119]. Instant lymphatic vessel expansion and lymphangiogenesis always happen around wound area, which will be discussed in detail in the following part. Thirdly, dysfunctional lymph vessel can result in lymph edema, which is due

to extra tissue fluid cannot be drained properly. Lymph edema can cause severe problems for patient if not treated properly.

6.1.2 Lymphangiography

Visualization of the lymphatic system (lymph nodes and lymphatic vessels) plays a significant role in assessing patients with various malignancies and lymphedema [25, 26]. Most current methods for visualizing the lymphatic vessels require exogenous contrast agents [27], including but not limited to whole-mount immunofluorescence (LYVE_1), Evans blue dye imaging, fluorescence imaging, MRI, CT, Ultrasound and Photoacoustic imaging (Indocyanine Green dye as contrast agent) [28]. Unfortunately, the applicability of these methods is limited due to the difficulty of contrast agent uptake and their potential side effects. There is a need for a noninvasive and label-free method that can image the lymphatic vessel network *in vivo*.

Due to the relative low scattering property of lymph fluid, it appears almost transparent optically. In this regard, an endogenous contrast would be taken advantage by optical coherence tomography (OCT) [9], which is an interferometric technology using the intrinsic light scattering as image contrast. This was initially demonstrated by B. J. Vakoc et al. [38] using the negligible OCT scattering intensity from the lymph fluid to delineate lymph vessels, which was correlated with Evan's blue dye image. Our previous work that used label-free optical microangiography (OMAG), a variation of OCT technology) reported the 3D information of microcirculation that supplies the lymph node and efferent lymph vessels [120]. However, both of these works was unable to show lymphatic capillaries due to their limited spatial resolution. In order to distinguish the lymphatic vessel, especially the lymphatic capillaries from background tissue, ultrahigh resolution is required.

Another issue we wish to address is that to better understand the physiological function of the immune system, it is preferred to study the interaction between lymphatic circulation system and blood microcirculation. This requires high resolution imaging of microstructure, lymphatic and blood vessel network within tissue bed all together. In this letter we report the use of an ultrahigh

resolution OMAG system for simultaneous 3D imaging of microstructure, blood vessels and lymphatic vessels innervating the living perfused tissue beds without the use of any contrast agents.

6.2 Material and methods

6.2.1 Ultra-high resolution OMAG system

The OMAG system setup used here is similar to that previously reported [121]. Briefly, the system utilized a broadband supercontinuum light source as the illumination light, which provided a bandwidth of 120 nm centered on 800 nm, delivering an axial resolution of 2.3 μm in tissue. The objective lens with an effective focal length of 18 mm provides a measured lateral resolution of 5.8 μm. With the 2.3 μm axial and 5.8 μm lateral resolutions, we were able to image blood vessel and lymph vessel down to the capillary level within microcirculatory tissue beds. The high speed spectrometer that was used to capture the OCT interferograms employed a high speed CMOS line-scan camera with 4096 active pixel array (Basler SPL 4096-70 KM, Germany), capable of a maximum line scan rate at 70 kHz. The system had a measured sensitivity of 95 dB at the 0.5 mm depth position, dropped to 87 dB at 1.5 mm with 4.0 mw power incident on the sample.

6.2.2 Mouse ear model

To demonstrate the capability of our ultra-high resolution OAMG system and proposed segmentation method for simultaneous imaging of blood vessel and lymphatic vessel, we conducted experiments to image the microstructure, blood vessel and lymphatic vessel networks lying within the mouse ear pinna *in vivo*. C57 BL/6 mice (22 to 26 g) was immobilized in a stereotaxic stage and anesthetized with vaporized isoflurane (0.2 L/min oxygen and 0.8 L/min air). The body temperature was kept to 35.5 and 36.5 ◦C with use of a heat pad. The ear pinna was hair removed and placed flatten for imaging. All experimental animal procedures performed in this

study conform to the guidelines of the US National Institutes of Health. The laboratory animal protocol was approved by the Animal Care and Use Committee of University of Washington.

6.2.3 Data acquisition and image processing

In order to perform simultaneous 3D imaging of blood and lymphatic vessels, we applied the OMAG scanning protocol reported in [80] for this study. A 3D data volume with 256 A-lines and 1024 B-frames (256 cross-sections with 4 B-frames at each cross-section) was captured to cover a field of view of 1.2 x 1.2 mm^2. With the camera running at 70 kHz line scan rate, it provided an image acquisition rate of 220 frames per second. Under this configuration, the whole 3D dataset was acquired within 5 seconds, which minimized the possible motion artifact.

By processing the data using the OMAG algorithm [121], we were able to simultaneously obtain two images: microstructure and blood flow images. The microstructure image at each cross-section was obtained by averaging four images captured at the same cross-section, which reduced the random noise and made the microstructure image smooth. Finally, the lymphatic vessel image was extracted from the microstructure image.

We developed an automatic segmentation algorithm for the extraction of lymphatic vessel from the OCT microstructure image (Fig.6.2), based on the fact that the lymph fluid is optically transparent, thus giving optical signals near the system noise floor. The segmentation program was developed on OpenCV environment, which is an image processing library. In the program, an adaptive threshold was first calculated by the intensity of the pixels within a local window around a target pixel to perform binarization operation. The window size was designed to be adjustable according to local lymphatic vessel size. If the intensity of target pixel was lower than the adaptive threshold, then that target pixel was judged to belong to lymphatic vessel, and assigned to a value of 1; otherwise it was assigned to 0. Finally, the processing was performed frame by frame for the whole 3D dataset to obtain a final 3D data volume, showing the lymphatic vessels only. Compared to the method that used only one fixed threshold to perform binarization

for the whole image, the use of the adaptive threshold can extract the target tissue at where the intensities of both target tissue and surrounding tissue are either high or low.

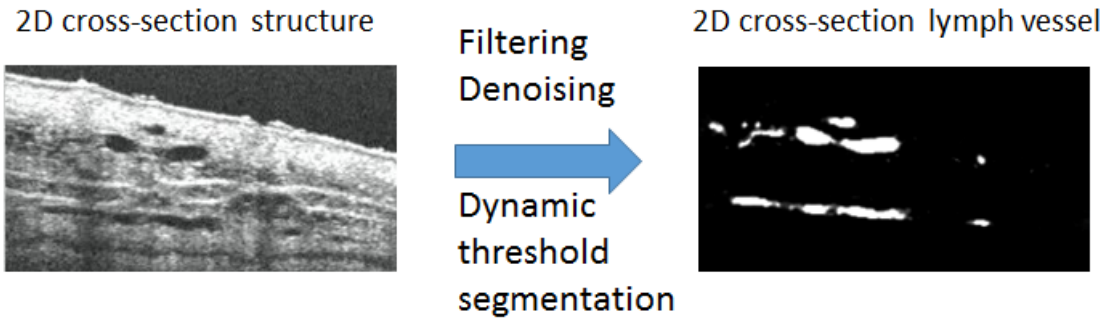

Fig. 6.2 2D Segmentation of lymphatic vessel based on the OCT structure image.

6.3 Results

6.3.1 3D label-free lymphangiography

Fig.6.3 shows results of depth-resolved lymphatic vessels from living mouse ear tissue. Fig.6.3 (b) illustrates one typical cross-sectional microstructure image that slices through lymphatic vessels, the lumen of which gives the low optical scattering signals (appearing black in the image) due to the optical transparency of the flowing lymph fluid. Fig.6.3 (a) plots the signal intensity over the depth along the red line marked in (b), demonstrating there is almost no optical signal measured from the lumen of lymphatic vessel. Since the OMAG/OCT is depth-resolved imaging tool, the captured 3D dataset can be manipulated to show detailed microstructure information in any orientations. Fig.6.3 (c) and (d) are two en-face images that were extracted at the depth positions of 80 and 40 μm respectively, showing different lymphatic vessel patterns. With the proposed segmentation algorithm applied, 3D lymphatic vessel network within the scanned tissue volume can be obtained (Fig.6.3 (e)), which can be merged with the 3D microstructural image to show in detail how the lymphatic vessels are distributed within the tissue beds (Fig.6.3 (f)).

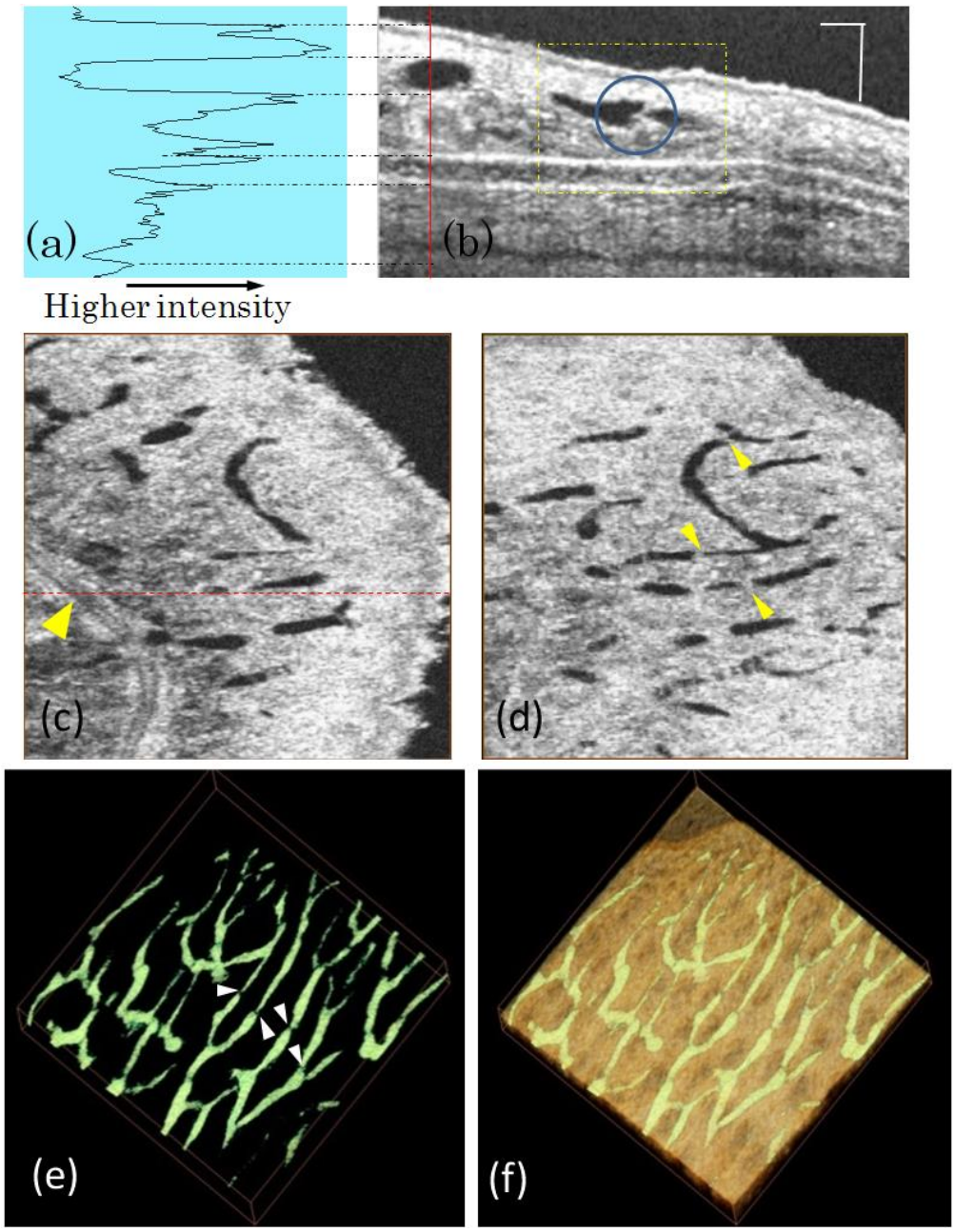

Fig. 6.3 Ultra-high resolution OCT image based lymphangiography. (a) Plot of signal intensity along the red line in, (b) one typical cross-sectional microstructure image of mouse ear; (c) en-face image of mouse ear at the depth of 80 μm, where the red dashed line indicates the cross-section in (b) and yellow arrow points to a blood vessel; (d) en-face image at the depth of 40 μm; (e) 3D lymphatic vessel network and (f) 3D merge of lymphatic vessel with the microstructure image. Scale bar= 100 μm and image size for (c)-(f) is 1.2 x1.2 $mm^{2.}$

Most importantly, the spatial resolution afforded by our current imaging system enables the visualization of the one-way valve of lymphatic vessels, which prevent any backward flow. The sernilunar shaped lymphatic valve is marked by a blue circle in Fig.6.3 (b) and pointed by arrows in Fig.6.3 (d) and (e) as well.

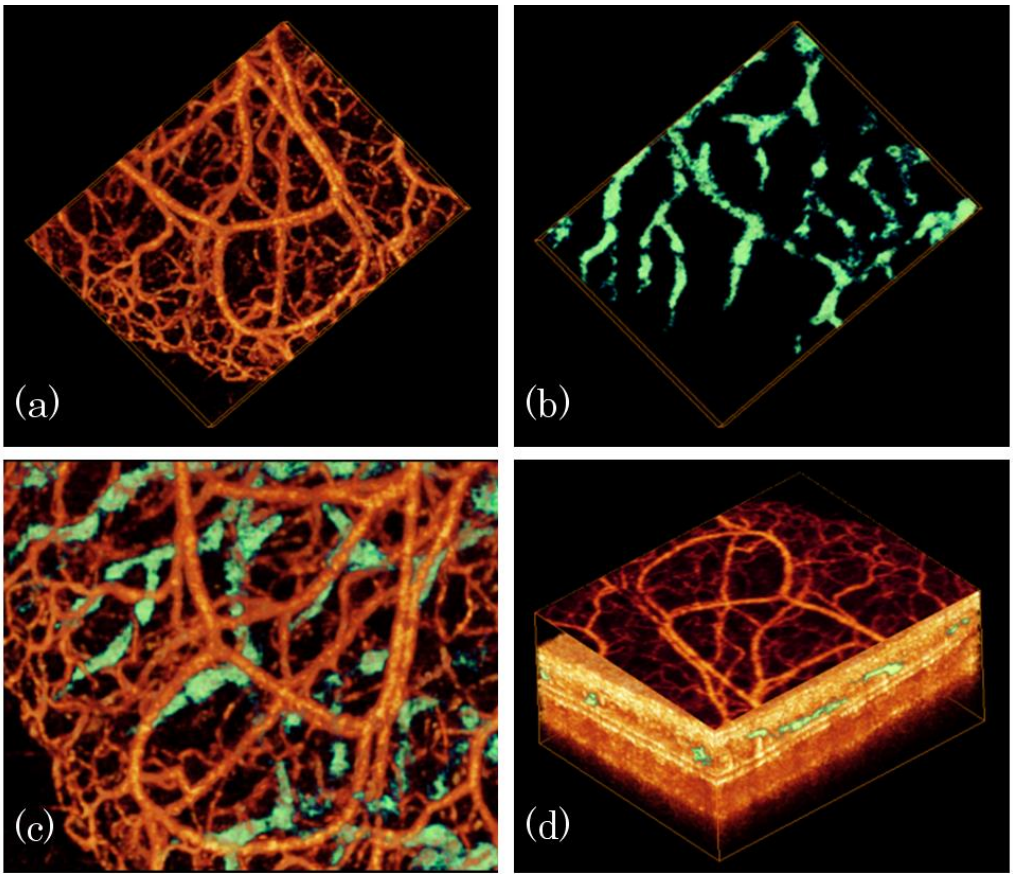

Fig. 6.4 *In vivo* simultaneous 3D angiography and lymphangiography of mouse ear pinna. (a) Blood vessel image, (b) lymphatic vessel, (c) combined blood and lymphatic vessel image and (d) projection view of blood vessel lying on merged microstructure and lymphatic vessel image.

Fig.6.4 demonstrates the capability of the proposed system and segmentation method for simultaneous 3D vascular-angiography and lymphangiography where Fig.6.4 (a) and (b) show blood vessel image and lymphatic vessel image, respectively, obtained from the same tissue volume. One advantage of the OMAG modality is that it is capable of providing co-registered and depth-resolved blood flow and lymphatic flow images in parallel. Thus, we merged the lymphatic vessels together with the blood vessels [Fig.6.4 (c)] to better appreciate their positional

relationship. Together with Fig.6.3, we noticed that lymphatic capillaries are closed at one end, which appearance is different from blood capillaries that are usually connected at both ends. According to the standard physiology textbook, this is due to that the function of lymphatic capillary is to drain excess tissue fluids within the extracellular space that must flow in one direction only. Fig.6.4 (d) shows a maximum intensity projection view of blood vessels lying on the merged microstructure and lymphatic vessel image.

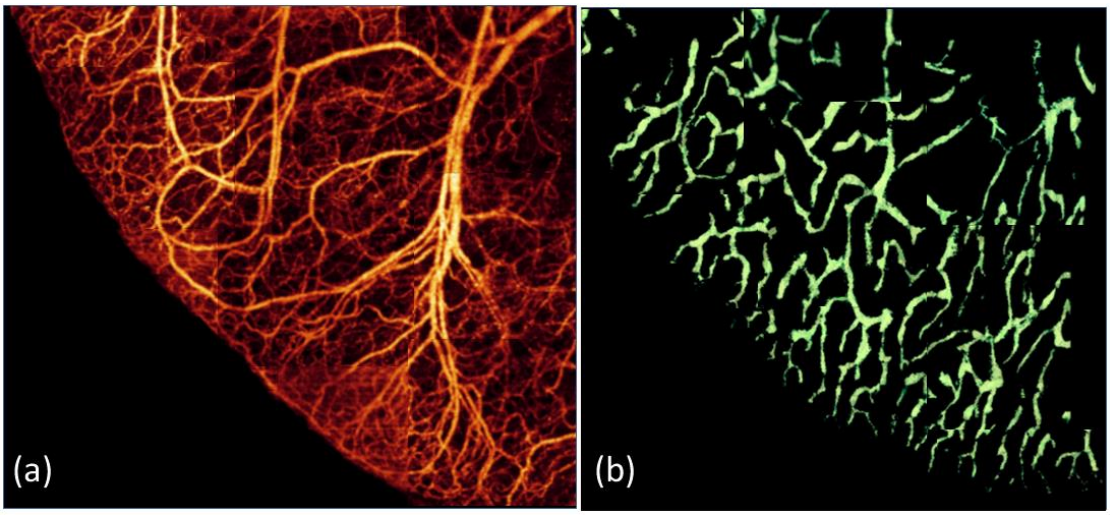

Fig. 6.5 Wide field (4 x 4mm^2) projection view of (a) blood vessel map and (b) lymphatic vessel network captured within the same tissue beds stitched by multiple images.

Fig.6.5 shows a wide projection view of the detailed (a) blood vessel and (b) lymphatic vessel network within a scanned microcirculatory tissue beds covering 4 x 4mm^2 of the mouse ear. Both dense blood capillary and lymph capillary could be visualized and correlated with each other. Without the need for exogenous contrast agents, OMAG thus have potential to monitor functional lymphatic and blood vessels within the tissue beds in vivo both locally and globally. Notably, the OMAG lymphangiography can be performed simultaneously with the tissue morphology and vascular microangiography; and these can be done from one single OMAG volumetric scan.

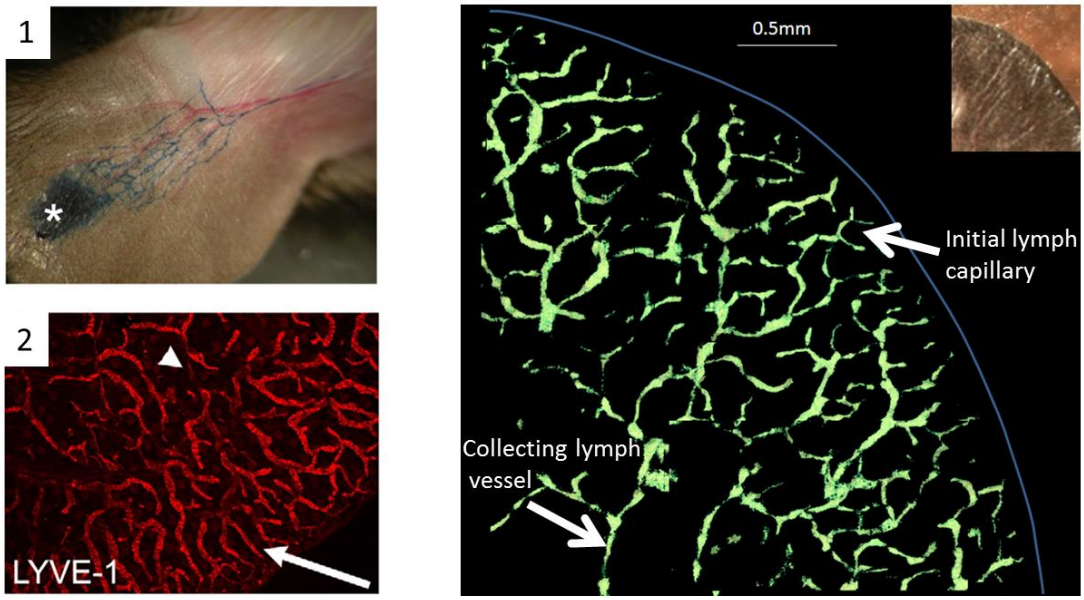

Fig. 6.6 Comparison of OCT based label-free lymphangiography with labeling required methods. (A) Lymphangiography with injection of Evan's blue dye (adapted from [122]), only large collecting lymph vessels are visualized; (B) Immunofluorescence method using LYVE-1 labeling (adapted from [122]), only superficial small initial lymph capillaries are shown; (C) OCT based label-free lymphangiography, where both collecting lymph vessels initial lymph capillaries are imaged, insert is the corresponding mouse ear pinna imaged.

Analyses of morphological features of blood vessels, lymphatic vessels and microstructures of the microcirculatory tissue beds *in vivo* afforded by the 3D OCT dataset provides detailed information about blood flow in both lymphatic tissue volumes and individual circulation vessels. Previous methods, such as Intravital Microscopy [123] and Multiphoton Microscopy [124], have been limited to small field of view and superficial depths (< 200μm), and often required labeling contrast agents to reveal the lymph vessels. OCT is superior in visualizing complex morphological features, blood and lymph vessel networks deeper (> 200μm) and without the use of the contrast agents. Fig. 6.6 shows the comparison of OCT based label-free lymphangiography with labeling required methods. As compared with Evan's blue dye injection method, ultra-high resolution OCT is superior in resolution and sensitivity as it can reveal the small initial lymphatic capillaries. Whereas, compared with Immunofluorescence method using LYVE-1 labeling, OCT

can image deeper collecting lymph vessel. Thus, ultra-high resolution OCT based label-free lymphangiography may be a useful tool for the investigations of potential mechanisms of the normal physiological functions as to lymph and blood perfusions, as well as their responses to the therapeutic treatment under diseased conditions, e.g., inflammation and cancer.

6.4 Monitoring blood vessel and lymphatic vessel response to wound punch and healing in mouse ear pinna model

6.4.1 Background and motivation

Cutaneous wounds are common and include incisions/lacerations, abrasions, contusions, puncture wounds, burns and ulcers. Complications during the cutaneous wound healing process are a significant healthcare challenge and economic concern. Each year it is estimated that over one million people are treated for burn injury alone [125]. In addition to undesirable scar formation, skin wounds often become severely infected which can become fatal. Skin damage due to a wound, burn or illness may lead to major complications, such as diabetic ulcers, psoriasis and bed sores [125-127].

One of the main goals during tissue repair is to achieve rapid wound closure. Recent advances in cellular and molecular biology have determined that the basic biological processes involved in wound healing are inflammation, tissue formation and tissue remodeling [128, 129]. The vasculature must be a key player in promoting tissue survival and repair during these processes as it carries the tissue's blood supply and is the site for initiation of inflammatory events in the affected area. However, little is known about the changes which occur to the vasculature after tissue damage and during repair. To design effective treatments, further understanding of both vasculature, lymphatics and tissue restoration during wound healing is required.

In the present work, we approach the feasibility of OMAG to track the tissue and vascular remodeling as well as lymphatic vessel response in a wound induced by a biopsy punch on the

mouse pinna *in vivo*. We demonstrate for the first time that the ultra-high resolution, UHS-OMAG system is capable of visualizing capillary networks (~5 μm), and determining tissue structure and the corresponding vascular and lymphatics reaction due to a biopsy wound.

6.4.2 Material and method

To determine whether the developed ultra-high resolution UHS-OMAG could noninvasively track the vascular architecture, lymphatic vessel and structural changes within the tissue during the wound healing process, four SKH1-E mice (22 to 26 g) (Charles River, Holllister, CA) were imaged at various time points after a wound was induced with a biopsy punch. Animals were subjected to a 12 h light and dark cycle, and allowed to drink and eat *ad libitum*.

Mice were anesthetized with isoflurane (0.2 L/min oxygen and 0.8 L/min air) by a face mask. The pinna was immobilized with double-sided tape onto a glass slide to minimize motion artifacts. As a control, the mouse pinna was imaged using OMAG system prior to the wound. To induce a wound in the ear, a 0.5 mm size biopsy punch was sterilized, placed on the dorsal side of the pinna and used to punch a round hole through the skin. The bleeding was washed out with medical grade saline. After onset of the wound, OMAG imaging was obtained from the same regions as the control image. OMAG images were obtained at 30 minutes and 4, 8,12,18,22,26,32,46 and 60 days on the same animal after the biopsy punch to monitor the chronic wound healing process.

6.4.3 Results: blood vessel response to wound punch and healing

To correlate observed changes in structural thickness with vascular development, the data was processed as a depth-resolved image. A line (data not shown) was assigned to the highest point on the control image. Any vessel structure below this line is depicted in a yellow color and any vessel structure higher than this line is designated as a red color. Therefore the red color in Fig.6.7 and Fig.6.8 represents an increased structural thickness when compared with the baseline image. As wound healing progresses, the thickness gradually returns to baseline levels.

In the lower right hand panel of Fig.6.7, a picture of the pinna was taken at day 4 and 60, and after 60 days no wound is visible by eye.

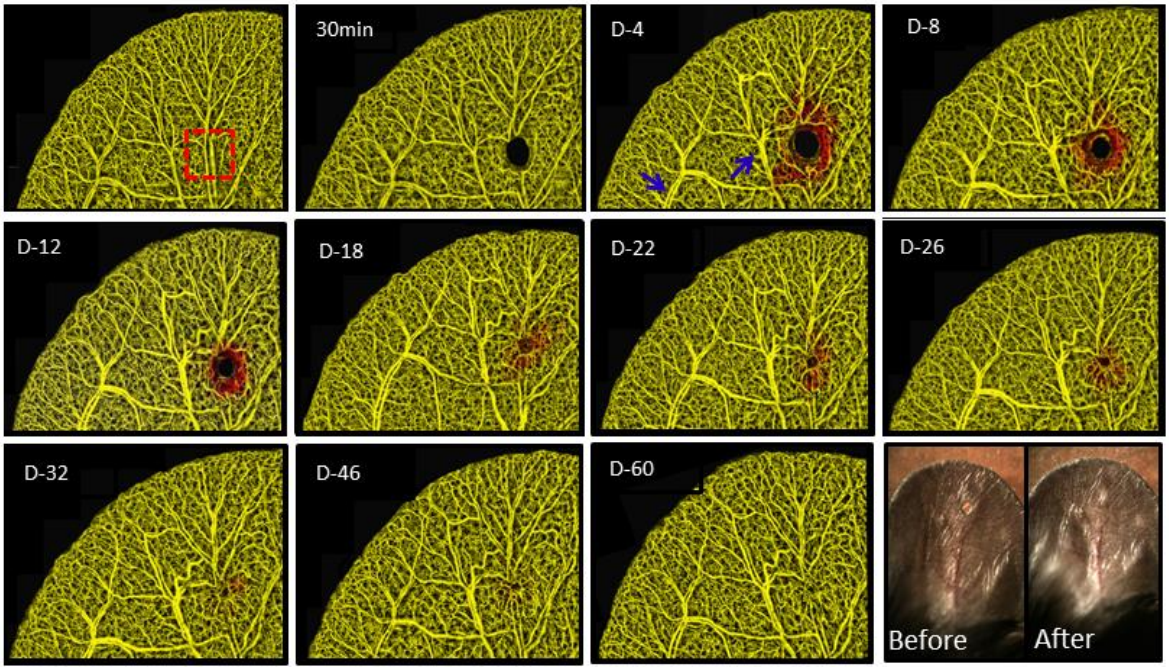

Fig. 6.7 Projection view OMAG images of the pinna before and after wound induced by biopsy punch *in vivo* at different time points. The red color indicates vasculature within thicker tissue compared to the baseline control. Compared to baseline, progressive vessel regulation (vessels pointed by blue arrows) and neovascularization observed as red looped vessels surrounding the wound develop at 4 days after punch biopsy was induced. In the lower right corner, a light photograph of the wound at days 4 and 60.

The high resolution achieved by our system enabled us to visualize morphological details. Fig.6.8 shows enlarged microangiography images of the wound area corresponding to the positions marked by the dashed-line red square and biopsy punch over 30 min to 60 days in Fig.6.7. After the wound induction, the tissue and blood flow was totally absent as shown by the black holes in Fig.6.7 and Fig.6.8. Because OMAG only renders images from which there is blood flow, lack of flow appeared as a black space. Fig. 8 shows the formation of functional vessels along with the increased thickness of the pinna around the area of the wound by day 4 (white arrow). This growth of new vasculature is coiled and torturous in nature suggesting angiogenesis. By day 18, numerous capillaries are present within newly generated tissue.

Fig.6.8B shows the area of the wound size, which was quantified for both the structure and blood vessel images (Fig. 6.8A). New tissue formation occurred at a high rate between days 12 to day 22 as shown by the decreased wounds structure size as new tissue is generated and cells migrate toward each other. We also estimated the wound size based on the blood vessel images. The wound size estimated by the blood vessel image reaches a peak of ~ 0.11mm^2 compared to ~0.075 mm^2 estimated by the structure image. The blood vessel wound size is larger than the structure wound size because there was no blood flow surrounding the wound 30 min after the biopsy punch. In Fig. 6.8A, this is most apparent at day 4 where the edge of the wound is visible and the absence of vessels is apparent (blue arrow).

Fractal dimension was used to quantify the blood vessel tortuosity during the wound healing process. Briefly, the vessels were segmented and a binary image was created and skeletonized. The fractal dimension was calculated over the skeletonized image within a small window (~100 μm x100 μm). Two circles (a small and a large) centered at the wound were created as shown in Fig.6.6 at 30 min. The mean and standard deviation of the fractal dimension at the periphery of the circle was calculated for each time point (Fig.6.8 C). In the small circle, the fractal dimension disappears after the wound (as expected given that there are no vessels present). The vessels reappear and stabilize at a fractal dimension value 20% higher than the baseline at 60 days. This indicates that the new vessels formed are more tortuous as typically observed in angiogenic vessel formation. The vessels in the large circle have a ~10% increase in fractal dimension after the wound. This value remains fairly constant throughout time. The increase is possibly due to the recruitment of existing capillary vessels.

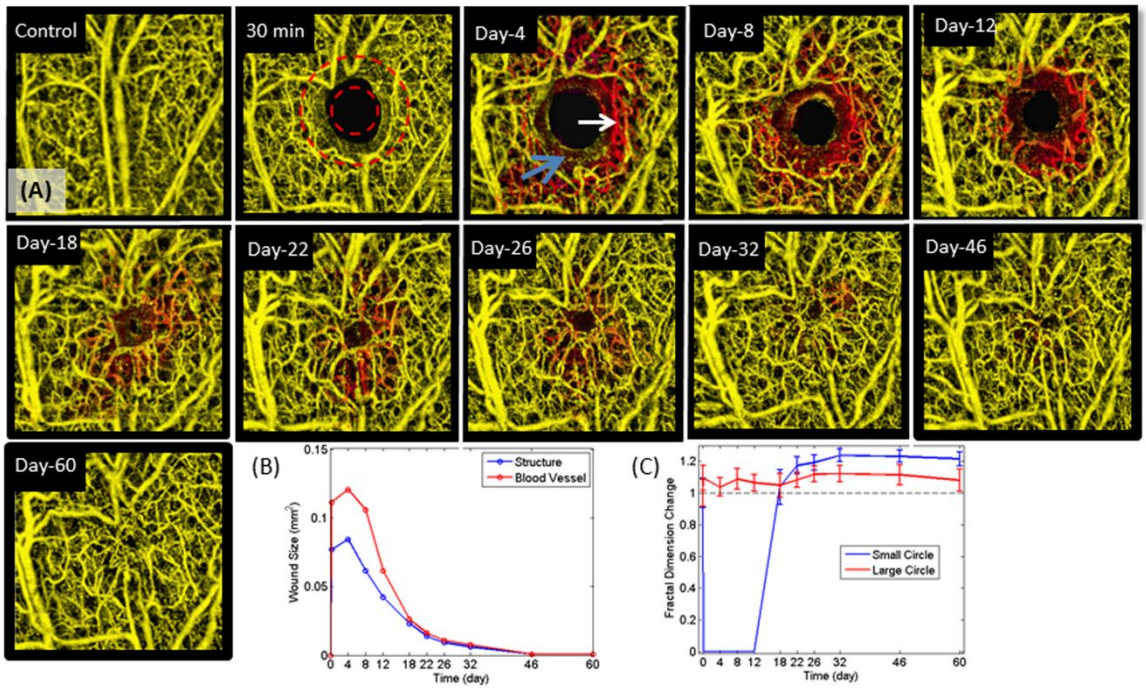

Fig. 6.8 Depth-resolved projection view and corresponding changes in wound size and fractal dimension over time. (A) Projection view of the OMAG wound vasculature for the different time points in Fig.5.7 for a small field of view (1.2 mm×1.2 mm). (B) Size of the wound at different time points. These were calculated by the size of the structure wound (white arrow in day 4) and blood vessel wound (blue arrow in day 4). (C) Mean and standard deviation of the change in the fractal dimension value calculated at the periphery of a small and large circle around the wound (indicated in the 30 min image).

6.4.4 Results: lymphatic vessel response to wound punch and healing

To monitor the dynamic response of lymphatic vessel to wound punch and healing, we further processed the microstructure videos as discussed above to obtain the lymphatic vessel network changes. All these are obtained from the same dataset and no extra scanning are required.

Fig. 6.9 shows the results of cross-sectional microstructure images and corresponding color-coded depth maximum projection view of lymphatic vessel network during 3weeks after punch. As we can see from the cross-sectional microstructure images (a-d), the total thickness of ear flap as well as the epidermal thickness is increased after punch (Fig. 6.9b) and during the healing period. This is supposed to be related to the tissue inflammation, which is a protective mechanism. From these cross-sectional microstructure images, we can also see the lymphatic vessels are

increased in size right after punch. In day 7 (Fig. 6.9c), both the number and size of the dark holes (lymphatic vessel) are maximized. After that the size and number will reduce and return to the original state at day21 (Fig. 6.9d). Right panel color-coded depth maximum projection images can better show this process. The white dashed circle show the size change of punched hole, which indicates the wound healing happens during the process as the hole size is much smaller at day 21 (Fig. 6.9h). Before the punch, the lymphatic vessels are small and due to the limitation of our system resolution, we couldn't see much lymphatic except for large collecting lymphatic vessels. Right after punch (day 0, Fig. 6.9e), we see obvious increased size and density of the lymphatic vessel within the white circle. And at day 7 (Fig. 6.9g), there is large and dense lymphatic vessel over the whole ear. Whereas at day 21(Fig. 6.9h), the lymphatic vessel size and density is reduced back to original states.

Based on the above observations, we hypothesized that i) both lymphatic vessel size increase and lymphangiogenesis happened during the punch and healing process; ii) there is a relationship between the lymphatic vessel size and the epidermal thickness, which is related to the tissue inflammation to wound. Future work will be conducted to evaluate this hypothesis, which is important for better understanding the mechanism of tissue response to wound and help accelerate the healing process.

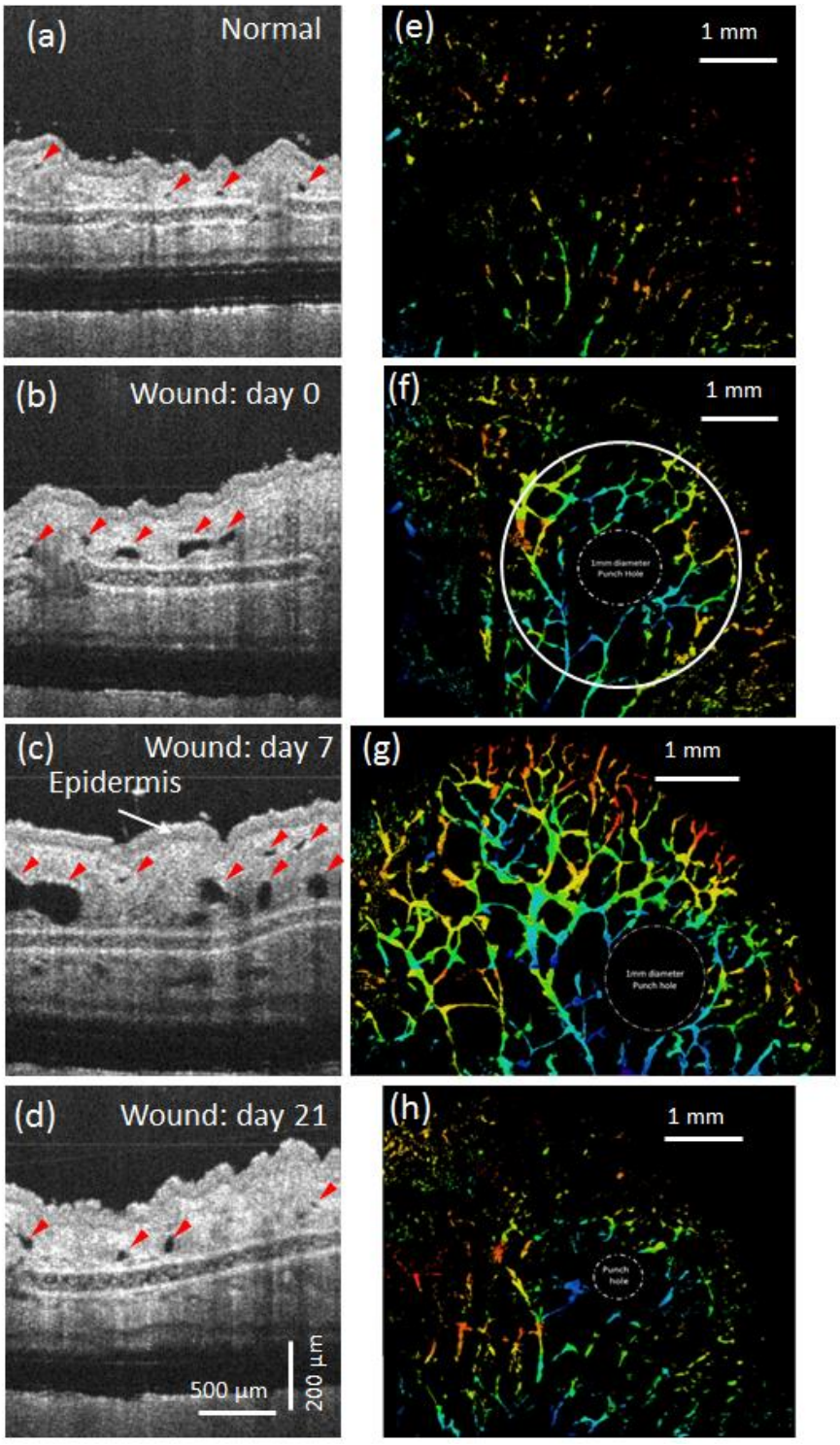

Fig. 6.9 (a-d) Cross-sectional microstructure images showing the lymphatic vessel size and density changes within 3 weeks after wound punch. Red arrows point to lymphatic vessels (dark holes). Normal is before punch and day 0 is ~ 5 min after punch. (e-h) Corresponding color-coded depth MIP view of lymphatic vessel network change during the wound healing process.

6.5 Conclusion and future work

In conclusion, we have demonstrated that ultrahigh resolution OAMG is able to achieve simultaneous 3D label-free lymphangiography and vascular-angiography coupled with detailed tissue morphology *in vivo*. With the system, we were able to monitor the blood vessel and lymphatic vessel response to a biopsy punch wound and healing on mouse ear pinna model. Blood vessel angiogenesis through the whole process was recorded. Inflammation related lymphatic vessel expansion and possible lymphangiogenesis was observed with a peak in around one week after the punch. We have also demonstrated that the high resolution afforded by OMAG enables the visualization of the lymphatic valve structure, promising future investigation of the lymph flow dynamics within deep microcirculatory tissue beds that has not been possible previously. In future, the quantitative measurement of blood vessel and lymphatic vessel density can be done as well for better evaluation of the wound healing process.

The technique we presented here shows great capability for characterizing blood vessel angiogenesis and lymphangiogenesis which is associated with the occurrence of various diseases especially tumor [130]. During tumor growth, blood vessel angiogenesis are required to provide the nutrients and oxygen for tumor tissue growing, while the lymphatic vessel network play key role for the transportation of tumor cells during tumor metastasis. Simultaneous imaging of blood and lymphatic vessel is essential for better evaluation of tumor growth and metastasis. Hence, our future work would be focus on applying our developed technique for studying the microenvironment of tumor.

Chapter 7. Noninvasive Imaging of Retinal Morphology and Microvasculature in Obese Mice using Optical Coherence Tomography and Optical Microangiography

Purpose: To evaluate early diabetes-induced changes in retinal thickness and microvasculature in a type II diabetic mouse model using optical coherence tomography/optical microangiography (OCT/OMAG).

7.1 Introduction

Diabetic retinopathy (DR) is the most common microvascular complication of diabetes and it is one of the leading causes of blindness worldwide [131]. DR can be classified into 2 stages: non-proliferative and proliferative. The earliest visible signs in non-proliferative DR are microaneurysms and retinal hemorrhages. Prolonged hyperglycemia can lead to severe pathological changes in the retina, leading to proliferative retinopathy with retinal neovascularization and diabetic macular edema (DME). Early diagnosis and prevention of retinopathy in diabetic patients is crucial for preventing vision loss [132]. Invasive imaging techniques, e.g., fluorescein angiography (FA) [133] and indo-cyanine green angiography (ICGA) [134], are currently used to visualize ocular perfusion and detect abnormal vessels. Both techniques have traditionally been utilized to make diagnoses and treatment decisions, but they can only provide two-dimensional (2D) images and require intravascular injections that risk complications, including anaphylaxis. A noninvasive imaging technique with the capability of detecting early changes in DR, such as retinal structural and microvascular alterations would be critical.

Optical coherence tomography (OCT) is a non-contact, non-invasive imaging modality that has been widely used for human retinal imaging [9]. Functional OCT can provide important clinical information that is not available in the typical intensity-based structural OCT images.

Doppler OCT and OCT angiography techniques have attracted increased attention in the clinical community because of their utility in studying functional changes in microvascular pathology *in vivo*. Phase-resolved Doppler OCT (PRDOCT) [17, 18] has been applied to quantify blood flow in human retina.[70, 135] On the other hand, in order to visualize the microcirculation network, a number of technological strategies have recently emerged that provide improved imaging contrast for microvasculature components, e.g. OCT angiography. Optical microangiography (OMAG) is one of the earliest OCT angiography methods, capable of generating 3D images of dynamic blood perfusion distribution within microcirculatory tissue beds *in vivo*. Most recently, OMAG has been extended to ultra-high sensitive OMAG (UHS-OMAG) that dramatically improves the detection sensitivity to slower blood flow velocities to a level that enables the imaging of true capillaries within the scanned tissue volume. We have demonstrated its capability for volumetric imaging of retinal vasculature and quantitative measurement of retinal blood flow in rats [72, 136], and mice [137].

Because most structural, functional and biochemical studies cannot be carried out in human subjects, animal models are essential for studying DR pathology and for developing new and better therapeutic strategies to treat human diseases [138]. Mouse models of DR have proven useful for studying DR and evaluating novel therapies due to their amenability to genetic manipulation [139-143]. Type 2 diabetes (DM2) is a progressive disease that generally has an onset in adulthood and accounts for over 90% of all diabetes cases. A recently developed mouse strain BTBR with the *ob/ob* leptin-deficiency mutation develops Type 2 diabetes, hypercholesterolemia, elevated triglycerides, and insulin resistance [144-148].

The purpose of this study is to investigate the early signs of DR, including the retinal thickness, microvasculature changes and total RBF change in a diabetic mouse model of Type 2 diabetes and obesity using the OCT/OMAG system. As shown in our results, the retinal thickness measured from the NFL to IPL and total retinal blood flow was significantly lower in the obese mice, whereas there is no obvious alteration in the retinal capillary density.

7.2 Material and Methods

7.2.1 Animal Model

22 week old female BTBR *ob/ob* leptin-deficiency mutation mice (OB, N=10) and BTBR wild type control mice (WT, N=10), bred at the University of Washington as previously described [144], were used in this study. BTBR ob/ob mice develop type 2 diabetes [144] and develop several diabetic complications including morphologically advanced nephropathy and cardiomyopathy. It is not yet known whether these mice are capable of developing a robust, advanced proliferative retinopathy resembling morphologically advanced diabetic retinopathy. The BTBR ob/ob mice used here weigh an average of 63.9 ± 2.2 g and have elevated serum glucose levels that exceed 600 mg/dl. In comparison, control WT mice have an average weight of 32.6 ± 1.4 g and serum glucose levels of 242 ± 27 mg/dl. The average systolic blood pressure of BTBR ob/ob mice was 120.3 ± 9.2 mm Hg and diastolic blood pressure was 83.7 ± 6.4 mm Hg. Whereas, the average systolic blood pressure of WT was 89.8 ±4.2 mm Hg and diastolic blood pressure was 66.6 ± 3.6 mm Hg. Both of the average systolic blood pressure and diastolic blood pressure of BTBR ob/ob mice are significantly ($p<0.05$) higher than WT mice which means BTBR ob/ob mice are hypotensive compared with WT. The measured axial eye length for the WT and OB mice are 3.624 ± 0.071 mm (N =10) and 3.591 ± 0.047 (N =10). There is no significant difference between them. All animals were treated in accordance with the ARVO Statement for the Use of Animals in Ophthalmic and Vision Research, and the animal protocol was approved by the Animal Care and Use Committee at University of Washington.

7.2.2 Optical coherence tomography/Optical microangiography system

A SDOCT-based OMAG system was used in this study to acquire in vivo 3D datasets of retinal microstructure and microvasculature. The system has been previously described in detail [137]. Here we briefly provide some key parameters that specifically determine the system performance for mouse eye imaging. The system was operated at a central wavelength of 840 nm with a

spectral bandwidth of 42 nm, providing an axial resolution approximately 7.2 μm in air. The detector used was a high speed CMOS line scan camera (Basler Sprint spL2048-140 km), having 10 μm square pixels in two rows and 2048 pixels wide. In order to increase the camera speed, only 896 pixels were illuminated and the camera was read at an exposure time of 5.7 μs which provided a line scan rate of 140 kHz, i.e. 140,000 A-scans per second. In the sample arm, we applied an ocular lens (Ocular Instrument, Maxlight Standard 90D) that enables both a large field of view (~2x2 mm2) and an acceptable lateral resolution (~10 μm) of the mouse retina.

7.2.3 Image acquisition and processing

The mice were anesthetized with inhalational isoflurane (1.5%) mixed with 80% air and 20% oxygen, positioned in a custom-made head holder, and the right eye was prepared for OCT/OMAG imaging. The pupil was dilated with eye drops (10% phenylephrine hydrochloride ophthalmic solution, USP, AK-Dilate™). 3D data volumes covering the optic nerve head (ONH) area with a size of ~ 2x2 mm^2 were first captured using the UHS-OMAG scanning protocol [80], in which the raster scanning of the beam spot was performed to capture 512 A-lines within each B-frame (2D cross-sectional image) and 2000 B-frames for each C-scan (3D image). These 2000 B-frames were captured at 400 cross-sections with 5 repeated B-frames captured at each cross-section position. Using a frame rate of 220 frames per second (fps), we were able to obtain a single 3D data volume in about 7 seconds. We then captured another 3D dataset (using 2048 A-lines per B-frame and a frame rate of 35 fps) covering a region of ~ 1x1 mm^2 around ONH for PRDOCT analysis to determine the axial blood flow velocity in retinal arteries and veins [137]. During the procedure, the position of the mice was unchanged and the eye movement was minimal.

The 3D OMAG data were post-processed using the UHS-OMAG algorithm [29, 72], i.e. high pass filtering along the C-scan direction to extract the blood flow signal out of the background tissue. At each cross-section, the phase-compensated complex signal of adjacent B-frames were

subtracted and then averaged (four times) to obtain the cross-sectional structural image (see Fig. 7.1A) and its corresponding blood flow image (see Fig. 7.1C). This was applied in all of the 400 cross-sections to generate concurrent 3D structural and blood flow movies. The 3D retinal structure and microvascular network were rendered using Amira 3D software (Visage Imaging, Inc.). An example of the maximum intensity projection map of the retinal microvasculature in a typical mouse is shown in Fig. 7.1D.

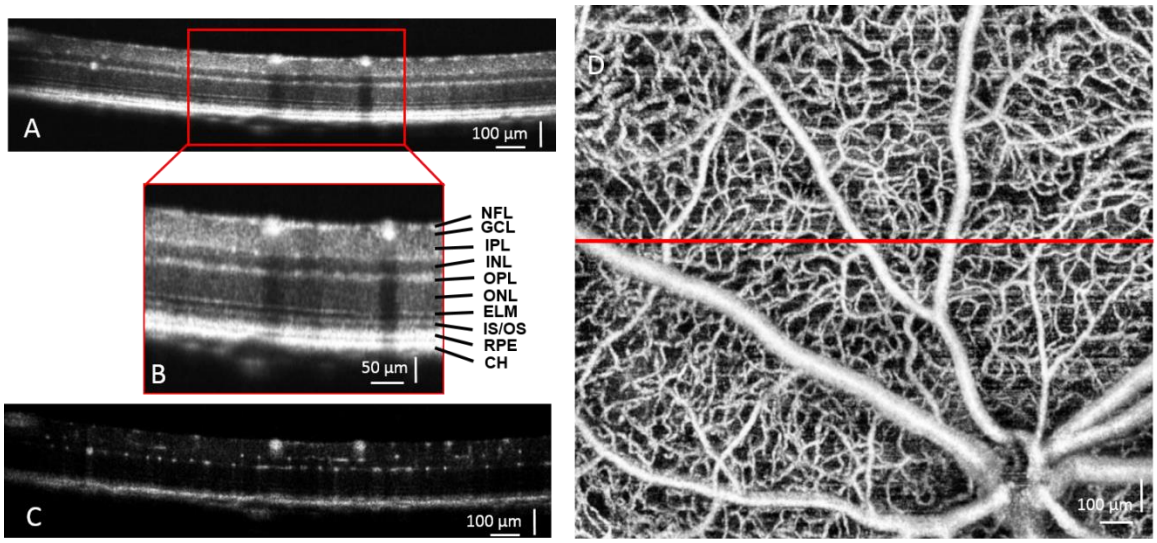

Fig. 7.1 Ultrahigh-resolution OCT/OMAG images from a normal WT BTBR mouse. **(A)** Cross-sectional OCT structural image of the retina; (**B**, inset) High magnification demonstrating the resolved retinal and choroidal layers. NFL: nerve fiber layer, GCL: ganglion cell layer, IPL: inner plexiform layer, INL: inner nuclear layer, OPL: outer plexiform layer, ONL: outer nuclear layer, ELM: external limiting membrane, IS/OS: junction between the inner and outer segment of the photoreceptors, RPE: retinal pigment epithelium layer, CH: choroid. **(C)** Corresponding cross-sectional blood flow image obtained by comparing the 5 repeated B-frames captured at the same cross-section. **(D)** Maximum intensity projection map of mouse retinal microvasculature generated by OMAG. The *red line* indicates where the cross-section is shown in (**A**).

7.2.4 Retinal segmentation and thickness measurement

A semi-automated retinal layer segmentation algorithm developed by our research group was used to segment individual retinal layers from the OCT cross-sectional structural images based on the intensity difference (Fig. 7.2A). This was conducted on the entire 3D data volume. After

segmentation, the thickness of the nerve fiber layer (NFL) (Fig. 7.2B) and the thickness from the NFL to the inner plexiform layer (in short, NFL-IPL) (Fig. 7.2C) were calculated. These results were captured from a BTBR wild type mouse. As we can see from the thickness map, the thickness of the measured retinal layers decreases with distance away from the ONH, consistent to what has been previously reported [149]. We report the retinal thickness in each of the concentric circles according to the distance from the center of the ONH (Fig. 7.2 D and E). For each retina, the mean thickness (MT) is calculated as the average thickness of the whole scanned area.

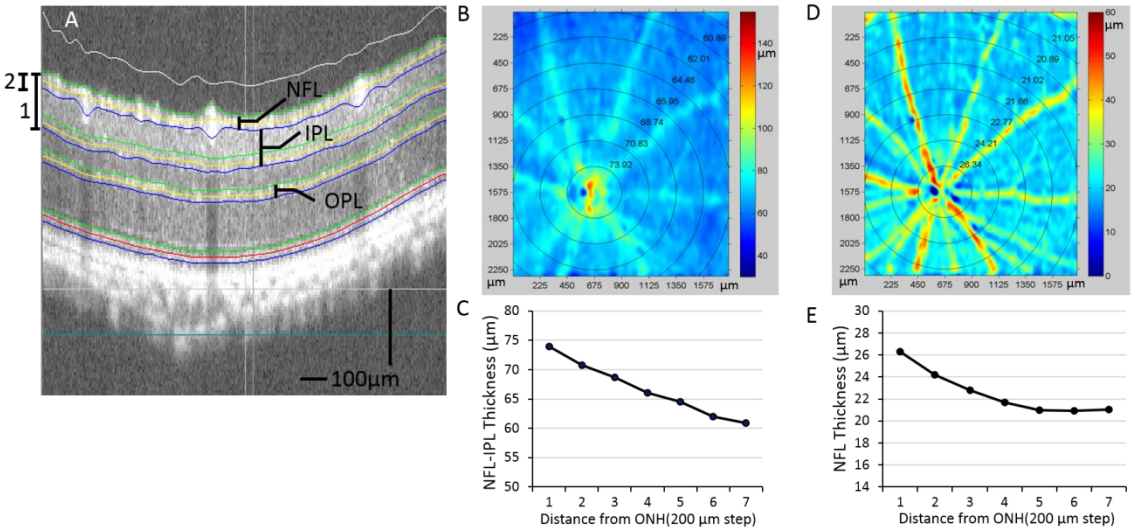

Fig. 7.2 Retinal layer segmentation and thickness measurements. **(A)** OCT images from the 3D OCT data set are segmented and interfaces are identified by the center line (yellow) and boundary (green and blue). **(B)** Pseudocolor image of NFL-IPL thickness (Labeled as *1* in **(A)**) from an OB mouse. The mean thicknesses within the concentric regions of varying distances from ONH are shown on top of the thickness map and plotted in **(C)**. **(D)** Pseudocolor image of NFL thickness (Labeled as *2* in **(A)**). Similarly, the mean thicknesses within the circular region are shown on top and plotted in **(E)**.

7.2.5 Measurement of Retinal Capillary Density

Retinal capillary dropout is a hallmark of both early and late diabetic retinopathy. Hence, the ability to quantify retinal capillary density can potentially be an important early indicator in the evaluation of diabetic-induced changes. We quantified capillary density in the IPL and OPL

layers by measuring the number of capillaries intersected by a 500 μm straight line [150]. For each retina, 12 locations were chosen for measurement according to the distance and angle to the ONH. 12 measurements of capillary density were averaged for the IPL and OPL capillary layers in 10 wild type and 10 OB mice.

7.2.6 Measurement of total retinal blood flow rate

Total RBF rate measurements were performed using the elegant *en face* Doppler method demonstrated by Srinivasan et al [47]. We have also described the approach for the measurement of total blood flow rate in mouse retina in detail [137]. The detailed method has been presented in chapter 4 and we will apply the same approach. Briefly, axial flow velocity within a three-dimensional volume around the ONH was measured. Then, by re-orienting the velocity map into an *en face* view, an *en face* plane can be chosen that bisects all of the retinal arteries and veins. By integrating the axial flow components over the vessel cross-sections, the total RBF can be obtained without knowing the Doppler angle. The total RBF was computed by adding either together the arterial or venous flow. We computed the total RBF as the average of arterial and venous flow in the right eyes of 10 WT and 10 OB mice.

7.2.7 Statistical Analysis

Data are presented as mean ± SEM. The differences in retinal layer thickness, capillary density and total retinal blood flow between the WT- and OB-mice groups were analyzed using Student's t-test by determining the p-value, where it is assumed that the sample populations are normally distributed. The criterion for a statistical significance was $p < 0.05$.

7.3 Results

Retinal thickness measurements were performed after layer segmentation of the retinal structural images. The mean thickness of the NFL and NFL-IPL layers in WT control mice (N =10) and diabetic OB mice (N =10) are presented in Fig. 7.3. The WT control mice have a mean NFL thickness of 21.9 ± 1.8 μm and the diabetic OB mice have a mean thickness of 21.5 ± 2.4 μm. There was no statistical difference observed between these two groups. However, the mean

thickness of the NFL-IPL in diabetic OB mice was significantly lower (65.1 ± 2.1 μm, **p <0.01) than that of the WT control mice (71.9 ± 1.5 μm). Thickness from the OPL to RPE was also measured, and no significant difference was found between the two groups (data not shown).

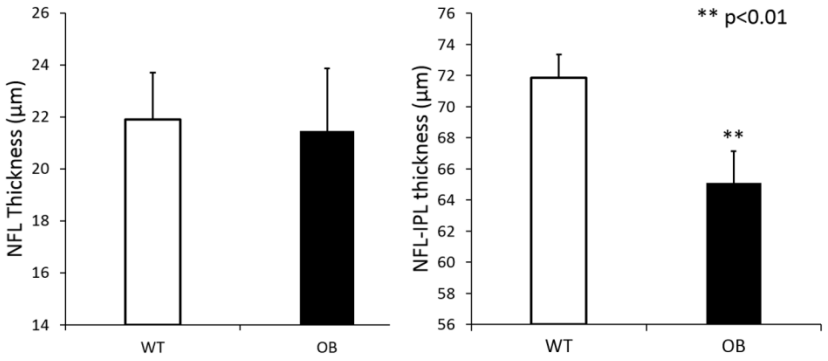

Fig. 7.3 Decrease in NFL-IPL thickness in OB mouse retinas compared to WT mouse retinas. **(A)** Mean thickness of NFL in WT control mice (N =10) and diabetic OB mice (N =10). No statistical difference was observed between the two groups. **(B)** Mean thickness of NFL-IPL in WT control mice (N =10) and diabetic OB mice (N =10), with the NFL-IPL thickness measured from retinal surface to the posterior limit of IPL layer. **P < 0.01 between the two groups. Data are presented as means ± SE.

The OMAG imaging technique can provide depth-resolved imaging (Fig. 7.4A) of the microvasculature in the mouse retina with a large field of view. In the holangiotic retina, there are, schematically speaking, three layers of microvessels: a superficial microvessel network in ganglion cell layer, an intermediate capillary network in the inner plexiform layer, and a deep microvessel network in the outer plexiform layer [104]. Hence, we segmented the vasculature into these three different layers based on the architecture of the murine retinal microvascular network (Fig. 7.4B-D). With this high resolution and depth-resolved microvasculature map, we were able to track the blood flow path through the three retinal layers (Fig. 7.4E-H). As we know, the blood flow in outer retinal layers is supplied by the central retinal artery which usually divides into 4-6 major arteriole branches. Each major arteriole branch will then separate into small precapillary arterioles (Fig. 7.4E). Notably, the superficial layer is predominantly precapillary arterioles (Fig. 7.4E) which then dive into the intermediate layer. After an asymmetric cross path in the IPL as intermediate capillaries, they either dive into the OPL to form the deep microvessels

or join the venules directly (*white arrow* in Fig. 7.4F). The venous-end capillary flow in the deep layer of OPL is then collected by postcapillary venules (Fig. 7.4G), which finally joins with major venules in the superficial layer. From our images, we can see that these postcapillary venules may either be connected to the major venules directly or by passing through the intermediate layer. Finally, all of the blood flow returns back to the central retinal vein (Fig. 7.4H). To the best of our knowledge, this is the first time that the murine capillary network has been imaged in such three-dimensional structural detail in an *in vivo* and non-invasive method. With this capability, we expect to be able to detect retinal microvascular changes in the diabetic OB mice in comparison to the wild type mice.

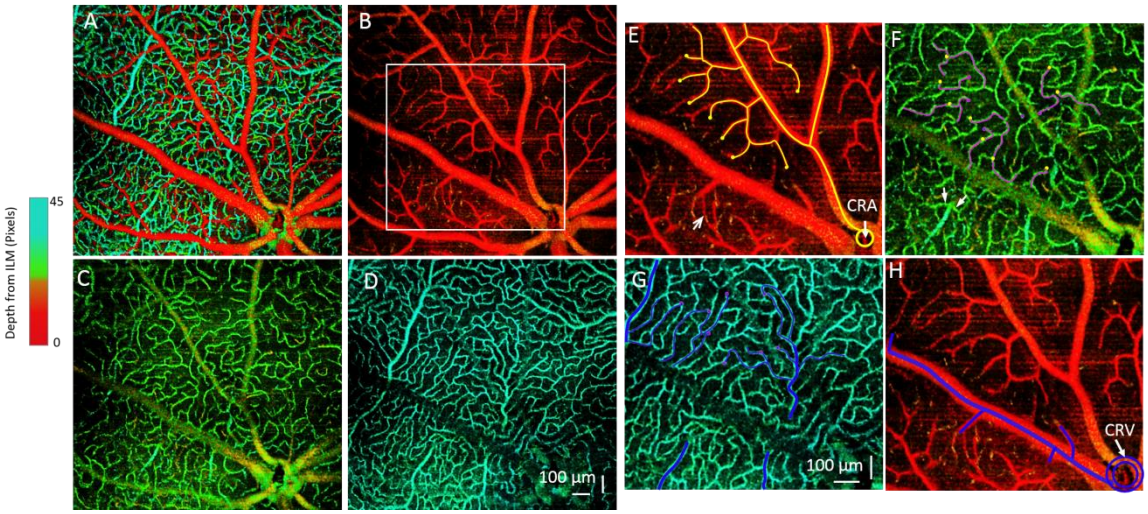

Fig. 7.4 Depth-resolved retinal microvascular network and 3D tracking of the blood flow capillary by capillary. **(A)** Depth-coded color angiography of the whole mouse retina. **(B-D)** Microvascular network within three different layers, **(B)** GCL, **(C)** IPL, **(D)** OPL. The microvascular organization within the three layers has distinct patterns. **(E-H)** Tracking of the microvessel paths of an arteriole and venule demarcated in the *white rectangular region in* **(B)**. **(E)** In the superficial microvessels of GCL, the blood flows through arterioles branched from central retinal artery *(CRA)*, shown as the *yellow lines.* The *yellow dots* denote where the vessels diving to a separate layer. *Arrow* points to a direct arteriovenular connection in the superficial GCL layer. **(F)** Intermediate capillary layer in the IPL. *Yellow dots* indicate the vessels that are diving to this layer from the superficial layer in (E). These capillaries flow as *pink lines* and then dive into deeper layer at the *pink dots*. *Arrows* point to capillaries joining the postcapillary venules. **(G)** Deep layer microvessel in OPL, with the pink dots from IPL indicating diving vessels and flow as *blue lines*. All of the

blood flow will be then collected by the postcapillary venules and returned back to the superficial layer, and to **(H)** the major venules which will join the central retinal vein *(CRV)*.

In order to quantitatively compare the capillary vessel density between the WT control and diabetic OB mice, we measured the linear capillary density by determining the number of capillaries crossed by a 500 μm line (Fig. 7.5A-B). For each retina, we randomly chose twelve counts and averaged them to obtain the mean value. The linear capillary density in the IPL is usually less dense than the deep capillaries in the OPL. No statistical difference was found between the WT control mice (N =10) and diabetic OB mice (N =10) for both capillary density in either the IPL or OPL (Fig. 7.5C).

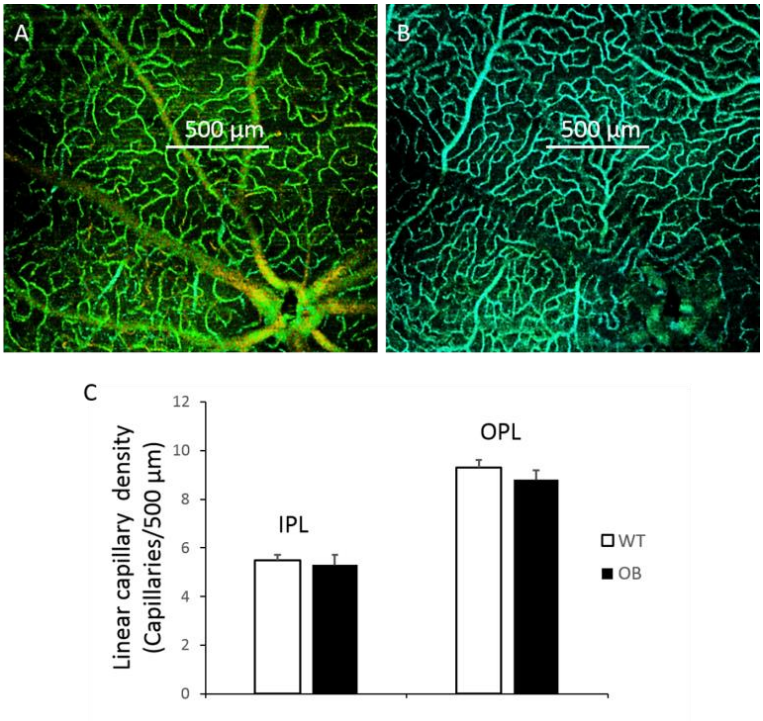

Fig. 7.5 Determination of retinal capillary density in WT and OB mouse retinas. Measurement of linear capillary density as determined by the number of capillaries crossing a 500 μm line in the intermediate capillary layer (A) and in (B) deep layer. (C) Linear capillary density in WT control mice (N =10) and diabetic OB mice (N =10). No statistical difference was found between the two groups. Data are presented as means ± SE.

We next measured the total RBF in all the mice involved in this study using the *en face* Doppler approach [137]. Interestingly, while the capillary density was unchanged between the

two groups, we found that the total RBF in the diabetic OB mice (N =10) was significantly lower than that in normal WT mice (N =10) (Fig. 7.6). The mean total RBF rate in WT mice is 3.05 ± 0.20 μl/min whereas the RBF rate in diabetic OB mice is 2.63 ± 0.23 μl/min, which is 13% lower (*p<0.05).

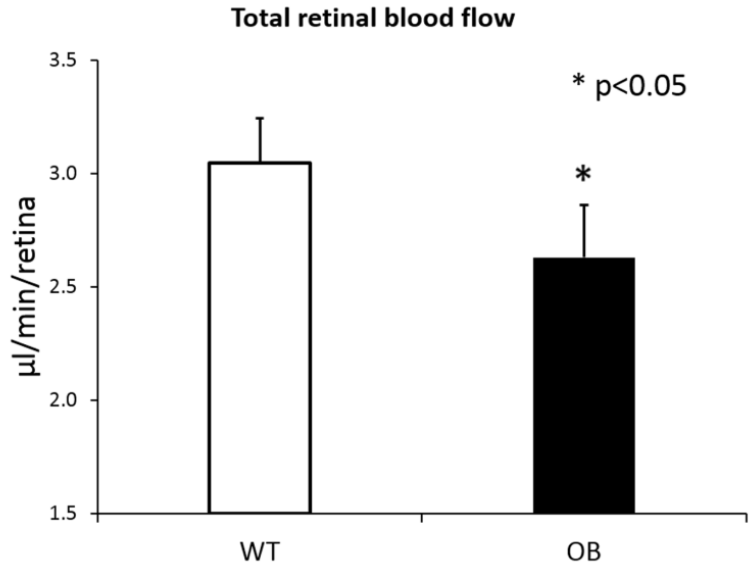

Fig. 7.6 Decrease in total retinal blood flow (RBF) in OB mouse retinas compared to WT. Mean total retinal blood flow rate (μl/min/retina) in WT control mice (N =10) and diabetic OB mice (N =10). *P < 0.05 indicates significant difference between the two groups. Data are presented as means ± SE.

7.4 Discussion

In this paper, we applied OCT and its functional modality OMAG for noninvasive 3D imaging of the murine retinal microstructure and microvasculature. The purpose was to investigate early diabetes-induced alterations in the retinal structure and microvasculature using an obese diabetic mouse model. Our results suggest that there is a significant change in both retinal thickness and total RBF rate in the diabetic OB retinas, while the retinal capillary density did not show any significant change compared to the wild-type retinas in our imaging system.

While the retinal thickness of the NFL-IPL is significantly thinner in diabetic OB mice as compared to the WT controls, the NFL thickness remains unchanged as detected by our current

OCT/OMAG system. There is reason to suspect that ganglion cells loss may responsible for the reduction in NFL-IPL thickness reduction in diabetic mice [151, 152]. Krady *et al.* reported that the spontaneous development of diabetes in $Ins2^{Akita}$ mice (a model of Type 1 diabetes) resulted a 23.4% reduction in the number of cell bodies in the GCL after 22 weeks of hyperglycemia [153]. The effect of diabetes on retinal ganglion cells has also been studied in the spontaneously diabetic KKAY strain (a model of Type 2 diabetes) where Ning *et al.* demonstrated that apoptosis of retinal ganglion cells [154] using TUNEL staining in whole retinas. Our OCT/OMAG imaging results are consistent with these findings and perhaps provide a mechanism for imaging ganglion cell layer thinning (and other potential diabetes-induced microstructural changes) over time in a non-invasive *in vivo* manner.

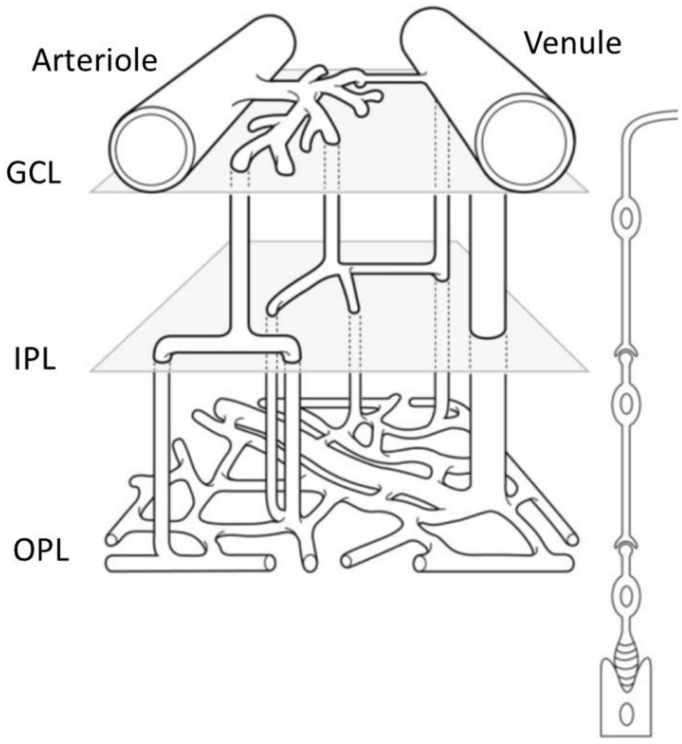

Fig. 7.7 Schematic representation of the microvessel array between an arteriovenous couple (image regenerated from [155] with permission). GCL: ganglion cell layer, IPL: inner plexiform layer, OPL: outer plexiform layer.

It has been commonly reported that three layers of microvessels are presented in the mouse retina, with predominantly precapillary arterioles in the superficial layer and postcapillary venules in the deep layer. Paque *et al.* proposed a schematic sketch of the microvessel array between an arteriovenous couple (Fig. 7.7) based on their observation from *ex vivo* confocal imaging [155]. They clearly identified the intermediate layer as asymmetric crossroads for capillary blood flow. In this paper, we confirmed this schematic of mouse retinal microvascular organization using our 3D depth-resolved OMAG imaging in living animals in their physiological state. As compared to the confocal imaging or Multiphoton microscopy of mouse retina, the biggest advantage of OMAG is its noninvasiveness and *in vivo* imaging capability. Another advantage of OMAG is its large field of view. Although we did not observe any differences in the capillary vessel organization between the WT control and diabetic OB mice in this study, we anticipate that this may be due to the fact that OB mice are still in the early stage of diabetes with no observable morphological change occurred in the capillary bed. However, a system capable of detecting retinal microvasculature changes non-invasively *in vivo* would be particularly useful for studying diabetic retinopathy in human patients. Tam et al. reported that there is disruption of the retinal parafoveal capillary network in type 2 diabetes before the onset of diabetic retinopathy by the use of adaptive optics scanning laser ophthalmoscopy [156] . As such, the OMAG system, which has been successfully applied for imaging of human retinal microvasculature, can potentially be used for screening of diabetic suspects. In addition, OMAG imaging would allow for longitudinal monitoring of progressive diabetic microvascular changes, including detection of early microaneurysms and perhaps even early detection of neovascular changes.

Measurement of the total retinal blood flow rate was achieved using the phase-resolved *en face* Doppler approach. This method has been successfully applied for pulsatile total RBF in both human and rat eye [105, 106], although in this study, we did not take into the account of the RBF pulsatility as our goal was to measure the averaged total retinal blood flow rate. By integrating the axial velocity over the vessel cross-section in the *en face* plane, both the systolic and diastolic

flow was included, thus eliminating the pulsatility effect. Finally, the total RBF described in this paper is the averages of arterial and venous flow rate, which make the measurements less reflective of motion and pulsatility artifacts.

While there was no difference in the density of the retinal capillaries, interestingly, there was a significant measurable decrease in the total retinal blood flow in the OB retinas in comparison to the WT retinas. These results are consistent with previous studies that show that there is a reduction in the retinal blood flow in diabetic rat and mouse models [157-159]. It has also been reported that retinal blood flow measured by using a Laser Doppler Velocimetry was decreased in early stage of diabetic retinopathy in patients with type 1 [160] and type 2 diabetes [161]. However, there is still controversy about whether the total retinal blood flow increases or decreases in diabetic patients. The reduction in RBF is usually seen in the earlier stages of diabetes which may result in a reduction of nutrient delivery to the retinal tissue that may contribute to the resultant development of microvascular changes. But the increases in retinal blood flow are usually seen in the later stages of diabetic retinopathy development [157]. OMAG's capability in performing long term *in vivo* monitoring of retinal blood flow changes may help better elucidate these pathological changes.

A recent study by Harris *et al.* [150] reported similar findings where they found that diabetes-induced retinal blood flow is decreased in the STZ-induced diabetic rat, while there was no reduction in linear capillary density. By infusing fluorescently-labeled RBCs into the mouse retina, they counted the number of fluorescent RBCs in the intermediate and deep capillary layers versus the RBCs in the superficial branches of the primary arterioles, and found that in the diabetic rat, the number of fluorescent RBCs in the inner and deep capillary layers is lower than normal control. This indicates a lower fraction of the retinal blood flow passes through the inner and deep capillaries, with a higher than normal fraction of blood flowing through superficial arteriovenular pathways for diabetic rat. This explanation could be applicable to our observations in the OB diabetic mice as well. We also hypothesize that the capillary flux, i.e. the number of

blood cell flows through the capillary beds per unit time is reduced due to hyperglycaemia in diabetic mice. Hyperglycemia can increase the viscosity of blood which may in turn reduce capillary velocity as well as the blood flux. In order to validate this hypothesis, we will develop a method to measure capillary flux based on the OMAG technique.

7.5 Conclusion

In this paper, OCT/OMAG was applied to achieve noninvasive imaging of changes in retinal morphology and microvasculature of diabetic obese mice and its wide type control. The thickness from NFL to IPL was significantly thinner in OB mice ($p<0.01$). 3D depth-resolved OMAG angiography revealed the first *in vivo* tri-dimensional model of mouse retinal microcirculation. No obvious difference in the capillary vessel density for both intermediate and deep capillary layers was found between normal and obese mice. The total RBF rate was however significantly ($p<0.05$) lower in obese mice than that in WT mice. We conclude that, compared with the wild-type, there is reduction in NFL-IPL thickness and total RBF rate in the obese BTBR mice as revealed by OCT/OMAG. OMAG provides an unprecedented capability for high-resolution depth-resolved imaging of mouse retinal microvasculature which may play vital role for detecting early microvessel abnormality such as microaneurysms.

Chapter 8. RBC Flux measurement of Retina in Normal and Diabetic Mice with Optical Coherence Tomography

8. 1 Motivation

Ocular microcirculation plays an important role for maintaining a normal vision and abnormal ocular blood flow was shown to be related to many ocular diseases, such as age-related macular degeneration [162], diabetic retinopathy [163, 164], and glaucoma [54]. As we know, the capillaries are the smallest unit of the circulatory system, within which, red blood cells (RBCs) are squeezing through one by one. The capillary network directly supplies the circulatory tissue beds with oxygen and nutrition. It is critical to develop a noninvasive imaging technique to visualize the retinal capillary network and quantify the RBC characteristics for understanding and early diagnosis of ocular diseases that have a vascular component in their pathogenesis.

In particular, Diabetic retinopathy (DR) is the most common microvascular complication of diabetes and a leading cause of blindness in American adults. It is caused by changes in the blood vessels of the retina. At the early stage of DR, microaneurysms which are small areas of balloon-like swelling, occur in the retina's tiny blood vessels/capillaries [132, 165]. In chapter 7, we investigated the diabetes-induced changes in retinal microvasculature of a diabetic BTBR *ob/ob* (OB) mouse model using UHS-OMAG. The systemic blood pressure was significantly increased in OB mice but total retinal blood flow (RBF) was significantly lower in the OB mice compared with WT mice [144]. This means the retinal vascular resistance, which was calculated as (resistance=ocular perfusion pressure/flow), should be much higher in OB mice. If so, vasoconstriction, decrease in the number of vessels or capillary flow reduction would happen. However, we found that the capillary density was not significantly decreased in OB mice. The RBC flow characteristic within capillary would be critical for resolving this issue. We assume that there should be difference in the capillary flux (i.e. the number of RBC flow through

the capillary per unit time) between OB and WT mice. In order to validate our assumption, we propose to measure the capillary flux within rodent retina noninvasively using OCT.

The ultra-high sensitivity of the UHS-OMAG enables us to detect the slow capillary flow down to 4μm/s [29] and it has been demonstrated for imaging capillary network in both human [166] and rodent retinas [72, 137]. This advantage is preferable for visualization of capillaries. However, it can be a problem for quantitative evaluation of capillary flow, especially the RBC characteristics, because small change in the capillary RBC flux or RBC speed couldn't be revealed from the angiography.

Recently, Lee et al. found out the fluctuating OCT signal has been shown to be associated with the RBC passing through the capillary in the mouse brain by using a repeated B-scan mod [167]. Ren et al. also applied OCT to measure the red blood cell velocities of cerebrovascular networks by detecting the Doppler phase transients induced by the passage of RBCs through the capillary [168]. However, both of these works have been done on cerebrovascular network, and no work has yet been done on retinal capillary flux measurement using OCT. More importantly, they were both conducted on normal animals, there is still demanding to test the possibility on diseased animal models.

Here, we propose to utilize a fast speed spectral-domain OCT imaging system to perform measurement of RBC flux within multiple capillary of retina at the same cross-section. The RBC flux of capillaries within retina of both OB mice and WT mice will be measured and statistically compared to validate our assumption.

8.2 System setup, data acquisition and image processing

All the system setup and animal preparation details have been presented in Chapter 7. Please go back to chapter 7 for more details. The only difference is in the homebuilt spectrometer. In this work, we updated the system to utilize a higher speed CMOS line scan camera (Basler Sprint spL4096-140 km). This ultra-fast CMOS camera has 10 μm square pixels in two rows and 4096 pixels in width. In order to increase the camera speed, only 896 pixels were illuminated with

vertical binning for the two rows. The camera was read at an exposure time of 4.2 μs which provided an ultra-fast line scan rate of 240 kHz.

For the data acquisition, we first implemented an UHS-OMAG scanning protocol [80] as shown in Fig.8.1 (A) to acquire data volumes for generating 3D angiography of retina. The beam spot of sample arm was raster scanned by x-y Galvo-mirrors to capture 1600 B-frames (400 cross-sections with 4 repeated B-frames for each cross-section) with 512 A-lines in each B-frame covering an area of ~ 1.5x1.5 mm^2 centered around the optic nerve head (ONH). The frame rate is 360 fps and the whole 3D data volume takes ~4.4 seconds. Then, on a cross-sectional plane, 2000 repeated B-scans (using 256 A-lines per B-frame and a frame rate of 720 fps) were consequently captured with the slower scanner stable (Fig.8.1 B). This M-B mode scanning produce a three-dimensional data cubes of the OCT intensity $I(z,x,t)$ and the whole scanning was completed in ~2.8 seconds. The time gap between two subsequent B-frames was Δt =1.39ms.

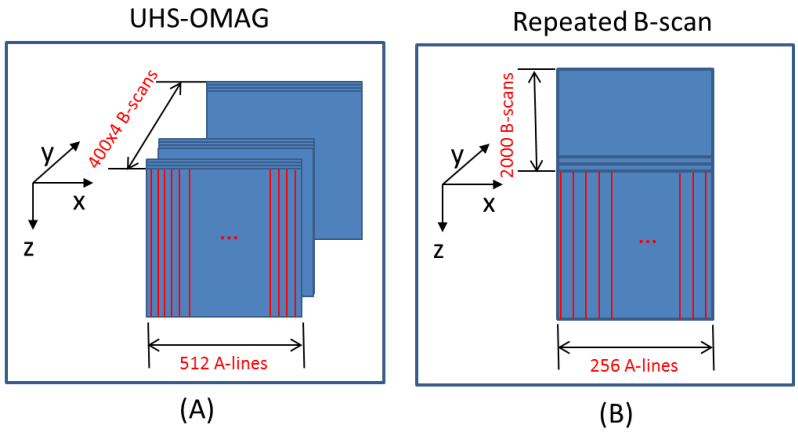

Fig. 8.1 Schematics of the scanning protocols for data acquisition. (A) UHS-OMAG scanning protocol for 3D angiography. (B) Repeated B-scan protocol for capillary flux measurement.

3D angiograms of the mouse retina were reconstructed from the 3D data volumes by applying UHS-OMAG algorithm which extracts the moving blood flow signal out of the static background tissue. The principle of UHS-OMAG algorithm is to compare the four adjacent frames captured at the same cross-section which has a long enough time interval (in this case, 2.78ms with 360 fps B-frame rate). The algorithms runs by simply subtracting the phase compensated complex signal

between subsequent B-frames (totally 4 B-frames) obtained at the same cross-section and then averaged to increase the SNR [72]. Fig.8.2A shows a typical depth color-coded projection view of the retinal microvasculature within normal mouse retina. The retinal microvasculature within three different layers (Fig.8.2 B-D), nerve fiber layer/ganglion cell layer (NFL/GCL), inner plexiform layer (IPL) and outer plexiform layer (OPL) could also been obtained after applying segmentation on the images. For 2D repeated B-scans, captured at the white line in Fig.8.2A, similar processing could be done to obtain flow only image (Fig.8.2 E). The flow image at the same cross-section was plotted along the time (Fig.8.2 F), from which, we can observe fluctuations in the intensity of capillaries due to the passage of RBCs through the capillary.

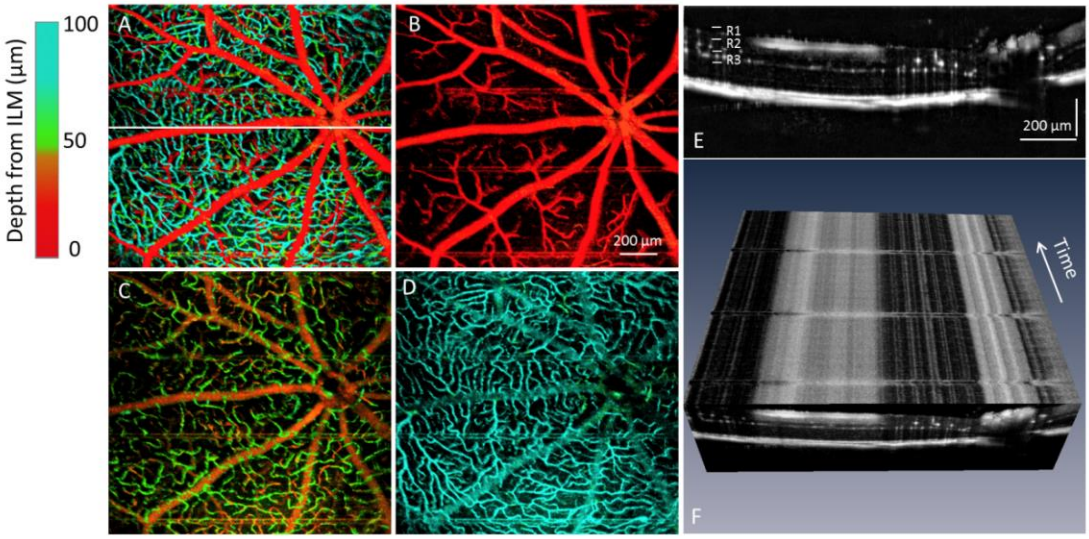

Fig. 8.2 (A) Depth-resolved angiography of moue retina. (B-D) Microvasculature within three different layers of retina after segmentation, where R1, R2 and R3 represent NFL/GCL, IPL, and OPL, respectively. (E) Cross-sectional blood flow image located at the white line in A. (F) Blood vessel through time obtained with repeated B-scans. The horizontal line artifacts are caused by animal breathing.

For the 2D repeated B-scans, we processed them using the intensity based subtraction UHS-OMAG algorithm to obtain the cross-sectional flow image. This intensity based subtraction was done on adjacent B-scans using the following equation:

$$I'(z,x,t) = \frac{d\,I(z,x,t)}{dt} = I(z,x,t+\Delta t) - I(z,x,t) \quad (1)$$

where $I(z,x,t)$ is the intensity at time point t and $I(z,x,t+\Delta t)$ is the intensity of next frame.

In order to perform multiple capillary flux measurement automatically, we need to isolate all the capillaries in the cross-section. Fig.8.3 shows the flowchart for isolating the capillaries at the cross-section. Twenty consequent B-frame flow images at the same cross-section were first averaged to obtain high contrast cross-sectional flow image (Fig.8.3 A). This image was then binarized with an automatic determined threshold (Fig.8.3 B) and each of the isolated vessel/capillary was labeled with specific number and color (Fig.8.3 C). Based on the number of pixels each vessel/capillary occupied, the big vessels were removed to obtain the capillary only cross-sectional flow image (Fig.8.3 D). In this cross-section, 40 capillaries $(cap_i,\ i= 1,\ 2...40)$ were identified and labeled with different colors (Fig.8.3 E). The capillary flux for each of them will be calculated as described below.

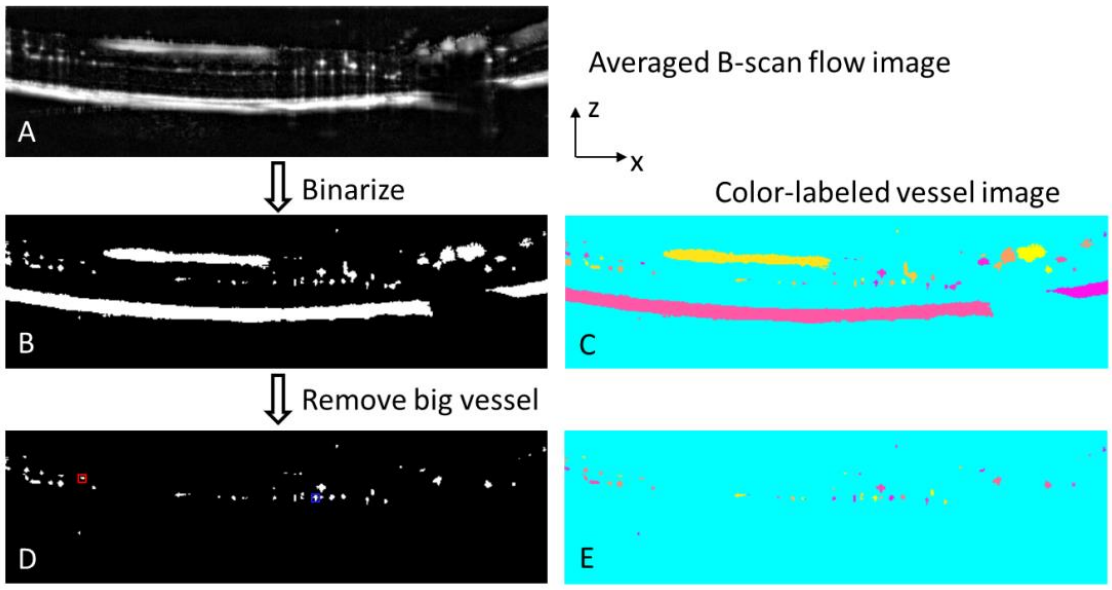

Fig. 8.3 Flowchart for automatic isolation of the capillaries at one cross-section. (A) Averaged cross-sectional blood flow image. (B) Binary image and (C) corresponding color-labeled vessel image. (D) Capillary only flow image after removing the big vessels and (D) its corresponding color-labeled capillary image.

8.3 Capillary Flux calculation

For each identified capillary cap_i, the UHS-OMAG flow signal intensity at each time point was obtained as averaged value for all the voxels within the capillary. This process was repeated for all B-frames to obtain the intensity profile $I(cap_i,t)$ throughout the whole repeated scanning time.

$$I(cap_i, t) = \sum_{voxels\ with\ capi} I'(z, x, t) \quad (2)$$

Fig.8.4 A-B shows two typical flow images picked out of the repeated B-scans, from which obvious signal fluctuation could be observed, especially the two typical capillaries labeled as 1 and 2. The raw OCT intensity profiles versus time at these two capillaries were plotted in Fig.8.4 C. The peaks in the time courses correspond to the RBC passages. In order to estimate the capillary flux, we applied a Gaussian fitting method as described by Lee etc. [167] to detect the peak numbers, which corresponds to the number of RBCs flow through the capillary. For each capillary intensity profile, the algorithm moves a 40-ms time window while fitting the data points within the window to a Gaussian function [167].

$$F(t) = a * \exp\left[-\frac{t^2}{2b^2}\right] + c \quad (3)$$

where -20 $ms < t < 20\ ms$ as the center time point of the window was set to be *zero*, and a, b, c are the fitting coefficients. Fitting resulted value of a and the coefficient of determination $R^2$are for each time point are used to detect the true RBC passage peaks by thresholding $a > 50\%$ and $R^2 > 0.5$. The RBC passage caused peaks were detected after applying above Gaussian fitting as shown in Fig.8.4 D. The capillary flux (RBC/s) was calculated as the number of peaks per second. The flux of the chosen two capillaries was estimated to be 69.3 RBC/s and 73.8 RBC/s, respectively. Flux map (Fig.8.4 E) of all capillaries in the cross-section could be obtained as well, from which we can see that for each single capillary the flux is different. To better evaluate the characteristics of the flux distribution, we plotted the corresponding histogram of the flux in the whole cross-section (Fig.8.4 F).

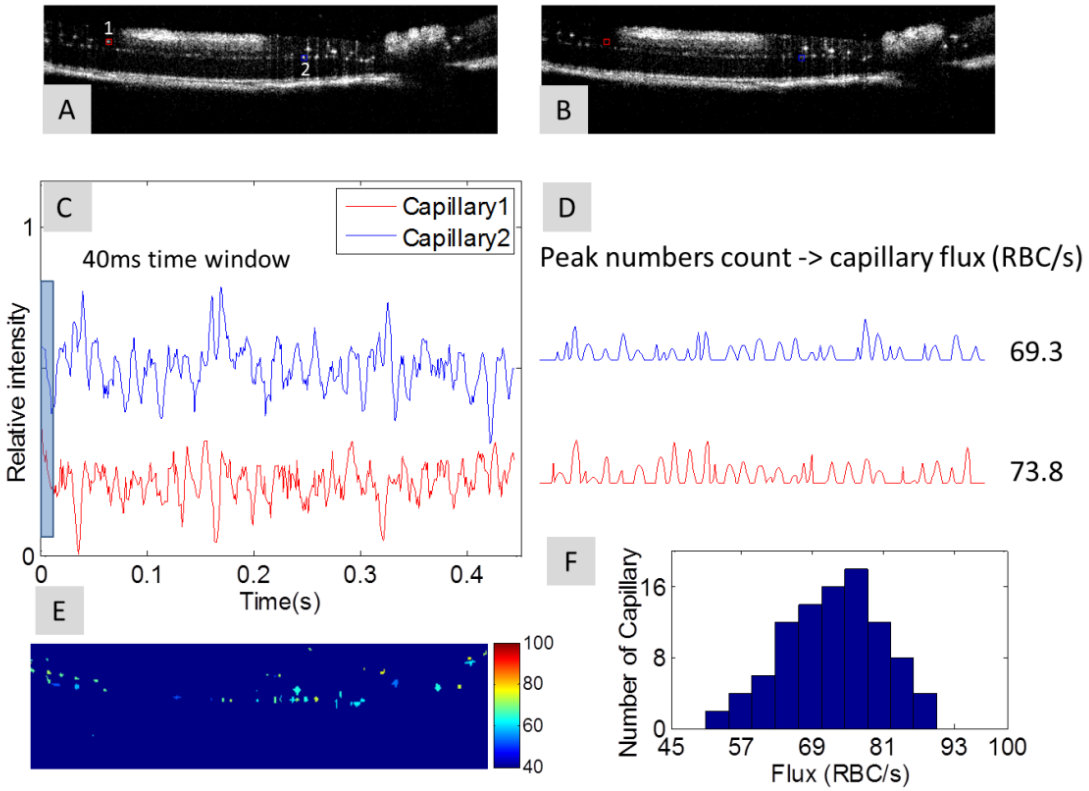

Fig. 8.4 (A-B) Two cross-sectional blood flow frames captured at different time showing the fluctuating capillary signal. (C) Smoothed intensity profile at the two capillary regions labeled as 1 and 2. (D) The intensity profile after Gaussian fitting, and capillary flux was calculated by detecting the number of peaks. (E) Cross-sectional color coded capillary flux image and (F) histogram of the flux for all capillaries in the cross-section.

One thing we need to pay attention is the chosen of Gaussian fitting time window size, which would be different for different tissue type and system setup. Here, the time window we used was 40-ms, which is determined based on the beam size and average RBC flow speed in the capillary. The beam size of our system was simulated to be ~10 μm, and the normal retinal capillary flow speeds have been estimated to be in the range of 0.4-3.0 mm/s [169, 170]. In this situation, the maximum time for the whole RBC pass through the beam would be 25-ms. Therefore, the 40-ms window size is enough to cover the whole profile of most RBCs flow through the capillary.

8. 4 Results and Discussion

BTBR *ob/ob* mice develop sever type2 diabetes and obvious hypertension. We found that they have lower total RBF but similar capillary density as compared to its WT control. One possible explanation is that the number of RBCs flow through the capillary per unit time (flux) is smaller in OB mice. Hence, in order to validate our assumption we applied the developed technique to measure the RBC flux of capillaries within retina of BTBR *ob/ob* mice as well as its WT controls.

The right eye of 6 OB mice and 6 WT mice were imaged and repeated B-scans were taken at two different cross-sections from each eye. Typical cross-sectional capillary RBC flux images for OB and WT mice are shown in Fig. 5. The histograms show the distribution of Flux in all the capillaries from the two cross-sections measured for each eye. From the histograms, we can see that the OB mice have a relative lower capillary RBC flux than WT controls.

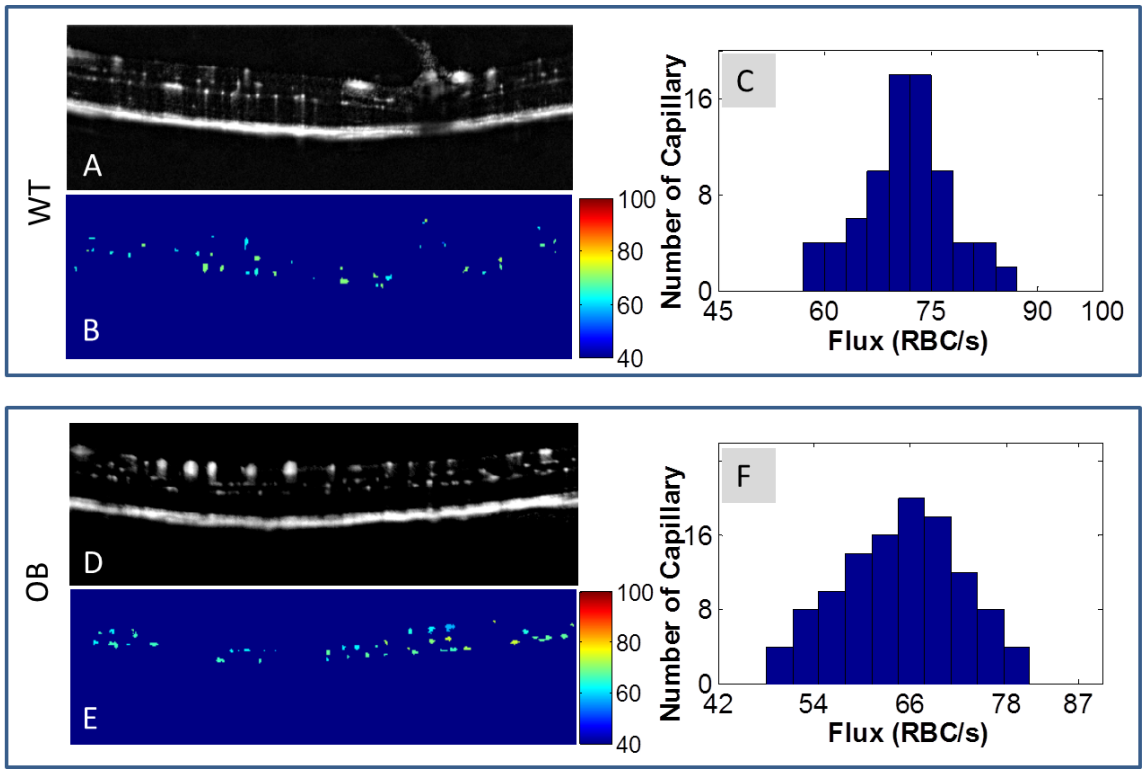

Fig. 8.5 (A-C) Cross-sectional blood flow image, capillary RBC flux image and histogram (n=80 capillaries) for WT mouse. (D-F) Cross-sectional blood flow image, capillary RBC flux image and histogram (n=94 capillaries) of the capillary flux for OB mouse.

Michel Paques et. al [155] conducted research about the structural and hemodynamic analysis of the mouse retinal microcirculation utilizing confocal imaging and Intravital microscopy. In their work, they established a tridimensional model of retinal microcirculation of mouse eye based on *ex vivo* confocal images, which has been confirmed with our *in vivo* 3D OMAG images [171]. They also calculated RBC flux in a single capillary from the number of labeled with FITC RBCs passing along a given capillary path per second, corrected by the proportion of labeled cells among all the RBCs. The RBC flux they measured is 251±96 which is much higher than what we measured here (40~100 RBC/s). The reason is because they are not directly measuring the total RBC flow through the capillary per second, but use the FITC labeled cells and then corrected by the portion which would induce big errors. Direct measurement of number of RBCs flow through the capillary based on the OCT signal can be more accurate.

In order to compare the capillary flux between OB and WT mice, we calculated the averaged capillary flux of each mouse retina as the mean value from all capillaries of the acquired two cross-sectional flow images. The average capillary flux was measured to be 76.5±4.8 RBC/s for the OB mice (N=6) and 65.4±6.6 RBC/s for the WT mice (N=6). The Statistical analysis was done to evaluate the significance of difference between OB and WT mice using a student *t*-test. Results show that the average capillary flux of OB was significantly ($p < 0.05$) lower than WT mice (Fig. 8.6).

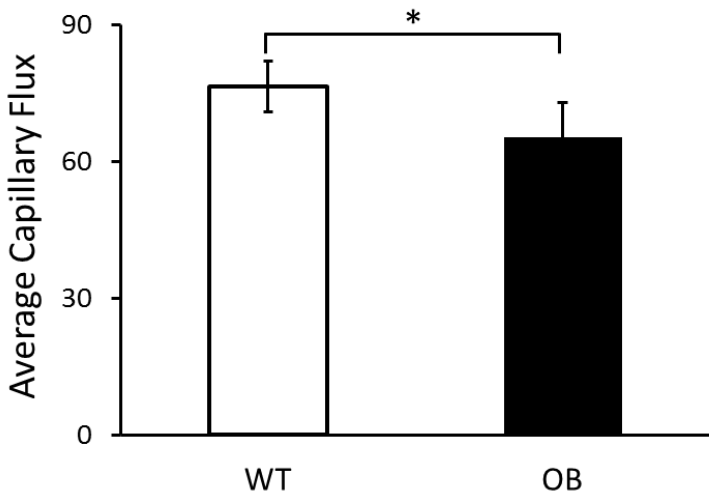

Fig. 8.6 Comparison of the averaged capillary RBC flux between BTBR OB (N=6) and WT (N=6) mice. Note, * OB group is significantly lower than WT group (Two-sample *t*-test; $p < 0.05$).

Our result explains why OB mice have higher systematic blood pressures and lower total RBF rate while the capillary vessel number wasn't less. Hyperglycemia can increase the viscosity of blood which may in turn reduce capillary velocity as well as the RBC flux. Harris et al. [150] counted the number of fluorescent RBCs in the intermediate and deep capillary layers, and found that in the STZ-induced diabetic rat, the number of fluorescent RBCs in the inner and deep capillary layers is lower than normal control. We have also demonstrated the capability of OMAG to distinguish the three different layers of microvessels: a superficial microvessel network in ganglion cell layer, an intermediate capillary network in the inner plexiform layer, and a deep microvessel network in the outer plexiform layer. In the future, we will look at the difference in flux between the three different layers of capillary network.

More importantly, the results we observed here may provide a potential important biomarker for early diagnosis of DR. Microaneurysms are the first clinically evident sign of diabetic nonproliferative eye disease and the recognition of microaneurysms can be the first step in secondary prevention of DR progression to the proliferative stage and consequent severe visual loss [172, 173]. In our work, we didn't observe obvious microaneurysm in obese mice which are

still at their early stage of diabetes. Our findings in this work indicated that the decrease of capillary flux happens even earlier than the microaneurysm during the progress of DR.

8. 5 Conclusions

In summary, we demonstrated the capability of SDOCT imaging technique for the measurement of RBC flux within multiple capillary of retina at the same time in mice. Fast frame rate (720 fps in this application) repeated B-scans at one cross-section enable us to observe fluctuation in OCT intensity as RBC passing through the capillary. The flux of each single capillary was estimated by counting the number of peaks per unit time in the signal profile after applying a Gaussian filtering algorithm. Multiple capillaries in one cross-sectional were isolated and their flux was measured automatically with this algorithm. The average capillary flux within retinas of BTBR ob/ob mice were measured to statistically lower than its WT controls. This indicates that capillary RBC flux can be an important potential maker for the early detection of diabetic retinopathy as well as other ocular diseases.

Chapter 9. Summary and future work

9.1 Summary

In this thesis, we developed a multiple-functional SDOCT system to image and quantify the microcirculation within microcirculatory tissue beds, and further apply it for pre-clinical research applications. The whole thesis was divided into two main parts. Firstly, we developed system and methods capable of volumetric and quantitative imaging of vasculature by using combined OMAG and Phase-resolved Doppler OCT for i*n vivo* study of vascular physiology (Chapter 2). We then applied the technique to investigate the impact of elevated intraocular pressure on retinal, choroidal and optic nerve head blood flow in rat eye model, which aids to the better understanding of the mechanism and development of glaucoma (Chapter 3 and Chapter 4). We also performed research for early diagnosis of Diabetic retinopathy by evaluating early diabetes-induced changes in retinal thickness and microvasculature in a type II diabetic mouse model using OCT/OMAG (Chapter 7 and Chapter 8).

Secondly, I developed an ultra-high resolution SDOCT system using broadband Supercontinuum light source to achieve ultra-high resolution imaging of microstructure and microvasculature for *in vivo* biological tissue (Chapter 5). Based on this ultra-high resolution SDOCT system, I also developed methods for label-free lymphangiography, and further achieved simultaneous label-free optical imaging of blood and lymphatic vessel. I demonstrated its capability for monitoring the blood and lymph response to wound healing on mouse ear pinna model (Chapter 6).

9.2 Future work

For the first part, in the future, the system performance could be improved to better visualize the microstructure and the capillary response within ONH during the IOP elevation. The analysis of ONH capillary and flow response to IOP elevation is mainly limited by the relative low OCT signal intensity due to the shadowing effect from the above retinal tissue and large vessels. In

order to solve this problem, we need to minimize the shadow effect from the above tissue to improve the penetration depth of light into the ONH. The approach would include increasing the light intensity, using longer wavelength light source to reduce the scattering or digital compensation of the OCT signal. We show that 1310 nm light source can penetrated deeper into the choroid and ONH than 840 nm system. However, due to the significantly increased absorption by water in the anterior and posterior chamber at wavelength higher than 1500 nm, there is a limitation to further increase the central wavelength. Hence, there is more work needs to be done to solve this problem.

We will then continue to investigate the effects of long term elevated IOP (4 hours and 8 hours) on the structures and blood perfusion within retina, choroid and ONH. Based on the results we obtained here, we found that 50 mmHg IOP doesn't cause significant reduction of blood flow and ischemia to the tissue. In the future study, the IOP will be elevated to be 50 mmHg and stay there for 4 hours and 8 hours to investigate its effect on microstructure, capillary bed filling and retinal blood flow.

Since we demonstrated the capability OMAG/OCT technique for early detection of retinal thickness and vascular changes on diabetic mouse model, we can further apply it to investigate the retinal thickness and vascular changes in human diabetic patient with the aim for early screening of diabetic retinopathy noninvasively.

For the second part, the future work would be focused on further improvement of the system resolution and processing algorithm to achieve better quality for *in vivo* label-free microangiography and lymphangiography. We will then try to apply the technique to study the microenvironment of tumor and further apply it for metastatic cancer research. The tumor growth is usually accompanied by the vessel angiogenesis. Metastatic cancer is a cancer that has spread from the part of the body where it started (the primary site) to other parts of the body. When cancer cells break away from a tumor, they can travel to other areas of the body through the bloodstream or the lymph system. Hence, a label-free lymphangiography method we developed in

this thesis along with cancer cell labeling and imaging technique will be useful for the evaluation of metastatic cancer development and treatment.

Finally, the oxygenation level is one of the important parameter of microcirculatory tissue as well. One main future work for the development of a multi-functional OCT system will include adding the spectroscopic analysis to image the oxygen saturation of the vasculature and tissue beds. As OCT utilizes a broadband light source for imaging, we can take advantage of the spectroscopic information of the broadband wavelength. We can tune the central wavelength of OCT light source to be 805 nm (equal absorption coefficient for deoxygenated hemoglobin and oxygenated hemoglobin), which can be achieved by using a tunable femtosecond laser and comparing the difference in OCT intensity from wavelength smaller than 805 nm and larger than 805 nm.

Bibliography

1. Fung, Y.C. and B.W. Zweifach, *Microcirculation - Mechanics of Blood Flow in Capillaries.* Annual Review of Fluid Mechanics, 1971. **3**: p. 189-&.
2. Dunn, A.K., et al., *Introduction: feature issue on In Vivo Microcirculation Imaging.* Biomedical Optics Express, 2011. **2**(7): p. 1861-1863.
3. Wilt, B.A., et al., *Advances in Light Microscopy for Neuroscience.* Annual Review of Neuroscience, 2009. **32**: p. 435-506.
4. Grinvald, A., et al., *Functional Architecture of Cortex Revealed by Optical Imaging of Intrinsic Signals.* Nature, 1986. **324**(6095): p. 361-364.
5. Dirnagl, U., et al., *Continuous Measurement of Cerebral Cortical Blood-Flow by Laser-Doppler Flowmetry in a Rat Stroke Model.* Journal of Cerebral Blood Flow and Metabolism, 1989. **9**(5): p. 589-596.
6. Dunn, A.K., et al., *Dynamic imaging of cerebral blood flow using laser speckle.* Journal of Cerebral Blood Flow and Metabolism, 2001. **21**(3): p. 195-201.
7. Villringer, A. and B. Chance, *Non-invasive optical spectroscopy and imaging of human brain function.* Trends in Neurosciences, 1997. **20**(10): p. 435-442.
8. Denk, W., J.H. Strickler, and W.W. Webb, *2-Photon Laser Scanning Fluorescence Microscopy.* Science, 1990. **248**(4951): p. 73-76.
9. Huang, D., et al., *Optical coherence tomography.* Science, 1991. **254**(5035): p. 1178-81.
10. de Boer, J.F., et al., *Improved signal-to-noise ratio in spectral-domain compared with time-domain optical coherence tomography.* Opt Lett, 2003. **28**(21): p. 2067-9.
11. Choma, M.A., et al., *Sensitivity advantage of swept source and Fourier domain optical coherence tomography.* Optics Express, 2003. **11**(18): p. 2183-2189.
12. Swanson, E.A., et al., *High-Speed Optical Coherence Domain Reflectometry.* Optics Letters, 1992. **17**(2): p. 151-153.
13. Fercher, A.F., et al., *Optical coherence tomography - principles and applications.* Reports on Progress in Physics, 2003. **66**(2): p. 239-303.
14. Hu, Z.L., Y.S. Pan, and A.M. Rollins, *Analytical model of spectrometer-based two-beam spectral interferometry.* Applied Optics, 2007. **46**(35): p. 8499-8505.
15. Rosamond, W., et al., *Heart disease and stroke statistics--2008 update: a report from the American Heart Association Statistics Committee and Stroke Statistics Subcommittee.* Circulation, 2008. **117**(4): p. e25-146.
16. Leitgeb, R., C. Hitzenberger, and A. Fercher, *Performance of fourier domain vs. time domain optical coherence tomography.* Opt Express, 2003. **11**(8): p. 889-94.
17. Chen, Z., et al., *Noninvasive imaging of in vivo blood flow velocity using optical Doppler tomography.* Opt Lett, 1997. **22**(14): p. 1119-21.

18. Zhao, Y., et al., *Real-time phase-resolved functional optical coherence tomography by use of optical Hilbert transformation.* Opt Lett, 2002. **27**(2): p. 98-100.
19. Zhao, Y.H., et al., *Doppler standard deviation imaging for clinical monitoring of in vivo human skin blood flow.* Optics Letters, 2000. **25**(18): p. 1358-1360.
20. Makita, S., et al., *Optical coherence angiography.* Opt Express, 2006. **14**(17): p. 7821-40.
21. Wang, R.K., et al., *Three dimensional optical angiography.* Optics Express, 2007. **15**(7): p. 4083-4097.
22. Wang, R.K. and S. Hurst, *Mapping of cerebro-vascular blood perfusion in mice with skin and skull intact by Optical Micro-AngioGraphy at 1.3 mum wavelength.* Opt Express, 2007. **15**(18): p. 11402-12.
23. An, L. and R.K. Wang, *In vivo volumetric imaging of vascular perfusion within human retina and choroids with optical micro-angiography.* Opt Express, 2008. **16**(15): p. 11438-52.
24. Wang, R.K. and L. An, *Doppler optical micro-angiography for volumetric imaging of vascular perfusion in vivo.* Opt Express, 2009. **17**(11): p. 8926-40.
25. Alitalo, K., T. Tammela, and T.V. Petrova, *Lymphangiogenesis in development and human disease.* Nature, 2005. **438**(7070): p. 946-53.
26. Pepper, M.S., *Lymphangiogenesis and tumor metastasis: Myth or reality?* Clinical Cancer Research, 2001. **7**(3): p. 462-468.
27. Zhang, F., et al., *Preclinical Lymphatic Imaging.* Molecular Imaging and Biology, 2011. **13**(4): p. 599-612.
28. Kim, C., et al., *Sentinel Lymph Nodes and Lymphatic Vessels: Noninvasive Dual-Modality in Vivo Mapping by Using Indocyanine Green in Rats-Volumetric Spectroscopic Photoacoustic Imaging and Planar Fluorescence Imaging.* Radiology, 2010. **255**(2): p. 442-450.
29. An, L., J. Qin, and R.K. Wang, *Ultrahigh sensitive optical microangiography for in vivo imaging of microcirculations within human skin tissue beds.* Opt Express, 2010. **18**(8): p. 8220-8.
30. Wang, R.K., et al., *Depth-resolved imaging of capillary networks in retina and choroid using ultrahigh sensitive optical microangiography.* Opt Lett, 2010. **35**(9): p. 1467-9.
31. Jia, Y., L. An, and R. Wang, *Label-free and highly sensitive optical imaging of detailed microcirculation within meninges and cortex in mice with the cranium left intact.* Journal of Biomedical Optics, 2010. **15**: p. 030510.
32. Jung, Y., Z. Zhi, and R. Wang, *Three-dimensional optical imaging of microvascular networks within intact lymph node in vivo.* Journal of Biomedical Optics, 2010. **15**(5): p. 0501.
33. Fingler, J., et al., *Volumetric microvascular imaging of human retina using optical coherence tomography with a novel motion contrast technique.* Optics Express, 2009. **17**(24): p. 22190-22200.
34. Mariampillai, A., et al., *Optimized speckle variance OCT imaging of microvasculature.* Opt Lett, 2010. **35**(8): p. 1257-9.

35. Kim, D.Y., et al., *In vivo volumetric imaging of human retinal circulation with phase-variance optical coherence tomography.* Biomed Opt Express, 2011. **2**(6): p. 1504-13.
36. Fingler, J., et al., *Mobility and transverse flow visualization using phase variance contrast with spectral domain optical coherence tomography.* Opt Express, 2007. **15**(20): p. 12636-53.
37. Liu, G., et al., *Intensity-based modified Doppler variance algorithm: application to phase instable and phase stable optical coherence tomography systems.* Opt Express, 2011. **19**(12): p. 11429-40.
38. Vakoc, B.J., et al., *Three-dimensional microscopy of the tumor microenvironment in vivo using optical frequency domain imaging.* Nature Medicine, 2009. **15**(10): p. 1219-U151.
39. Schmoll, T., C. Kolbitsch, and R.A. Leitgeb, *Ultra-high-speed volumetric tomography of human retinal blood flow.* Opt Express, 2009. **17**(5): p. 4166-76.
40. Zotter, S., et al., *Visualization of microvasculature by dual-beam phase-resolved Doppler optical coherence tomography.* Opt Express, 2011. **19**(2): p. 1217-27.
41. Mariampillai, A., et al., *Speckle variance detection of microvasculature using swept-source optical coherence tomography.* Opt Lett, 2008. **33**(13): p. 1530-2.
42. Enfield, J., E. Jonathan, and M. Leahy, *In vivo imaging of the microcirculation of the volar forearm using correlation mapping optical coherence tomography (cmOCT).* Biomedical Optics Express, 2011. **2**(5): p. 1184-1193.
43. Jia, Y., et al., *Split-spectrum amplitude-decorrelation angiography with optical coherence tomography.* Opt Express, 2012. **20**(4): p. 4710-25.
44. Szkulmowski, M., et al., *Flow velocity estimation using joint Spectral and Time Domain Optical Coherence Tomography.* Optics Express, 2008. **16**(9): p. 6008-6025.
45. Tao, Y.K., A.M. Davis, and J.A. Izatt, *Single-pass volumetric bidirectional blood flow imaging spectral domain optical coherence tomography using a modified Hilbert transform.* Opt Express, 2008. **16**(16): p. 12350-61.
46. Srinivasan, V.J., et al., *Rapid volumetric angiography of cortical microvasculature with optical coherence tomography.* Opt Lett, 2010. **35**(1): p. 43-5.
47. Srinivasan, V.J., et al., *Quantitative cerebral blood flow with optical coherence tomography.* Opt Express, 2010. **18**(3): p. 2477-94.
48. Grulkowski, I., et al., *Scanning protocols dedicated to smart velocity ranging in spectral OCT.* Opt Express, 2009. **17**(26): p. 23736-54.
49. Piao, D., L.L. Otis, and Q. Zhu, *Doppler angle and flow velocity mapping by combined Doppler shift and Doppler bandwidth measurements in optical Doppler tomography.* Opt Lett, 2003. **28**(13): p. 1120-2.
50. Pedersen, C.J., et al., *Measurement of absolute flow velocity vector using dual-angle, delay-encoded Doppler optical coherence tomography.* Opt Lett, 2007. **32**(5): p. 506-8.

51. Ma, Z., et al., *Measurement of absolute blood flow velocity in outflow tract of HH18 chicken embryo based on 4D reconstruction using spectral domain optical coherence tomography.* Biomedical Optics Express, 2010. **1**(3): p. 798-811.
52. Wang, Y., et al., *In vivo total retinal blood flow measurement by Fourier domain Doppler optical coherence tomography.* J Biomed Opt, 2007. **12**(4): p. 041215.
53. White, B., et al., *In vivo dynamic human retinal blood flow imaging using ultra-high-speed spectral domain optical coherence tomography.* Opt Express, 2003. **11**(25): p. 3490-7.
54. Flammer, J., et al., *The impact of ocular blood flow in glaucoma.* Prog Retin Eye Res, 2002. **21**(4): p. 359-93.
55. Grieshaber, M.C. and J. Flammer, *Blood flow in glaucoma.* Curr Opin Ophthalmol, 2005. **16**(2): p. 79-83.
56. Grunwald, J.E., et al., *Optic nerve and choroidal circulation in glaucoma.* Invest Ophthalmol Vis Sci, 1998. **39**(12): p. 2329-36.
57. Riva, C.E., J.E. Grunwald, and B.L. Petrig, *Autoregulation of human retinal blood flow. An investigation with laser Doppler velocimetry.* Invest Ophthalmol Vis Sci, 1986. **27**(12): p. 1706-12.
58. Brein, K.R. and C.E. Riva, *Laser Doppler velocimetry measurement of pulsatile blood flow in capillary tubes.* Microvasc Res, 1982. **24**(1): p. 114-8.
59. Riva, C.E., et al., *Blood velocity and volumetric flow rate in human retinal vessels.* Invest Ophthalmol Vis Sci, 1985. **26**(8): p. 1124-32.
60. Binaghi, F., F. Cannas, and F. Pitzus, *[Laser Doppler flowmetry. Principles and clinical applications in vascular acro-syndromes]*. Minerva Med, 1988. **79**(10): p. 831-8.
61. Riva, C.E., *Basic principles of laser Doppler flowmetry and application to the ocular circulation.* Int Ophthalmol, 2001. **23**(4-6): p. 183-9.
62. He, Z., et al., *Blood pressure modifies retinal susceptibility to intraocular pressure elevation.* PLoS One, 2012. **7**(2): p. e31104.
63. Harris, A., et al., *Laser Doppler flowmetry measurement of changes in human optic nerve head blood flow in response to blood gas perturbations.* J Glaucoma, 1996. **5**(4): p. 258-65.
64. Riva, C.E., et al., *Laser Doppler flowmetry in the optic nerve.* Exp Eye Res, 1992. **55**(3): p. 499-506.
65. Yaoeda, K., et al., *Measurement of microcirculation in the optic nerve head by laser speckle flowgraphy and scanning laser Doppler flowmetry.* Am J Ophthalmol, 2000. **129**(6): p. 734-9.
66. Petrig, B.L., C.E. Riva, and S.S. Hayreh, *Laser Doppler flowmetry and optic nerve head blood flow.* Am J Ophthalmol, 1999. **127**(4): p. 413-25.
67. Chauhan, D.S. and J. Marshall, *The interpretation of optical coherence tomography images of the retina.* Invest Ophthalmol Vis Sci, 1999. **40**(10): p. 2332-42.

68. van Velthoven, M.E., et al., *Recent developments in optical coherence tomography for imaging the retina.* Prog Retin Eye Res, 2007. **26**(1): p. 57-77.
69. Leitgeb, R., et al., *Real-time assessment of retinal blood flow with ultrafast acquisition by color Doppler Fourier domain optical coherence tomography.* Opt Express, 2003. **11**(23): p. 3116-21.
70. Wang, Y., et al., *Pilot study of optical coherence tomography measurement of retinal blood flow in retinal and optic nerve diseases.* Invest Ophthalmol Vis Sci, 2011. **52**(2): p. 840-5.
71. Zhao, Y., et al., *Phase-resolved optical coherence tomography and optical Doppler tomography for imaging blood flow in human skin with fast scanning speed and high velocity sensitivity.* Opt Lett, 2000. **25**(2): p. 114-6.
72. Zhi, Z., et al., *Volumetric and quantitative imaging of retinal blood flow in rats with optical microangiography.* Biomed Opt Express, 2011. **2**(3): p. 579-91.
73. Varma, R., et al., *An assessment of the health and economic burdens of glaucoma.* Am J Ophthalmol, 2011. **152**(4): p. 515-22.
74. Roberts, M.D., et al., *Changes in the biomechanical response of the optic nerve head in early experimental glaucoma.* Invest Ophthalmol Vis Sci, 2010. **51**(11): p. 5675-84.
75. Morrison, J.C., W.O. Cepurna Ying Guo, and E.C. Johnson, *Pathophysiology of human glaucomatous optic nerve damage: Insights from rodent models of glaucoma.* Exp Eye Res, 2010.
76. Pang, I.H. and A.F. Clark, *Rodent models for glaucoma retinopathy and optic neuropathy.* J Glaucoma, 2007. **16**(5): p. 483-505.
77. Guo, Y., et al., *Early gene expression changes in the retinal ganglion cell layer of a rat glaucoma model.* Invest Ophthalmol Vis Sci, 2011. **52**(3): p. 1460-73.
78. Johnson, E.C., et al., *Cell proliferation and interleukin-6-type cytokine signaling are implicated by gene expression responses in early optic nerve head injury in rat glaucoma.* Invest Ophthalmol Vis Sci, 2011. **52**(1): p. 504-18.
79. Liang, Y., et al., *Impact of systemic blood pressure on the relationship between intraocular pressure and blood flow in the optic nerve head of nonhuman primates.* Invest Ophthalmol Vis Sci, 2009. **50**(5): p. 2154-60.
80. Zhi, Z., et al., *Highly sensitive imaging of renal microcirculation in vivo using ultrahigh sensitive optical microangiography.* Biomed Opt Express, 2011. **2**(5): p. 1059-68.
81. Fukuchi, T., et al., *Optical coherence tomography (OCT) findings in normal retina and laser-induced choroidal neovascularization in rats.* Graefes Arch Clin Exp Ophthalmol, 2001. **239**(1): p. 41-6.
82. Srinivasan, V.J., et al., *Rapid volumetric angiography of cortical microvasculature with optical coherence tomography.* Opt Lett. **35**(1): p. 43-5.
83. Geijer, C. and A. Bill, *Effects of raised intraocular pressure on retinal, prelaminar, laminar, and retrolaminar optic nerve blood flow in monkeys.* Invest Ophthalmol Vis Sci, 1979. **18**(10): p. 1030-42.

84. He, Z., et al., *The role of blood pressure in glaucoma.* Clin Exp Optom, 2011. **94**(2): p. 133-49.
85. Jia, Y., P. Li, and R.K. Wang, *Optical microangiography provides an ability to monitor responses of cerebral microcirculation to hypoxia and hyperoxia in mice.* J Biomed Opt, 2011. **16**(9): p. 096019.
86. Jia, Y., et al., *Responses of peripheral blood flow to acute hypoxia and hyperoxia as measured by optical microangiography.* PLoS One, 2011. **6**(10): p. e26802.
87. Morrison, J.C., E. Johnson, and W.O. Cepurna, *Rat models for glaucoma research.* Prog Brain Res, 2008. **173**: p. 285-301.
88. Fortune, B., et al., *Deformation of the rodent optic nerve head and peripapillary structures during acute intraocular pressure elevation.* Invest Ophthalmol Vis Sci, 2011. **52**(9): p. 6651-61.
89. Morrison, J.C., et al., *Microvasculature of the rat optic nerve head.* Invest Ophthalmol Vis Sci, 1999. **40**(8): p. 1702-9.
90. Dai, C., et al., *Structural basis of glaucoma: the fortified astrocytes of the optic nerve head are the target of raised intraocular pressure.* Glia, 2012. **60**(1): p. 13-28.
91. M. Pazos, et al., *Radial Optic Nerve Expansion Within the Expanding Scleral Canal in the Hypertonic Saline Rat Early Experimental Glaucoma (EEG) Model.* Invest Ophthalmol Vis Sci, 2010. **51**(E-abstract): p. 4806.
92. Bui, B.V., et al., *The gradient of retinal functional changes during acute intraocular pressure elevation.* Invest Ophthalmol Vis Sci, 2005. **46**(1): p. 202-13.
93. Fizanne, L., et al., *Effect of isoflurane on skin-pressure-induced vasodilation.* J Vasc Res, 2003. **40**(4): p. 416-22.
94. Leoni, R.F., et al., *Magnetic resonance imaging quantification of regional cerebral blood flow and cerebrovascular reactivity to carbon dioxide in normotensive and hypertensive rats.* Neuroimage, 2011. **58**(1): p. 75-81.
95. Seyde, W.C. and D.E. Longnecker, *Cerebral oxygen tension in rats during deliberate hypotension with sodium nitroprusside, 2-chloroadenosine, or deep isoflurane anesthesia.* Anesthesiology, 1986. **64**(4): p. 480-5.
96. Z. He, A.J. Vingrys, and B.V. Bui, *Characterization of Blood Flow Autoregulation in Rat Eyes*. Invest Ophthalmol Vis Sci, 2010. **51**(E-abstract): p. 2686.
97. Weigert, G., et al., *Effects of moderate changes in intraocular pressure on ocular hemodynamics in patients with primary open-angle glaucoma and healthy controls.* Ophthalmology, 2005. **112**(8): p. 1337-42.
98. Pillunat, L.E., et al., *Autoregulation of human optic nerve head circulation in response to increased intraocular pressure.* Exp Eye Res, 1997. **64**(5): p. 737-44.
99. Riva, C.E., S.D. Cranstoun, and B.L. Petrig, *Effect of decreased ocular perfusion pressure on blood flow and the flicker-induced flow response in the cat optic nerve head.* Microvasc Res, 1996. **52**(3): p. 258-69.

100. Sossi, N. and D.R. Anderson, *Effect of elevated intraocular pressure on blood flow. Occurrence in cat optic nerve head studied with iodoantipyrine I 125.* Arch Ophthalmol, 1983. **101**(1): p. 98-101.
101. Alm, A. and A. Bill, *The oxygen supply to the retina. II. Effects of high intraocular pressure and of increased arterial carbon dioxide tension on uveal and retinal blood flow in cats. A study with radioactively labelled microspheres including flow determinations in brain and some other tissues.* Acta Physiol Scand, 1972. **84**(3): p. 306-19.
102. Kiel, J.W. and A.P. Shepherd, *Autoregulation of choroidal blood flow in the rabbit.* Invest Ophthalmol Vis Sci, 1992. **33**(8): p. 2399-410.
103. Polska, E., et al., *Regulation of choroidal blood flow during combined changes in intraocular pressure and arterial blood pressure.* Invest Ophthalmol Vis Sci, 2007. **48**(8): p. 3768-74.
104. Cuthbertson, R.A. and T.E. Mandel, *Anatomy of the Mouse Retina - Endothelial-Cell Pericyte Ratio and Capillary Distribution.* Investigative Ophthalmology & Visual Science, 1986. **27**(11): p. 1659-1664.
105. Baumann, B., et al., *Total retinal blood flow measurement with ultrahigh speed swept source/Fourier domain OCT.* Biomed Opt Express, 2011. **2**(6): p. 1539-52.
106. Choi, W., et al., *Measurement of pulsatile total blood flow in the human and rat retina with ultrahigh speed spectral/Fourier domain OCT.* Biomed Opt Express, 2012. **3**(5): p. 1047-61.
107. Ko, T., et al., *Ultrahigh resolution optical coherence tomography imaging with a broadband superluminescent diode light source.* Opt. Express, 2004. **12**(10): p. 2112-2119.
108. Drexler, W., et al., *In vivo ultrahigh-resolution optical coherence tomography.* Opt. Lett., 1999. **24**(17): p. 1221-1223.
109. Leitgeb, R., et al., *Ultrahigh resolution Fourier domain optical coherence tomography.* Opt. Express, 2004. **12**(10): p. 2156-2165.
110. Povazay, B., et al., *Submicrometer axial resolution optical coherence tomography.* Opt Lett, 2002. **27**(20): p. 1800-2.
111. Kray, S., et al., *High-resolution simultaneous dual-band spectral domain optical coherence tomography.* Opt Lett, 2009. **34**(13): p. 1970-2.
112. Spoler, F., et al., *Simultaneous dual-band ultra-high resolution optical coherence tomography.* Opt Express, 2007. **15**(17): p. 10832-41.
113. Cimalla, P., et al., *Simultaneous dual-band optical coherence tomography in the spectral domain for high resolution in vivo imaging.* Opt Express, 2009. **17**(22): p. 19486-500.
114. Yousefi, S., Z. Zhi, and R. Wang, *Eigendecomposition-Based Clutter Filtering Technique for Optical Micro-Angiography.* IEEE Trans Biomed Eng, 2011.
115. Grotte, G., *Discovery of the Lymphatic Circulation - Introduction.* Acta Physiologica Scandinavica, 1979: p. 9-10.
116. Shayan, R., M.G. Achen, and S.A. Stacker, *Lymphatic vessels in cancer metastasis: bridging the gaps.* Carcinogenesis, 2006. **27**(9): p. 1729-1738.

117. Saharinen, P., et al., *Lymphatic vasculature: development, molecular regulation and role in tumor metastasis and inflammation.* Trends in Immunology, 2004. **25**(7): p. 387-395.
118. Karpanen, T. and K. Alitalo, *Lymphatic vessels as targets of tumor therapy?* Journal of Experimental Medicine, 2001. **194**(6): p. F37-F42.
119. Martinez-Corral, I., et al., *In vivo imaging of lymphatic vessels in development, wound healing, inflammation, and tumor metastasis.* Proceedings of the National Academy of Sciences of the United States of America, 2012. **109**(16): p. 6223-6228.
120. Jung, Y., Z. Zhi, and R.K. Wang, *Three-dimensional optical imaging of microvascular networks within intact lymph node in vivo.* J Biomed Opt, 2010. **15**(5): p. 050501.
121. Zhi, Z.W., et al., *Supercontinuum light source enables in vivo optical microangiography of capillary vessels within tissue beds.* Optics Letters, 2011. **36**(16): p. 3169-3171.
122. Dellinger, M., et al., *Defective remodeling and maturation of the lymphatic vasculature in Angiopoietin-2 deficient mice.* Developmental Biology, 2008. **319**(2): p. 309-320.
123. Galanzha, E.I., V.V. Tuchin, and V.P. Zharov, *In vivo integrated flow image cytometry and lymph/blood vessels dynamic microscopy.* J Biomed Opt, 2005. **10**(5): p. 054018.
124. Miller, M.J., et al., *Two-photon imaging of lymphocyte motility and antigen response in intact lymph node.* Science, 2002. **296**(5574): p. 1869-73.
125. Singer, A.J. and R.A.F. Clark, *Mechanisms of disease - Cutaneous wound healing.* New England Journal of Medicine, 1999. **341**(10): p. 738-746.
126. Logerfo, F.W. and J.D. Coffman, *Vascular and Microvascular Disease of the Foot in Diabetes - Implications for Foot Care.* New England Journal of Medicine, 1984. **311**(25): p. 1615-1619.
127. Rapp, S.R., et al., *Psoriasis causes as much disability as other major medical diseases.* Journal of the American Academy of Dermatology, 1999. **41**(3): p. 401-407.
128. Martin, P., *Wound healing - Aiming for perfect skin regeneration.* Science, 1997. **276**(5309): p. 75-81.
129. Baum, C.L. and C.J. Arpey, *Normal cutaneous wound healing: Clinical correlation with cellular and molecular events.* Dermatologic Surgery, 2005. **31**(6): p. 674-686.
130. Kerbel, R.S., *Molecular origins of cancer: Tumor angiogenesis.* New England Journal of Medicine, 2008. **358**(19): p. 2039-2049.
131. Antonetti, D.A., et al., *Diabetic retinopathy - Seeing beyond glucose-induced microvascular disease.* Diabetes, 2006. **55**(9): p. 2401-2411.
132. Cheung, N., P. Mitchell, and T.Y. Wong, *Diabetic retinopathy.* Lancet, 2010. **376**(9735): p. 124-136.
133. Ivanisevic, M. and R. Stanic, *Importance of Fluorescein Angiography in the Early Detection and Therapy of Diabetic-Retinopathy.* Ophthalmologica, 1990. **201**(1): p. 9-13.
134. Hochheim.Bf, *Angiography of Retina with Indocyanine Green.* Archives of Ophthalmology, 1971. **86**(5): p. 564-&.

135. Wang, Y., et al., *Retinal blood flow detection in diabetic patients by Doppler Fourier domain optical coherence tomography.* Opt Express, 2009. **17**(5): p. 4061-73.
136. Zhi, Z., et al., *Impact of intraocular pressure on changes of blood flow in the retina, choroid, and optic nerve head in rats investigated by optical microangiography.* Biomedical optics express, 2012. **3**(9): p. 2220-2233.
137. Zhi, Z., et al., *Optical microangiography of retina and choroid and measurement of total retinal blood flow in mice.* Biomedical optics express, 2012. **3**(11): p. 2976.
138. Robinson, R., et al., *Update on animal models of diabetic retinopathy: from molecular approaches to mice and higher mammals.* Disease Models & Mechanisms, 2012. **5**(4): p. 444-456.
139. Barber, A.J., et al., *The Ins2(Akita) mouse as a model of diabetic retinopathy.* Investigative Ophthalmology & Visual Science, 2004. **45**: p. U92-U92.
140. Feit-Leichman, R.A., et al., *Vascular damage in a mouse model of diabetic retinopathy: Relation to neuronal and glial changes.* Investigative Ophthalmology & Visual Science, 2005. **46**(11): p. 4281-4287.
141. Feit, R., et al., *Using C57BL/6J as a mouse model for diabetic retinopathy.* Investigative Ophthalmology & Visual Science, 2004. **45**: p. U93-U93.
142. Kern, T.S. and R.L. Engerman, *A mouse model of diabetic retinopathy.* Archives of Ophthalmology, 1996. **114**(8): p. 986-990.
143. Li, Q.H., et al., *Diabetic eNOS-Knockout Mice Develop Accelerated Retinopathy.* Investigative Ophthalmology & Visual Science, 2010. **51**(10): p. 5240-5246.
144. Hudkins, K.L., et al., *BTBR Ob/Ob Mutant Mice Model Progressive Diabetic Nephropathy.* Journal of the American Society of Nephrology, 2010. **21**(9): p. 1533-1542.
145. Clee, S.M. and A.D. Attie, *The genetic landscape of type 2 diabetes in mice.* Endocrine Reviews, 2007. **28**(1): p. 48-83.
146. Clee, S.M., S.T. Nadler, and A.D. Attie, *Genetic and genomic studies of the BTBR ob/ob mouse model of type 2 diabetes.* Am J Ther, 2005. **12**(6): p. 491-8.
147. Ranheim, T., et al., *Interaction between BTBR and C57BL/6J genomes produces an insulin resistance syndrome in (BTBR x C57BL/6J) F-1 mice.* Arteriosclerosis Thrombosis and Vascular Biology, 1997. **17**(11): p. 3286-3293.
148. Clee, S.M., et al., *Positional cloning of Sorcs1, a type 2 diabetes quantitative trait locus.* Nature Genetics, 2006. **38**(6): p. 688-693.
149. Srinivasan, V.J., et al., *Noninvasive volumetric Imaging and morphometry of the rodent retina with high-speed, ultrahigh-resolution optical coherence tomography.* Investigative Ophthalmology & Visual Science, 2006. **47**(12): p. 5522-5528.
150. Leskova, W., et al., *Measurement of retinal blood flow rate in diabetic rats: disparity between techniques due to redistribution of flow.* Invest Ophthalmol Vis Sci, 2013. **54**(4): p. 2992-9.

151. Kern, T.S. and A.J. Barber, *Retinal ganglion cells in diabetes.* Journal of Physiology-London, 2008. **586**(18): p. 4401-4408.
152. Martin, P.M., et al., *Death of retinal neurons in streptozotocin-induced diabetic mice.* Investigative Ophthalmology & Visual Science, 2004. **45**(9): p. 3330-3336.
153. Barber, A.J., et al., *The Ins2(Akita) mouse as a model of early retinal complications in diabetes.* Investigative Ophthalmology & Visual Science, 2005. **46**(6): p. 2210-2218.
154. Ning, X., et al., *Neuro-optic cell apoptosis and microangiopathy in KKAY mouse retina.* International Journal of Molecular Medicine, 2004. **13**(1): p. 87-92.
155. Paques, M., et al., *Structural and hemodynamic analysis of the mouse retinal microcirculation.* Investigative Ophthalmology & Visual Science, 2003. **44**(11): p. 4960-4967.
156. Tam, J., et al., *Disruption of the Retinal Parafoveal Capillary Network in Type 2 Diabetes before the Onset of Diabetic Retinopathy.* Investigative Ophthalmology & Visual Science, 2011. **52**(12): p. 9257-9266.
157. Clermont, A.C. and S.E. Bursell, *Retinal blood flow in diabetes.* Microcirculation, 2007. **14**(1): p. 49-61.
158. Bursell, S.E., et al., *Evaluating Retinal Circulation Using Video Fluorescein Angiography in Control and Diabetic Rats.* Current Eye Research, 1992. **11**(4): p. 287-295.
159. Muir, E.R., R.C. Renteria, and T.Q. Duong, *Reduced Ocular Blood Flow as an Early Indicator of Diabetic Retinopathy in a Mouse Model of Diabetes.* Investigative Ophthalmology & Visual Science, 2012. **53**(10): p. 6488-6494.
160. Feke, G.T., et al., *Retinal Circulatory Abnormalities in Type-1 Diabetes.* Investigative Ophthalmology & Visual Science, 1994. **35**(7): p. 2968-2975.
161. Nagaoka, T., et al., *Impaired Retinal Circulation in Patients with Type 2 Diabetes Mellitus: Retinal Laser Doppler Velocimetry Study.* Investigative Ophthalmology & Visual Science, 2010. **51**(12): p. 6729-6734.
162. Harris, A., et al., *Progress in measurement of ocular blood flow and relevance to our understanding of glaucoma and age-related macular degeneration.* Prog Retin Eye Res, 1999. **18**(5): p. 669-87.
163. Patel, V., et al., *Retinal blood flow in diabetic retinopathy.* BMJ, 1992. **305**(6855): p. 678-83.
164. Nguyen, T.T. and T.Y. Wong, *Retinal Vascular Changes and Diabetic Retinopathy.* Current Diabetes Reports, 2009. **9**(4): p. 277-283.
165. Antonetti, D.A., R. Klein, and T.W. Gardner, *Mechanisms of Disease Diabetic Retinopathy.* New England Journal of Medicine, 2012. **366**(13): p. 1227-1239.
166. An, L., T.T. Shen, and R.K. Wang, *Using ultrahigh sensitive optical microangiography to achieve comprehensive depth resolved microvasculature mapping for human retina.* J Biomed Opt, 2011. **16**(10): p. 106013.

167. Lee, J., et al., *Multiple-capillary measurement of RBC speed, flux, and density with optical coherence tomography.* Journal of Cerebral Blood Flow and Metabolism, 2013. **33**(11): p. 1707-1710.

168. Ren, H.G., et al., *Quantitative imaging of red blood cell velocity in vivo using optical coherence Doppler tomography.* Applied Physics Letters, 2012. **100**(23).

169. Flower, R., et al., *Observation of Erythrocyte Dynamics in the Retinal Capillaries and Choriocapillaris Using ICG-Loaded Erythrocyte Ghost Cells.* Investigative Ophthalmology & Visual Science, 2008. **49**(12): p. 5510-5516.

170. Tam, J., P. Tiruveedhula, and A. Roorda, *Characterization of single-file flow through human retinal parafoveal capillaries using an adaptive optics scanning laser ophthalmoscope.* Biomedical optics express, 2011. **2**(4): p. 781-793.

171. Zhi, Z., et al., *Noninvasive Imaging of Retinal Morphology and Microvasculature in Obese Mice using Optical Coherence Tomography and Optical Microangiography.* Investigative Ophthalmology & Visual Science, 2014.

172. Sjolie, A.K., et al., *Retinal microaneurysm count predicts progression and regression of diabetic retinopathy.* Diabetologia, 2009. **52**: p. S30-S30.

173. Maneschi, E., et al., *Quantitative-Evaluation of Early Diabetic-Retinopathy - Microaneurysm Counting on Fluorescein Angiograms.* Diabetologia, 1981. **21**(3): p. 301-301.